MICROSTRUCTURE DEVELOPMENT IN SOLID STATE PROCESSING OF POLYPROPYLENE-TALC COMPOSITES AND MELT PROCESSING OF HIGH MOLECULAR WEIGHT HDPE-CLAY NANOCOMPOSITES

By

Rahul H. Rane

A DISSERTAION

Submitted to
Michigan State University
in partial fulfillment of the requirements
for the degree of

Chemical Engineering-Doctor of Philosophy

2013

ABSTRACT

MICROSTRUCTURE DEVELOPMENT IN SOLID STATE PROCESSING OF POLYPROPYLENE-TALC COMPOSITES AND MELT PROCESSING OF HIGH MOLECULAR WEIGHT HDPE-CLAY NANOCOMPOSITES

By

Rahul H. Rane

This research work is divided into two parts. The main objective of the first part was to study and compare the microstructure developed in the case of polypropylene (PP)-talc composite drawn at an elevated temperature to that of neat PP drawn under similar processing conditions. For a given die geometry, the final draw ratio of both of the die drawn materials increased with draw rate, and plateaued at higher draw rates. The ratio of final void fraction to particle fraction in the case of die drawn PP-talc composite with an initial filler loading of 7.5 vol. % (or 20 wt. %), was found to be higher (2.26 vs. 1.81) than that of the die drawn composite with an initial filler loading of 16.5 vol. %. Microscopic analysis of the drawn materials revealed that the voids in both cases were stretched in the drawing direction and the void volume fractions also leveled above an actual draw ratio (DR) of 7. Voids of higher aspect ratios were observed in the die drawn composite that had lower loading of talc. The average void length in the drawing direction had grown 4-6 times that of the particle length.

The steps of annealing and subsequent drawing led to a 12-15 % increase in crystallinity of the matrix phase, for both die drawn neat PP as well as die drawn PP-talc-20 wt. % composite. Die-drawing led to formation of well developed texture elements of type (110)[001] and (010)[001]. These textures sharpened with DR in both the materials. For a given draw rate, debonding and void growth in the drawn composite resulted in less

developed crystal orientation than drawn neat PP of comparable draw ratio. In the case of die drawn neat PP, the predominant texture type was (110)[001], whereas in the case of die drawn composite it was of type (010)[001]. The void growth in drawn PP-talc-20 wt. % composite progressed with the crystal orientation of the matrix phase, and both of them plateaued above a DR of 7. Despite saturation in void growth as well as crystal orientation, the tensile modulus of the drawn composite increased with DR. For the highest draw rate studied using a wedge die of nominal draw ratio 2, the tensile modulus attained for drawn PP-talc-20 wt. % composite was 3 times that of undrawn neat PP.

The second part of the research work was motivated by the aim of developing nanocomposites of high molecular weight high density polyethylene (HMW-HDPE) with enhanced mechanical properties and improved or similar processability as that of the base resin. This was achieved by adding a small percentage of organoclay with appropriate compatibilizers to the base resin, and using appropriate mixing conditions. Complete exfoliation of the dispersed clay could be achieved with much lower loadings of compatibilizer than those reported in the literature. Injection molded bars of a let-down formulation with 5 wt. % organoclay showed a modulus increase of 19 %. Extensional melt flow tests on nanocomposites with 3 wt. % organoclay showed a similar level of strain hardening to that of neat HMW-HDPE. Despite the strain hardening ability and good dispersion of the organoclay, blown film samples obtained with HMW-HDPE nanocomposites did not show much improvement in the mechanical properties. For similar film thicknesses, all the mechanical properties except the tensile modulus of this material were lower than that of neat HMW-HDPE. The anisotropic orientation of exfoliated platelets during the film blowing operation was found to be a likely cause.

Dedicated to all the proponents of ‘scientific temperament’.

ACKNOWLEDGEMENTS

As I leave the portals of Michigan State University, I want to thank all of the people who helped and supported me during the eventful journey of my Ph.D. First, I would like to thank my Ph.D. advisor Prof. K. Jayaraman. I have learned and still learning a lot from him. My affiliation with him has sharpened my critical thinking ability, and has made my approach more scientific. I am grateful for the valuable time he has spent discussing various topics and answering any questions that I had for him. Without his able guidance and encouragement this work would not have been possible. I would also like to express my gratitude towards my guidance committee members: Prof. L. Drzal and Prof. T. Bieler from the Department of Chemical Engineering and Materials Science, and Prof. F. Pourboghrat from the Department of Mechanical Engineering. I thank them for adjusting their schedules to accommodate all my examination and submission dates. The ideas and suggestions they provided during our meetings were useful in making my Ph.D. work comprehensive.

I would like to thank all the colleagues from the Polymer Processing and Rheology Research Group at MSU: John, Katie, Tanmay, Amit and Weijie. Special thanks to Amit and Weijie for their help on the nanocomposite work. I would like to acknowledge the help rendered to me by the CHEMS staff, namely JoAnn Peterson, Lauren Brown, Nichole Shook and Jennifer Keddle. I am also thankful to Mike Rich and Brian Rook for their help in the CMSC lab. Big thanks to all of my friends and colleagues, for making my experience at MSU an enjoyable and memorable one.

Finally, I would like to take this opportunity to express the deepest gratitude towards my family for their unbounded love and trust. Without the immense love and faith of my

parents, Mr. Hanmant Rane and Mrs. Mangal Rane, it was not possible for me to materialize the goals that I envisioned in my life. They have taken the best care of me and have always supported all of my endeavors. I miss my sister Vidya and her family, and the precious times we spent together during my stay in India. I can't thank them enough for filling the void that was created after I left my parents for my Ph.D. I would like to thank my wife's parents for accepting me as their son-in-law and trusting me with their daughter, even before I graduated and secured a job. Lastly, I would like to thank my wife and life-partner Priya, for all of the care and love that she has given since our marriage. There are no words to express the joy she has brought into my life by becoming the mother to our son, Dhey.

TABLE OF CONTENTS

LIST OF TABLES xi

LIST OF FIGURES xii

CHAPTER 1 1
OVERVIEW AND OBJECTIVES 1
1.1 Microstructure Development in Solid State Processing of PP-talc Composites 1
1.1.1 Solid State Processing of Polymers 1
1.1.2 The Process of Die Drawing 5
1.1.3 Solid State Die Drawing of Polymer Composites 8
1.1.3.1 Debonding 9
1.1.3.2 Void Growth 10
1.1.3.3 Polymer Orientation 11
1.1.4 Deformation during Die Drawing Process 12
1.1.5 Research Motivation and Objectives 17
1.2 Melt Processing of High Molecular Weight-HDPE Nanocomposites 20
1.2.1 Polymer Nanocomposites 20
1.2.2 Research Objective 25

CHAPTER 2 27
MATERIALS, PROCEDURES AND CHARACTERIZATION 27
2.1 Materials 27
2.2 Experimental Procedures and Material Characterization 28
2.2.1 Billet Preparation 28
2.2.2 Die-Drawing Runs 29
2.2.2.1 Lab-scale Die Drawing 29
2.2.2.1 Pilot-scale Die Drawing 30
2.2.3 Density Measurements 32
2.2.4 Scanning Electron Microscope 33
2.2.4.1 Sample Preparation 33
2.2.4.2 Testing Procedure 33
2.2.5 X-ray Diffraction (XRD) 34
2.2.5.1 Experimental Setup 34
2.2.5.2 Pole Figure Measurements 35
2.2.6 Tensile Tests 36
2.2.7 Differential Scanning Calorimetry (DSC) 37

CHAPTER 3 39
DRAW STRESS AND MORPHOLOGY OF DIE-DRAWN PP-TALC COMPOSITES 39
3.1 Introduction 39

3.2 Background 40
3.2 Research Objectives 44
3.3 Experimental 46
3.3.1 Materials 46
3.3.2 Procedures 47
3.3.2.2.1 Density Measurements 48
3.3.2.2.2 Morphological Study 48
3.4 Results and Discussion 49
3.4.1 Draw Stress 49
3.4.2 Void Growth 53
3.5 Conclusions 64

CHAPTER 4 70
CRYSTAL ORIENTATION AND MODULUS OF DIE DRAWN PP-TALC COMPOSITE 70
4.1 Introduction 70
4.1.1 Crystalline Morphology of PP-talc Composites 70
4.1.2 Crystal Orientation during Die Drawing 73
4.2 Experimental 76
4.2.1 Materials 76
4.2.2 Procedures 76
4.2.2.1 Die Drawing Runs 76
4.2.2.2 Characterization 77
4.2.2.2.1 Density Measurements 77
4.2.2.2.2 X-ray Diffraction 77
4.2.2.2.3 Tensile Tests 79
4.2.2.2.1 Differential Scanning Calorimetry (DSC) 80
4.3 Results and Discussion 80
4.3.1 Rates of Density reduction and Draw Ratios 83
4.3.2 Crystallinity and XRD Patterns 86
4.3.3 Texture Evolution 94
4.3.4 Tensile Properties of Final Drawn Products 116
4.4 Conclusions 118

CHAPTER 5 120
MELT PROCESSING OF HIGH MOLECULAR WEIGHT HDPE-CLAY NANOCOMPOSITES 120
5.1 Introduction 120
5.2 Research Objective 121
5.3 Material and Experimental Details 124
5.3.1 Materials 124
5.3.2 Nanocomposite Preparation 125
5.3.3 Sample preparation 127
5.3.4 XRD 128
5.3.5 Extensional Rheology 130
5.3.6 DSC 132

5.3.6 Flexural Tests 133
5.3.8 Film Testing 134
5.4 Results and Discussion 135
5.5.1 Effect of Mixing Time 135
5.5.2 Two Stage Mixing vs. Single Stage Mixing 136
5.5.3 Flexural Properties with Injection Molded Bars 141
5.5.4 Film Blowing and Processability 145
5.5 Conclusions 152

CHAPTER 6 153
SUMMARY AND RECOMMENDATIONS 153

APPENDICES 161
APPENDIX A 162
APPENDIX B 168

REFERENCES 173

LIST OF TABLES

Table 4.1: Percentage crystallinity of neat PP and PP-talc-20 wt. % billets at different locations. The sample numbers in the table correspond to different locations shown in Figure 4.4…….90

Table 5.1: Constituents of HMW-HDPE nanocomposites with clay……..124

Table 5.2: Mechanical properties of blown films of HMW-HDPE and LD2-3 nanocomposite containing 5 wt. % Si-I.44P produced with a BUR of 4.5……...148

Table 5.3: Mechanical properties of blown films of HMW-HDPE and LD1-4 nanocomposite containing 3 wt. % Si-I.44P produced with a BUR of 2.5……...151

LIST OF FIGURES

Figure 1.1: Schematic of a ram extrusion process. 2

Figure 1.2: Schematic of a hydrostatic extrusion process..... 2

Figure 1.3: Schematic of a roll drawing process..... 3

Figure 1.4: Schematic of a free tensile drawing process. 4

Figure 1.5: Schematic of a die drawing process. 4

Figure 1.6: A three dimensional schematic of the die drawing process. 5

Figure 1.7: Schematic of different deformation zones in die-drawing process. 6

Figure 1.8: Schematic of debonding or void initiation. 9

Figure 1.9: Schematic showing void growth along the drawing direction 11

Figure 1.10: Typical relation between engineering stress and strain during tensile drawing of a flexible polymeric material. 14

Figure 1.11: Schematic of a transcrystalline lamella on the surface of a talc particle and other lamella attached to it. 19

Figure 1.12: Schematic of 2:1 layered silicate 21

Figure 1.13: Schematic representation of clay dispersion process. 24

Figure 2.1: Particle size distribution for FDC talc. 28

Figure 2.2: Experimental setup and the wedge die used for lab-scale die drawing runs. . 30

Figure 2.3: Experimental setup and the wedge die used for pilot-scale die drawing runs. 31

Figure 2.4: Samples of PP-talc-20 wt. % (or 7.5 initial vol. %) composite cut from its billet before and after die drawing runs on pilot-scale setup. 32

Figure 2.5: Schematics of specimens used for SEM preparation. The shaded planes shown (a) perpendicular to the width and (b) perpendicular to the thickness direction were viewed under SEM; the arrow indicates draw direction. 33

Figure 2.6: Schematic of the X-ray diffraction experiment. 35

Figure 2.7: The reference directions and the 15º net used for reading pole figures. 36

Figure 2.8: Schematic of ASTM D638- type I tensile bar with total length of 230 mm. . 37

Figure 3.1: Schematic representation of different stages of void growth around an untreated particle in control volume element of a composite. 45

Figure 3.2: Drawing force vs. displacement during die drawing of PP-talc-38 wt. % composite for the draw rate of 101.6 cm/min. 49

Figure 3.3: Variation in die drawing stress and density for drawn PP-talc-38 wt. % composite as a function of draw rate. 50

Figure 3.4: Actual draw ratio vs. draw rate for die drawn PP-talc-38 wt. % composite. . 51

Figure 3.5: Actual draw ratio vs. draw rate for die drawn PP-talc-20 wt. % composite. . 51

Figure 3.6: Draw stress vs. draw ratio for drawn PP-talc-38 wt. % composite. 52

Figure 3.7: Density vs. DR_{final} for (a) PP-talc-38 wt. % composite drawn on lab-scale setup and (b) PP-talc-20 wt. % composite drawn on pilot-scale setup. 53

Figure 3.8: SEM images of PP-talc-38 wt. % composite drawn on lab-scale setup with a draw rate of (a) 12.7 cm/ min, DR_{final}=5.3(scale bar =200 μm) and (b) 50.8 cm/min DR=6.6 (scale bar =100 μm) 56

Figure 3.9: SEM images of PP-talc-20 wt. % composite drawn on lab-scale setup with a draw rate of (a) 91.4 cm/ min, DR_{final}=6.1 (scale bar =200 μm) and (b) 573 cm/min DR=8.1 (scale bar =200 μm) 57

Figure 3.10: Colored SEM pictures of (a) drawn PP-talc-38 wt. % DR_{final}=5.3 (scale bar =200 μm) and (b) drawn PP-talc-20 wt. % DR_{final}=6.1 (scale bar =200 μm) 59

Figure 3.11: SEM images of MD-ND planes for (a) undrawn PP-talc-20 wt. % (scale bar =100 μm) and (b) drawn PP-talc-20 wt. % DR_{final}=7.7 (scale bar =200 μm) 61

Figure 3.12: SEM images of MD-TD planes for (a) undrawn PP-talc-20 wt. % (scale bar =100 μm) and (b) drawn PP-talc-20 wt. % DR_{final}=7.7 (scale bar =200 μm) 62

Figure 3.13: Particle lengths (a) in MD and (b) in TD measured in MD-ND planes for pilot die drawn samples. 64

Figure 3.14: Particle dimensions measured in MD-TD planes of pilot die drawn samples. 65

Figure 3.15: Histograms of void stretch ratio for PP-talc-20 wt. % composite samples drawn on the pilot-scale setup at (a) 91, (b) 244, (c) 366 and (d) 573 cm/min. 66

Figure 3.16: Density ratio (final/initial) and void stretch ratio vs. DR_{final} for drawn PP-talc-20 wt. % composite. 69

Figure 4.1: Schematics of real and modified unit cell of i-PP. 75

Figure 4.2: Final area ratio of the die drawn neat PP and PP-talc-20 wt. % composite vs. draw rate 82

Figure 4.3: Actual draw ratio of die drawn neat PP and PP-talc-20 wt. % composite vs. draw rate 82

Figure 4.4: Billet sections of (a) neat PP and (b) PP-talc-composite collected after die-drawing runs at 573 cm/min. 83

Figure 4.5: Density variations in different deformation zones. 84

Figure 4.6: Rate of change of DR in the die and developing post-die deformation zones. 86

Figure 4.7: Linear XRD patterns of un-drawn neat PP and un-drawn PP-talc composite. 86

Figure 4.8: DSC endotherms of neat PP before and after annealing. 88

Figure 4.9: Effect of deformation on DSC endotherms of (a) die drawn neat PP and (b) die drawn PP-talc-20 wt. % composite. 89

Figure 4.10: Effect of deformation on the linear XRD patterns of (a) die drawn neat PP and (b) die drawn PP-talc-20 wt. % composite 91

Figure 4.11: Optical images of neat PP (a) un-drawn and (b) die-drawn at 5.73 m/min (DR_{final}=8.8). 94

Figure 4.12: Pole figures of α(040) and α(110) crystal planes of iPP in (a) un-drawn neat PP and (b) un-drawn PP-talc-20 wt. % composite..... 96

Figure 4.13: Pole figures of individual crystal axes of iPP in (a) un-drawn neat PP and (b) un-drawn PP-talc-20 wt. % composite. 98

Figure 4.14: Pole figures of individual crystal axes of iPP for (a) neat PP at the die entrance, DR=1.07 and (b) PP-talc-20 wt. % composite at the die entrance, DR=1.06. 100

Figure 4.15: Pole figures of individual crystal axes of iPP for (a) neat PP at the die exit, DR=1.47 and (b) PP-talc-20 wt. % composite at the die exit, DR=1.44. 102

Figure 4.16: Pole figures of individual crystal axes of iPP for (a) neat PP at location 4, DR= 2.49 and (b) PP-talc-20 wt. % composite at location 4, DR= 2.36. 103

Figure 4.17: Pole figures of individual crystal axes of iPP for (a) neat PP at location 6, DR=5.14 and (b) PP-talc-20 wt. % composite at location 6, DR=4.55. 104

Figure 4.18: Pole figures of individual crystal axes of iPP for (a) neat PP at location 8, DR=6.04 and (b) PP-talc-20 wt. % composite at location 8, DR=5.79. 105

Figure 4.19: Evolution of the Herman orientation parameter of the crystalline c-axis of PP phase. 107

Figure 4.20: Calculated positions of ideal (a) (110)[001] type and (b) (010)[001] type texture elements on (100) and (010) and (001) pole figures..... 109

Figure 4.21: Peak intensities in the ND-TD plane on (a) 100-axis and (b) 010-axis of neat PP at locations 4, 6, 8, 9 and 10 or Final with corresponding DRs of 2.5, 5.1, 6.0, 6.5 and 8.8 (c) 100-axis and (b) 010-axis of PP-talc-20 wt. % at locations 4, 6, 8, 9 and 10 or Final with corresponding DRs of 2.4, 4.5, 5.8, 6.2 and 8.1. 111

Figure 4.22: Development of the two texture elements viz. (110)[001]=T_1 and (010)[001]=T_2 vs. DR in (a) die drawn neat PP and (b) die drawn PP-talc composite. . 114

Figure 4.23: Plot of intensity ratios of texture T_2 to texture T_1 vs. draw ratio for the die-drawn samples of PP-talc-20 wt. % composite and neat PP..... 115

Figure 4.24: Herman orientation parameter of drawn materials as a function of final draw ratio attained at different draw rates. 116

Figure 4.25: Tensile stress-strain curves for undrawn and die drawn (drawn at 573 cm/min) neat PP and PP-talc-20 wt. % composite. 117

Figure 4.26: Tensile modulus of drawn materials as a function of DR_{final} attained for different draw rates. 118

Figure 5.1: Schematic of a Banbury type batch mixer used for melt blending. 126

Figure 5.2: Schematic of an extensional viscosity fixture (EVF) used to measure extensional viscosity behavior of polymeric melts. 131

Figure 5.3: Effect of mixing time for GR205/Cl-15A (97/3 wt/wt) nanocomposites prepared on a small Brabender mixer. 135

Figure 5.4: XRD patterns showing the effect of compatibilizer loading on dispersion in single shot mixing. The compounds were prepared using Polylab (OS) torque rheometer. 136

Figure 5.5: XRD patterns for a commercially available masterbatch MB0 with 50 wt. % I.44 P clay and its let-down compound LD1-0: HMW-HDPE/MB0 (90/10 wt.%) prepared on Polylab (OS) torque rheometer 138

Figure 5.6: XRD patterns of masterbatch MB1 with Si-I.44P/GR205/HIVAL (30/30/40 wt. %) and its let-down LD1-1 compound: HMW-HDPE/MB1 (83.3/16.7 wt. %), prepared on the Brabender mixer. 139

Figure 5.7: XRD patterns of masterbatch MB2 with 40/30/30 wt. % of Si-I.44P/SA/Hival and its let-down compounds LD1-2: HMW-HDPE/MB2 (87.5/12.5 wt. %), LD2-2: HMW-HDPE/GR205/MB2 (77.5/10/12.5 wt. %) and LD3-2: HMW-HDPE/GR205/MB2 (71.5/16/12.5 wt. %). 140

Figure 5.8: XRD patterns of MB3 with Si-I.44P/SA/HIVAL (40/35/25 wt. %) and its let-down compounds: LD1-3 with HMW-HDPE/MB3 (87.5/12.5 wt. %) and LD2-3 with HMW-HDPE/GR205/MB3 (77.5/10/12.5 wt. %) prepared on a twin screw extruder... 141

Figure 5.9: DSC curves of low molecular weight compatibilizer (SA), high density polyethylene (HIVAL) and their masterbatch (MB3 with Si-I.44P clay). 142

Figure 5.10: Flexural modulus of HMW-HDPE, LD1-0: HMW-HDPE/MB0 (90/10 wt. %) and LD2-3 with HMW-HDPE/GR205/MB3 (77.5/10/12.5 wt. %) 143

Figure 5.11: Flexural strength of HMW-HDPE, LD1-0: HMW-HDPE/MB0 (90/10 wt. %) and LD2-3 with HMW-HDPE/GR205/MB3 (77.5/10/12.5 wt. %) 144

Figure 5.12: Flexural yield strain of HMW-HDPE, LD1-0: HMW-HDPE/MB0 (90/10 wt. %) and LD2-3 with HMW-HDPE/GR205/MB3 (77.5/10/12.5 wt. %) 144

Figure 5.13: Uniaxial melt extensional viscosity of neat HMW-HDPE conditioned for 7 minutes before testing at 210ºC. 145

Figure 5.14: Uniaxial melt extensional viscosity of neat GR205 and GR205/Cl-15A composite tested at 190ºC without conditioning. 146

Figure 5.15: Uniaxial melt extensional viscosity of HMW-HDPE nanocomposite tested at 195ºC without conditioning. 147

Figure 5.16: XRD patterns of MB4 with Si-I.44P/SA (50/50 wt. %) and its let-down compound LD1-4 with HMW-HDPE/GR205/MB4 (88/6/6 wt. %) prepared on Polylab OS torque rheometer. 149

Figure 5.17: Uniaxial melt extensional viscosity behavior of HMW-HDPE and LD1-4 nanocomposite with HMW-HDPE/GR205/MB4 (88/6/6 wt. %). Both conditioned for 5 min. before testing at 210ºC..... 150

Figure A.1: Area ratio of PP-talc-38 wt. % drawn on a lab-scale setup. 163

Figure A.2: Area ratio of PP-talc-20 wt. % drawn on a pilot-scale setup..... 163

Figure A.3: SEM images of PP-talc-20 wt. % composite die drawn at 91 cm/min (a) MD-ND plane (scale bar =200 μm) and (b) MD-TD plane (scale bar =100 μm) 164

Figure A.4: SEM images of PP-talc-20 wt. % composite die drawn at 244 cm/min (a) MD-ND plane (scale bar =200 μm) and (b) MD-TD plane (scale bar =200 μm) 165

Figure A.5: SEM images of PP-talc-20 wt. % composite die drawn at 366 cm/min (a) MD-ND plane (scale bar =200 μm) and (b) MD-TD plane (scale bar =200 μm). 166

Figure A.6: SEM images of PP-talc-20 wt. % composite die drawn at 573 cm/min (a) MD-ND plane (scale bar =200 μm) and (b) MD-TD plane (scale bar =100 μm). 167

Figure B.1: Schematic of experimental setup used to study XRD of PP-talc-38 wt. % composite drawn on lab-scale setup. 170

Figure B.2: XRD patterns of PP-talc-38 wt. % composite and the Luzenac talc. 170

Figure B.3: Position of plane normal $P_{(h,k,l)}$ by spherical coordinates χ and φ. 171

CHAPTER 1
OVERVIEW AND OBJECTIVES

This research work is divided into two parts. The first part of the dissertation is discussed in Chapters 2 through 4, and constitutes major portion of the work. The main focus of the first part was to study microstructural development in solid state die drawn polypropylene (PP)–talc composites. The second part (Chapter 5) is devoted to the development and characterization of well-dispersed nanocomposites of film grade high molecular weight high density polyethylene (HMW-HDPE). In the following sections an overview and the problem statement for each part are described briefly:

1.1 Microstructure Development in Solid State Processing of PP-talc Composites

1.1.1 Solid State Processing of Polymers

Solid state processing of semi-crystalline polymers at elevated temperatures is done to enhance their mechanical, chemical and physical properties. These improvements are related to higher levels of crystallinity and orientation brought about in the process. To reach maximum improvements in the properties the polymers are oriented in their sub-molten state (heated at a temperature somewhere between the crystallization temperature and the melting temperature). It is difficult to orient the polymers that do not have a clear crystallization temperature[1]. The commonly employed solid-state processing techniques include ram extrusion, hydrostatic extrusion, roll drawing, free tensile drawing and die drawing. The ram extrusion process is shown schematically in Figure 1.1.

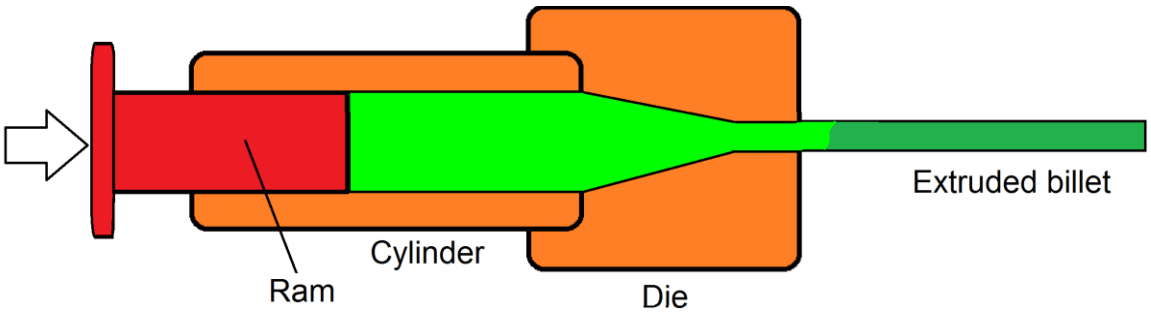

Figure 1.1: Schematic of a ram extrusion process.

For interpretation of the references to color in this and all other figures, the reader is referred to the electronic version of this dissertation.

The heated polymer compact or billet is pressurized using a hydraulically operated ram that forces the polymer through a converging die. This process has been used to produce various profiles such as tapes, sheets, tubes, etc. The process of ram extrusion is severely limited by its slow production rate. Attempts to operate the process at higher rates have been reported[2] to result in higher frictional forces and process instabilities, resulting in extremely distorted products. The process instabilities were reduced to some extent by extruding the billet using a hydrostatic extrusion process (Figure 1.2).

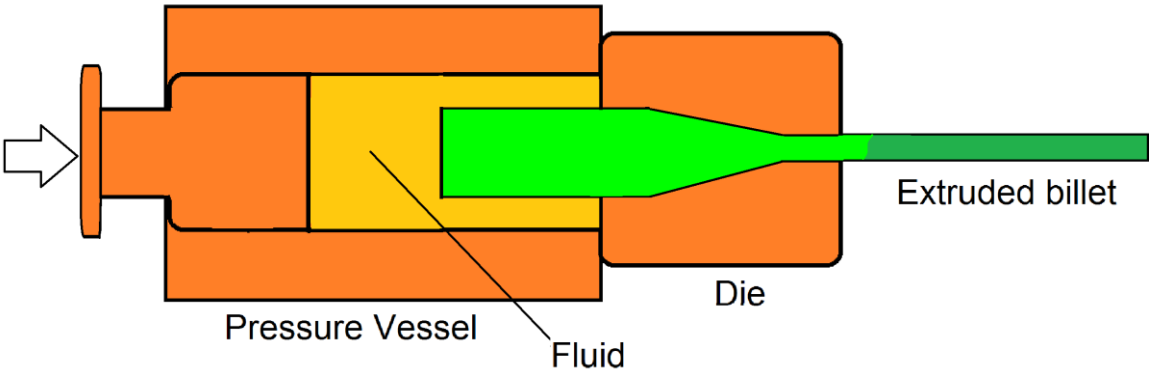

Figure 1.2: Schematic of a hydrostatic extrusion process.

In this process, instead of a ram, the heated polymer billet is forced using pressurized fluid. The use of hydrostatic fluid provides lubrication, which gives reduced extrusion pressure and therefore, a slightly higher draw rate than ram extrusion. However, due to the compressive nature of the applied draw stress, the production rate cannot be improved beyond a certain limit. Higher production rates in the drawing processes can be realized by employing draw stresses that are tensile in nature. This principle is used in the drawing techniques such as free tensile drawing, roll drawing and die drawing.

In the free tensile drawing (Figure 1.3) a polymeric billet is heated inside of a closed oven. When the billet reaches the desired draw temperature it is subjected to a uniaxial extension.

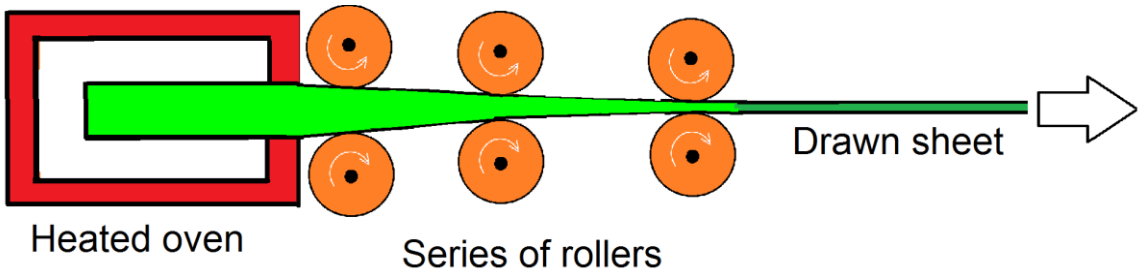

Figure 1.3: Schematic of a roll drawing process.

The shoulders of the billet can be manufactured in different ways to fit to various grips in the tensile machine. It is difficult to produce oriented rods and other relatively large sections by this process. Gripping problems and lack of heat control render yield a low output with this technique. For higher outputs the drawing process is carried by roll drawing and die drawing. As shown in Figure 1.4, in a typical roll drawing process a thick polymer sheet is conveyed through a series of rollers, in which the downstream set of rollers rotate at a faster rate than the upstream set of rollers.

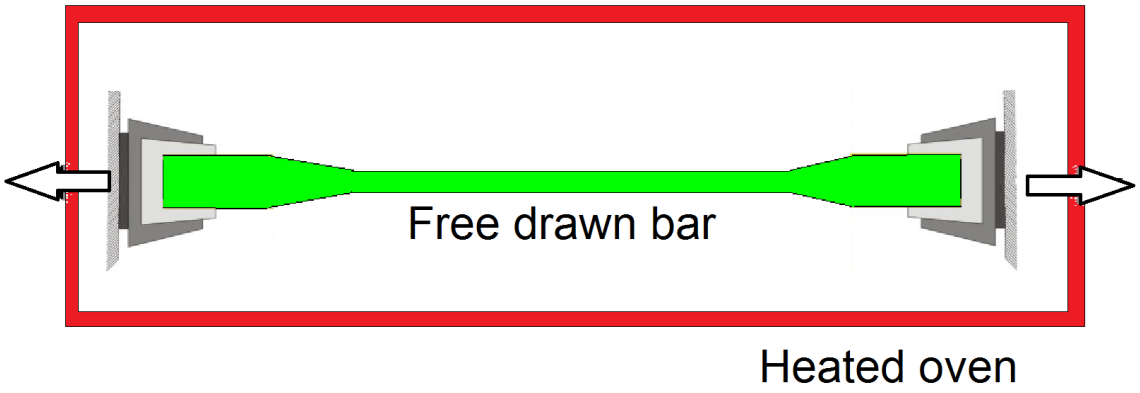

Figure 1.4: Schematic of a free tensile drawing process.

The degree of orientation obtainable in this process is measured by the thickness reduction of the feedstock sheet. Larger thickness reductions can be achieved if the feedstock is heated to the draw temperature or the temperature of rollers. The process of roll drawing has been primarily used to produce highly oriented tapes and films. For larger oriented shapes such as rods, I-beam sections, tubes and other shaped profiles, the process of die drawing (Figure 1.5) has been found to be beneficial.

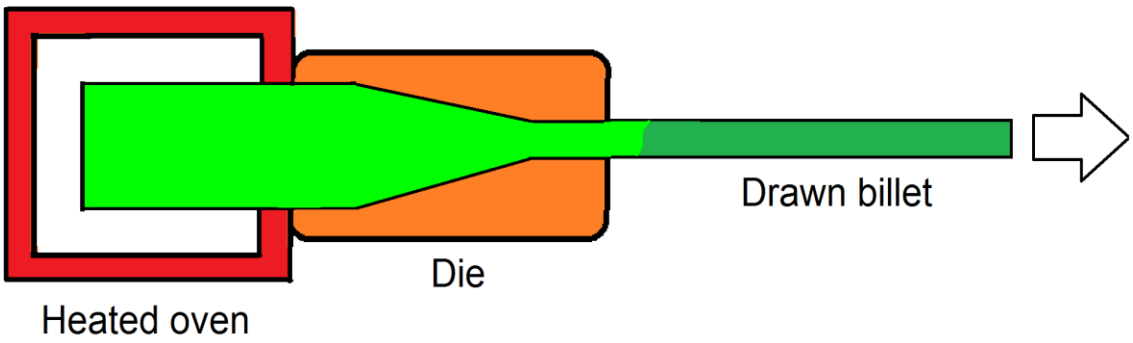

Figure 1.5: Schematic of a die drawing process.

The die drawing process consists of drawing a heated polymer billet through a shaped die (heated to the same temperature as the draw temperature) without the application of any

pressure. In its orientable state the polymeric billet does not maintain a large contact area with the processing equipment. This results in an efficient conversion of the applied forces into molecular orientation. Our work for the first part of the research was mainly focused on the solid state die drawing process.

1.1.2 The Process of Die Drawing

Among the various types of solid state processing techniques, the die drawing process has been found to be cost-effective in terms of attaining higher production rates. A relatively simpler experimental setup, capability to attain significant orientation levels using minimum draw stress, and the convenience of operating it in either batch or continuous mode have made this process commercially attractive. As presented in Figure 1.6, in this process, a billet of a given semicrystalline polymer is heated to an elevated temperature below the crystalline melting point and is drawn through a converging die heated to the same temperature.

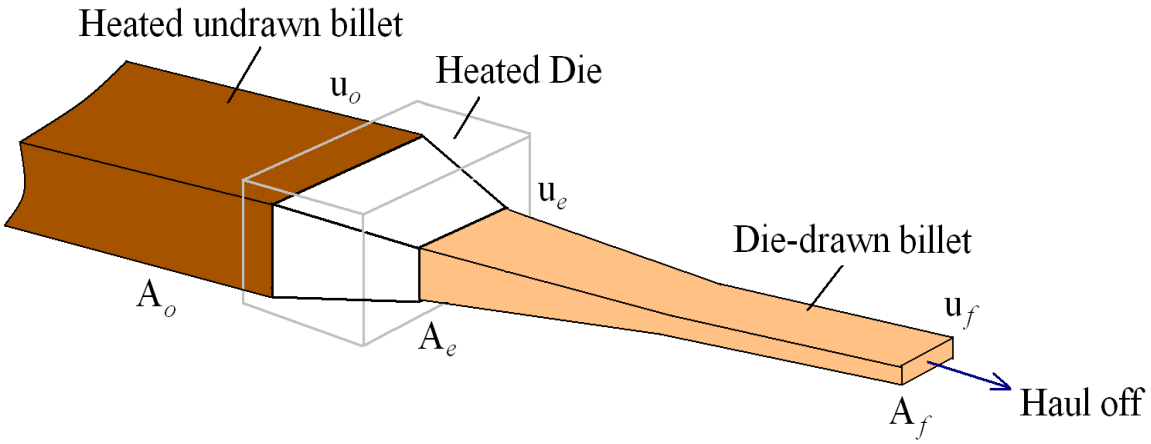

Figure 1.6: A three dimensional schematic of the die drawing process.

For unfilled polymers the die drawing process can give up to 10-20 fold increase in modulus[2]. In addition to the improved mechanical properties, the drawn materials also show low creep, low axial coefficient of thermal expansion, low permeability to gases and fluids and an improved resistance to chemical attack[3]. The final properties of a die drawn product depend on deformation level experienced by the material during the drawing process. The deformation of a material during its die-drawing process takes place in two distinct zones: die zone and post-die deformation zone as shown in Figure 1.7. The degree of deformation can be quantified in terms of actual draw ratio[3-6].

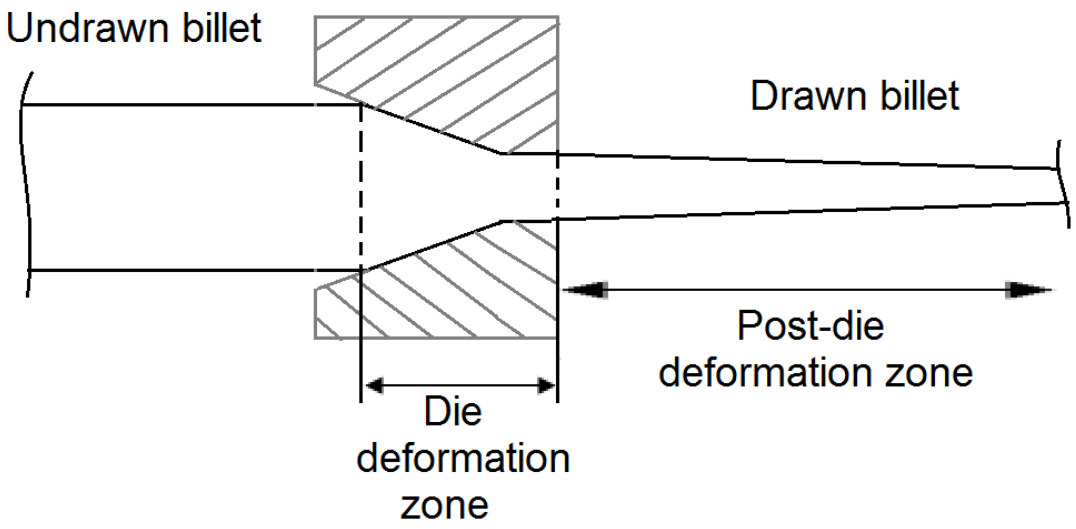

Figure 1.7: Schematic of different deformation zones in die-drawing process.

An actual draw ratio (DR) is defined as the ratio of take-up velocity (u_f) to the initial velocity of the billet (u_0). When the change in density is accounted for during the steady drawing process, the resulting equation for the draw ratio is:

$$DR \equiv \frac{u_f}{u_0} = \frac{\rho_0 A_0}{\rho_f A_f} \qquad (1.1)$$

A_f and ρ_f denote the final cross-sectional area and density of the drawn product and A_0 and ρ_0 denote the cross-sectional area and density of the billet before die drawing.

The axial mechanical properties such as tensile modulus and tensile strength of the drawn products increase with actual draw ratio up to a maximum value[3-6]. The maximum attainable DR increases with the nominal draw ratio (ratio of the inlet billet cross sectional area to the cross-sectional area of the die exit) of the converging die as well as the draw rate employed. Although it increases with the draw temperature, there is an optimum range of temperature (10-30°C below the crystalline melting point) which gives maximum improvement in axial modulus[3-4]. In addition to the processing parameters, the deformation behavior of a material during die drawing process also depends on its structural morphology. For example, die drawing of polyoxymethylene (POM)[4] led to cavitation in the matrix and subsequently reduced density starting at a DR of 2. On the other hand, no density reduction was observed in the case of drawn linear polyethylene (LPE), not even for DRs up to 30. For a given polymer, the maximum draw ratio has been reported to increase with the crystallinity and decrease with the molecular weight of the initial undrawn polymer[3]. The maximum draw ratio has also been shown to increase with the polydispersity index of the polymer.

1.1.3 Solid State Die Drawing of Polymer Composites

Solid state die drawing of composites of semicrystalline polymers filled with micron sized particles is done to produce light weight structural materials with reduced density and improved mechanical properties[7-9]. During an elevated temperature drawing of the polymeric composite, the microscopic phenomena of debonding of particles from the matrix phase and subsequent void growth lead to reduced density, whereas the orientation of the polymeric phase leads to enhanced mechanical properties of the drawn product. Nichols et al.[7] have reported that die drawing of PP-talc composite loaded with 46 wt. % (22 vol. %) talc resulted in as much as an 80 % increase in modulus and 40 % decrease in density compared to that of the undrawn composite. Although voiding is desired, it must be controlled otherwise it can result in premature failure of the drawn material. For example, die drawing of POM filled with 20 wt. % (10 vol. %) short glass fibers caused an excessive voiding (60-70 vol. %), and culminated in macroscopic fracture of the drawn products just after exiting the die[10]. An optimization of processing parameters and material composition is needed to reach a desired level of density and acceptable level of mechanical properties without affecting the production rate. In order to engineer the final properties of a die drawn product, it is important to understand the microscopic phenomena and development of microstructure during the drawing process of a microcomposite. At the microscopic level, the following key phenomena occurring during composite drawing determine the final properties of the drawn product:

1) The debonding of the filler particles from the matrix phase or void initiation,

2) The void growth around the debonded particles and

3) The orientations of the filler and matrix phases.

A significant research problem involves understanding and tracking these microscopic events with an ultimate aim of controlling final properties of the drawn product.

1.1.3.1 Debonding

During initial deformation of a polyolefin microcomposite, the stress at the filler-matrix interface is relieved by the onset of debonding of the non-treated filler particles. The debonding of a rigid filler particle begins at the points of maximum stress concentration as shown in Figure 1.8.

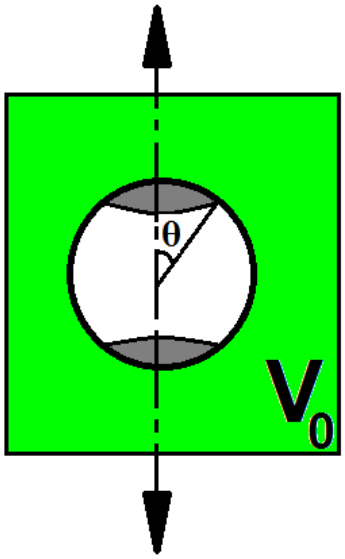

Figure 1.8: Schematic of debonding or void initiation.

When a polymeric composite is subjected to mechanical deformation, the damage in the material takes place mainly by crazing, shear yielding, debonding and cavitation. Many experimental and numerical studies[11-25] on particulate composites filled with micron and over micron size particles have shown that among the various mechanisms, debonding of the micron sized particles requires minimal stress and hence it is the dominant

mechanism of damage. The debonding stress is function of moduli of the two phases, particle-shape, size and size distribution, interfacial work of adhesion, residual stresses present in the material and the drawing temperature and rate.

1.1.3.2 Void Growth

Further deformation of the composite leads to crazing, shear yielding and void growth[21-23]. The dominance of one or the other mode depends on the temperature of drawing, interparticle distance and stress-strain state in the material. After the onset of void initiation or debonding at the filler-matrix interface, debonding proceeds along the phase boundary. In the case of non-polar matrices such as HDPE and PP, the debonding progresses along the interface until complete debonding of the filler particle from the matrix phase take place, and the void covers the entire surface of the filler[13,19-20,25]. At larger deformations, in cases of composites a with a lower filler loading, the void around the debonded particles get stretched in the drawing direction, as shown in Figure 1.9. The relative lengthening of fully formed voids in the direction of loading is close to the mean draw ratio of the deformed region[13].

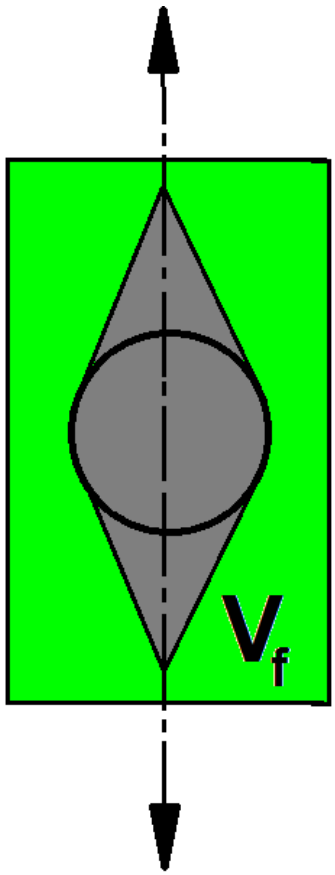

Figure 1.9: Schematic showing void growth along the drawing direction

With some exception[14], most of the literature on void initiation and void growth is limited to tensile test studies that are carried out at room temperature. None of those studies are reported for higher draw rates that are of interest to us.

1.1.3.3 Polymer Orientation

Semicrystalline polymers such as PE and PP contain a highly ordered crystalline phase and a highly disordered amorphous phase. The crystalline lamellae consist of polycrystalline structures of different natures (depending on the packing geometries), sizes and size distributions. The stacks of crystalline lamellae in the crystalline domains are separated by an amorphous phase, and within the stacks the lamellae are separated by

thin amorphous interlayers. The amorphous domains contain entangled networks of tie chains. The nature, fraction, and characteristics of the crystalline as well as the amorphous phases are affected[26-30] by the inherent material characteristics such as molecular structure, molecular weight, molecular weight distribution, polarity of the molecules, presence of additives, etc. Their characteristics and fractions also depend on the external factors such as temperature and stress profiles to which they are exposed. Depending on the stress state of the applied deformation, the orientation of the different domains progress differently. The orientation levels in polymers have been studied using various techniques[31-36]such as X-ray diffraction (XRD), atomic forced microscopy (AFM), birefringence, optical microscopy (OM), electron microscopy (EM) and infrared spectroscopy (IR). Most of these studies are limited to unfilled polymers.

In the die drawing process of microcomposite, the microscopic events of debonding, void growth and polymer orientation are affected by the degree of deformation experienced by the material.

1.1.4 Deformation during Die Drawing Process

The deformation of a given material during die drawing process takes place mainly in two-zones[37]: (a) within the converging die where the material is deformed isothermally up to the nominal draw ratio of the die and (b) in the post-die deformation zone where the material necks down freely as shown in Figure 1.7.

As the material moves farther from the die exit, it is progressively cooled. In the final part, it ceases to deform beyond a certain point. The deformation in the post-die deformation zone occurs isothermally in the initial part and non-isothermally in the later part. The

lengths of isothermal and non-isothermal post die deformation zones are functions of material and process parameters. When the drawn material loses contact with the die wall, it follows an energetically favorable stress-strain-strain rate path, reducing the required flow stress considerably[38]. Because of this and lack of any hydrostatic pressure, very high draw ratios can be achieved with low draw stresses during the die-drawing process of polymeric materials. The draw stress can be further reduced using higher drawing temperatures.

Since the strain rate field in the post-die deformation zone is imposed solely by the polymer and drawing conditions rather than by the die geometry, the process of die drawing is advantageous mainly for strain hardening polymers. These polymers are capable of forming a stable neck that propagates even at the larger draw ratios that are imposed at higher draw rates[37]. Experimental and theoretical work[19, 25] on drawing of voided microcomposites in a tensile test setting have shown that large plastic deformations are possible for the composites with strain hardening polymers as the matrices. Based on these observations, it can be said that the die drawing process for composites would give best results in terms of improved properties with semicrystalline polymers like PP, polyethylene or polyoxymethylene, which have the ability to strain harden.

Finite element analyses[4, 39-41] of a solid phase die drawing process through a converging die have concluded that the stresses developed in the process are largely tensile in nature; the tensile stresses are generated from about 70-80 % of die length and dominate the post-die deformation zone. Studying the deformation characteristics of a given material

with tensile stress-strain curve can be highly informative in the context of its die drawing. A constant strain rate tensile stress-stain curve of a flexible polymer typically shows[42] five regions as presented in Figure 1.10. Sketches drawn in the figure show a dog-bone tensile specimen in different deformation regions.

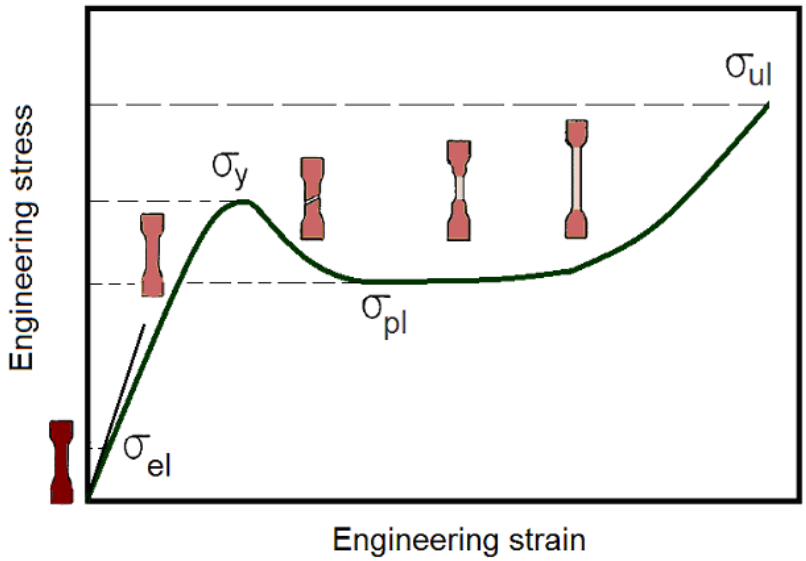

Figure 1.10: Typical relation between engineering stress and strain during tensile drawing of a flexible polymeric material.

As the test specimen is pulled, the engineering stress in the first region increases linearly with engineering strain until it reaches a particular value denoted as σ_{el}. This region is known as the linear elastic deformation region. The slope of the linear portion (or tangent drawn from the origin in the figure) gives the Young's modulus of the material. The Young's modulus of the polymer increases with the addition of reinforcing filler. Beyond the linear elastic deformation region, the increase in stress becomes less and it progresses non-linearly with the strain until it reaches the yield point. The stress at this point is called as the yield stress (σ_y). The non-linearity is set at lower strains for polymeric composites than for the corresponding unfilled polymers; sharp kinks can be observed for

microcomposites that are filled with particles bigger than a critical particle size[16]. Beyond the yield point, increased strain leads to a decrease in stress to a certain value denoted as σ_{pl}. The difference ($\Delta\sigma^{i}$) between σ_y and σ_{pl} has been associated with the homogeneity of the deformation[13, 43]. A high difference due to greater localized deformation gives higher reduction of the cross sectional area during necking and vice versa. In the fourth region the material undergoes plastic deformation where the neck is propagated by drawing into new portions of weakly deformed areas from the surrounding material[13]. In this region the stress-strain curve becomes nearly parallel to the strain axis. The draw ratio corresponding to the final strain reached at the end of this region is also known as the natural draw ratio of the material. A non-strain hardening material would break after reaching its natural draw ratio. A strain hardening or strain softening material on the other hand, would continue to deform until it is ultimately broken at a stress σ_{ul}. If the difference between σ_{ul} and σ_{pl} is positive ($\Delta\sigma^{ii}$), as shown in the figure, then this region is termed the strain hardening region, if it is negative ($-\Delta\sigma^{ii}$), then it is called the strain softening region; in this case, the plastically deformed section in this case would shed the load to the surrounding weak areas.

Constant strain rate tensile tests reported on neat PP have shown that the stresses σ_y ,σ_{pl} ,σ_{ul} as well as their differences $\Delta\sigma^{i}$ and $\Delta\sigma^{ii}$ decreased, whereas its natural draw ratio increased with increase in test temperature[44]. As the temperature is raised, the resistance of polymer crystals to plastic deformation goes down, making it possible to draw the polymer to a higher strain without a premature failure. Similar observations

have been made for some polymers drawn by die-drawing process[2], and the same results can be expected during the die drawing process of a polymer composite. In a recent work, Polec and coworkers[45] have reported enhancements in tensile moduli for drawn neat PP as well as drawn PP-wood powder (68/32 vol/vol) composites with increased draw temperature. The composites in their study could reach a drawing temperature very close to the melting temperature of PP. With regard to the influence of strain rate on deformation of neat PP, an increase in σ_y ,σ_{pl} ,σ_{ul} and $\Delta\sigma^{ii}$, but a decrease in $\Delta\sigma^{i}$ have been reported for the tests carried out at a constant test temperature of 150^{o}C. This means that drawing with higher draw rates would reduce localized deformation, giving quicker formation and propagation of a homogeneous neck. The important question is, how would this affect the final orientation of the matrix phase, especially when it is loaded with rigid filler particles? The presence of rigid particles bigger than a certain size and with a poor adhesion (or without any surface treatment) to the matrix phase reduces the yield stress of the material with increasing filler loading[11-13]. More importantly, the micron size particles get debonded from the matrix phase before the material reaches its yield point[16-18].

Some of the main questions that need to be answered in the context of high temperature-high strain rate solid state die drawing of polymeric composites are: How do the micron sized particles get oriented during the die drawing process? How is the void initiation and subsequent void growth affected by the interparticle distance? At what deformation levels can we attain significant degree of matrix orientation, and how would that be

affected by the other microscopic damage mechanisms? Does a different crystalline morphology of the matrix phase due to the presence of particles, affect the plastic deformation of the material? Our research work on die drawing of a microcomposite was aimed at answering a few of these important questions.

1.1.5 Research Motivation and Objectives

This research work was focused on unfilled and filled systems of isotactic polypropylene (i-PP) as the model polymer. Isotactic PP can crystallize[26-30, 35-36] in lamellae with the following different crystal forms categorized, based on different packing geometries of the PP helices: monoclinic (α), trigonal (β), triclinic (γ) and smectic (δ). The crystallization of i-PP in various categories is decided by the melting history, crystallization temperature, stress and cooling rate and presence of foreign particles. The most stable and common crystal form for i-PP is the monoclinic α-form. X-Ray diffraction (XRD) has been used frequently to investigate the development of crystal structure or texture in processed isotactic polypropylene[44, 46-50]. In the case of neat PP, the crystalline lamellae are radially oriented in spherulitic structures. Deformation of polypropylene, either with very low strain rate tensile tests carried out at different temperatures[44],or with high strain rate roll drawing[47-49] and die-drawing[3-5, 46] processes carried out at high temperatures has been shown to transform the initial spherulitic morphology to fibrous morphology where the block lamellar structures get oriented along the flow direction.

There are few papers available on the crystalline morphology of extruded and injection molded PP-talc composites[51-53]; however, to our knowledge no work has been published

on polymer crystal orientation during composite drawing. Presence of filler particles with anisometric shapes introduces an important difference in crystal morphology of the matrix phase from that of the unfilled or neat polymer. The inorganic filler particles provide more nucleation sites, resulting in faster crystallization of i-PP yielding a greater number of smaller crystalline domains[54]. Naiki et.al[55] showed that under quiescent conditions, slow cooling of a PP melt resulted in formation of transcrystalline regions at the interface of PP and talc particles. In these regions the crystalline lamellae grew orthogonal to the surface of platy talc particles until they impinged on spherulites nucleated in the bulk, Ferrage and coworkers[54] have described that there is a preferred orientation of PP crystals in the presence of crystalline talc where the mineral c-axis is merged with the PP b-axis (matching (001) plane of talc with the (010) plane of PP). Kitayam and others[56] found that for the transcrystalline lamellae attached directly to the fibers, the PP chain folding direction or c-axes were oriented parallel to the fiber length. Based on these observations, a schematic of a PP transcrystal grown on talc surface can be drawn as shown in Figure 1.11. The symbols a*, b and c in the figure denote the equivalent orthogonal axes of the monoclinic α-crystal structure of isotactic polypropylene.

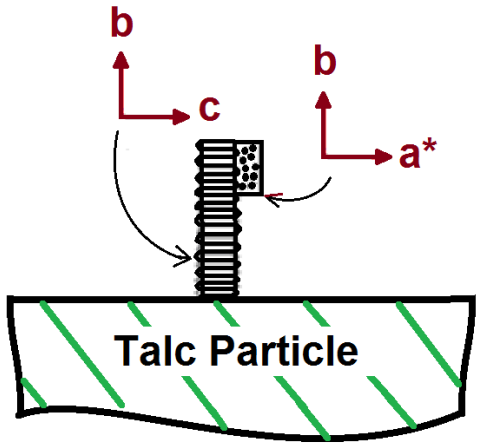

Figure 1.11: Schematic of a transcrystalline lamella on the surface of a talc particle and other lamella attached to it.

Due to an initially different microstructure, the drawability and orientation achieved on drawing of PP-talc composite would be different than that of neat PP. Moreover, the process of debonding of rigid particles from the matrix phase, and subsequent void growth would change the deformation mode and affect the crystalline orientation of the matrix phase. During die-drawing of PP-talc composites, the debonding of particles was expected to occur at very small deformation therefore the main objectives of this part of the research work were:

- To study the effect of process parameters on the content and morphology of the voids formed in the die drawn PP-talc composites filled with different levels of filler loadings and
- To investigate and compare the effect of annealing and subsequent deformation on the content, texture and orientation of the PP crystals in die drawn PP-talc composite to that unfilled PP drawn under similar processing conditions.

1.2 Melt Processing of High Molecular Weight-HDPE Nanocomposites

1.2.1 Polymer Nanocomposites

To achieve sufficient improvement in mechanical properties polymer microcomposites are prepared by loading higher levels of micron sized particles (anywhere from 10 to 45 wt/wt basis). These highly filled polymeric systems are often associated with some inherent drawbacks such as higher density, difficulties in melt processing, lack of transparency, lack of flexibility, etc. The advances made in the field of polymeric nanocomposites over the last two decades have been helpful in overcoming some of these problems. Polymer nanocomposite is a special class of polymer particulate composite in which the reinforcement (nanofiller) used has at least one dimension that is at nanometer scale. These composites have attracted significant interest because they have shown dramatic enhancement in the physical, thermal, gas barrier and mechanical properties for lower loadings of the fillers. As compared to the traditional microcomposites, this not only helps in reducing the density, but also in attaining relatively easier processing and higher flexibility. Lower loading levels of the nanoparticles are effective in obtaining the above discussed improvements because of their larger surface area to volume ratios; particularly when they are well-dispersed. Nanoclays (e.g. layered silicates), nanotubes (e.g. carbon nanotubes) and nanofibers (e.g. ceramic nanofibers) are some of the most commonly used nanofillers. Among these, the nanoclays are the most widely used nanofillers due to their ease of availability and cost. The generic term ‘nanoclays’ refers to natural clays, but also to synthesized nanoclays such as mica, laponite and fluorohectrorite. The most commonly used nanoclays belong to the structural family

known as the 2:1 phyllosilicates. Their crystal lattice consists of two-dimensional layers, where a central octahedral sheet of alumina or magnesia is fused to two external silica tetrahedrons by the tip so that the oxygen ions of the octahedral sheet also belong to the tetrahedral sheet, as shown in Figure 1.12.

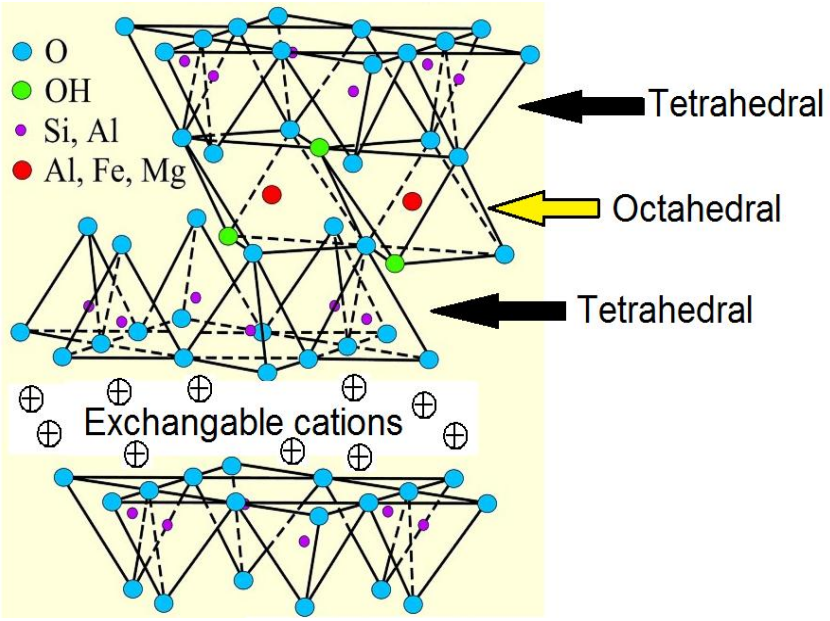

Figure 1.12: Schematic of 2:1 layered silicate
(Modified from http://pubs.usgs.gov/of/2001/of01-041/htmldocs/clays/smc.htm)

The layer thickness is around 1 nm and the lateral dimensions of these layers may vary from 300 nm to several microns. These layers organize themselves to form stacks with regular Van der Waals gaps in between them known as the clay galleries. Isomorphic substitutions of Si^{4+} for Al^{3+} in the octahedral sheet cause an excess of negative charge within the layers. This excess negative charge is counterbalanced by alkali or alkaline earth cations such as Ca^{2+} and Na^{+} situated within the layer. Because of their excellent intercalation ability the smectic phyllosilicates commonly used are montmorillonite,

hectorite and saponite. For this part of our research work we used montmorillonite as the nanoclay.

Clay nanocomposites can be prepared by dispersing the nanoclay in the polymer by using different techniques such as in situ polymerization, solution blending or melt mixing. Melt mixing is the most economical, and hence widely used processing technique to prepare commercial nanocomposites. Due to their hydrophilic nature, the nanoclays are difficult to disperse in the organic polymer therefore, they are always treated with an organic treatment. The first organic treatment used to prepare a polyamide 6-clay nanocomposite was amino acid. Numerous other kinds of organic treatments have since been used in the synthesis of polymer nanocomposites. The most popular organic treatment is done with alkyl ammonium ions, as they can be easily exchanged with the ions situated between the silicate layers. The commonly used alkyl ammonium ions are based on primary alkyl amines with chemical structure: CH_3-$(CH_2)_n$-NH_3 where n is between 1 and 18. Alky ammonium ions based on secondary alkyl amines are also used. It is interesting to note that the length of the ammonium ion has a strong impact on the resulting structure of the nanocomposites. For example, Lan et al.[57] showed that alkyl ammonium ions with chain lengths larger than 8 carbon atoms favored delaminated nanocomposites with well separated nano-layers in the matrix phase. The organic treatment lowers the surface energy of the base nanoclay, permitting other organic species with different polarities to get intercalated between the clay layers. For polar thermoplastics such as nylon6, polysiloxanes some non-polar thermoplastics like polystyrene, the organic treatment of the nanoclays is sufficient to achieve a good degree of clay dispersion during melt mixing. However, for polyolefins such as polypropylene or

polyethylene, which represent the biggest volume of polymers produced, organic treatment of the nanoclays alone is not enough to get well-intercalated composites. The incompatibility between a polyolefin and the clays is both thermodynamic as well as physical in nature. The stacks of nanolayers in given clay are held together by Van der Waal's forces of attraction and are unwilling to reach the state of disorder. The chemical unsuitability between the non-polar organic matrix and the polar hydrophilic clay makes it difficult to bond the two phases physically or in a non-thermodynamically favorable manner. Through the organic or surface treatment it is possible to change the interlayer structure of the smectic clays, both increasing the gallery spacing and modifying the silicate surface in an organic fashion. This artifice is not enough, and the use of a third polarizing component better known as 'compatibilizer' becomes essential in order to achieve well-dispersed polyolefin nanocomposites.

In general the compatibilizer used in the melt mixing step is prepared from the base polymer by introducing some polar group like maleic anhydride in it. For example to prepare well-dispersed PE nanocomposites, the most suitable compatibilizer is polyethylene grafted with maleic anhydride (PE-g-MA). This type of compatibilizer is produced by reactive extrusion using a peroxide initiator, which causes free radical formation by scission of polyolefin chains. In a simple binary mixture of PE and organoclay, the task of PE-g-MA would be to establish a bond between the two species. The hydrocarbon part of the compatibilizer is miscible with the PE matrix, whereas the polar group is linked with the hydroxyl groups on the clay particles through hydrogen bonding, making it possible for the nanolayers of the organoclay to get completely separated. If the nanoclay is treated with some surfactant that has reactive groups on it,

then there is a possibility of a inducing a chemical interaction between the organoclay and the compatibilizer. The formation of a strong chemical bond between the two species will further reduce or completely eliminate the repelling effect between them.

The use of compatibilizer to render the organoclay and the base polymer compatible has made it possible for the melt intercalation process to be accepted as the most economical, environmentally and user friendly technique to prepare polyolefin nanocomposites. The extent of dispersion of the organoclay in a given polymeric matrix depends on the concentration and interaction abilities of the raw materials as well as the intensity of mixing. A schematic of the clay dispersion attained in a typical melt mixing process is shown in Figure 1.13.

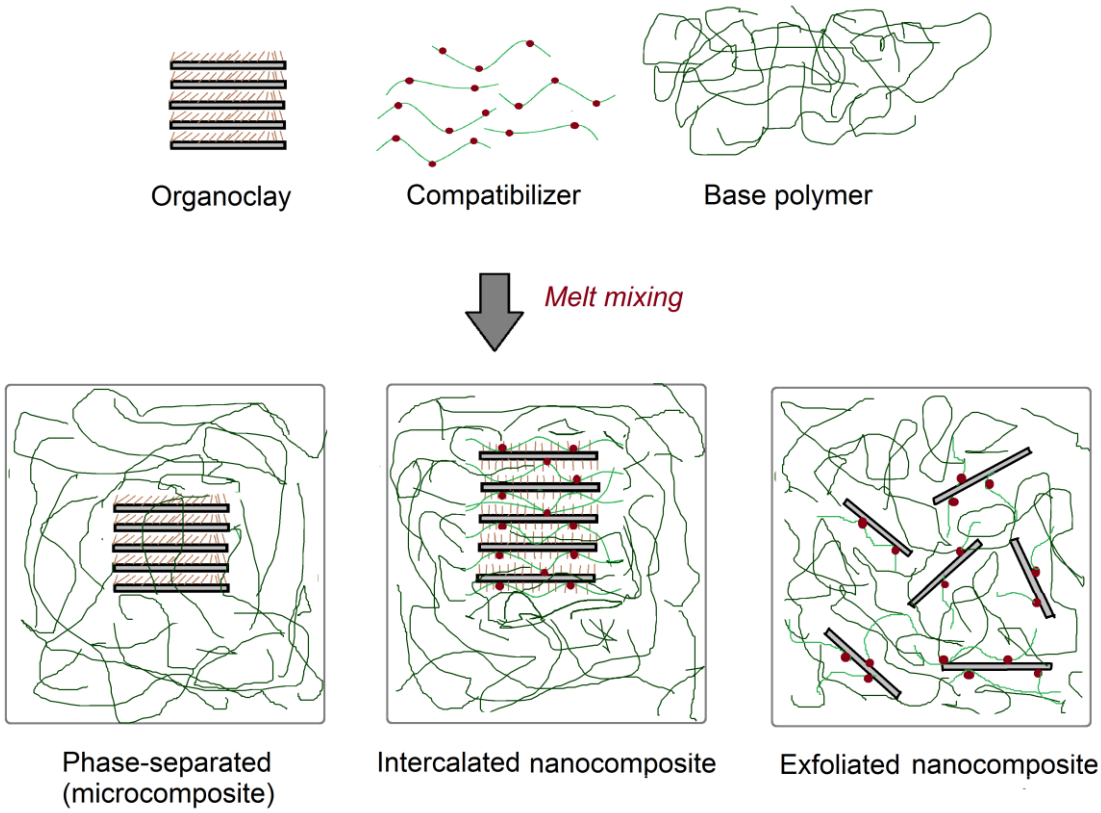

Figure 1.13: Schematic representation of clay dispersion process.

A poor dispersion of the organoclay (for example in the absence of any compatibilizer) leads to a phase separated structure, where the clay tactoids would exist in their original aggregated state with no insertion (intercalation) of polymer matrix between the layers. In this state, the particles can impart only a marginal enhancement in properties of the base matrix. In an intercalated nanocomposite, the polymer chains are inserted into the clay galleries, and at the end of the melt mixing process they get crystallized in a stereo-regular fashion. The penetration of polymer chains in the clay galleries increases the spacing between the clay layers but retain a well-ordered multilayer morphology. In an exfoliated nanocomposite, the nanolayers get completely separated from each other and are well-dispersed in the continuous matrix. Well-exfoliated clay layers offer very high surface to volume ratio at the filler-matrix interface, and hence, an effective bonding between the two phases. In general, a nanocomposite is composed of a random combination of various structures discussed above. A good judgment in selection of the raw materials and process parameters is necessary to achieve well dispersed nanocomposites of a given polymer.

1.2.2 Research Objective

The main goal of this part of the research was to prepare and characterize nanocomposites of different compositions based on HMW-HDPE and organoclays, along with specific maleic anhydride grafted polyethylene grades. The films made of HMW-HDPE are used in automotive aftermarket; specifically as masking alternative to paper in body repair shops. It is supposed to have good tear strength and tensile strength. The purpose of the research objective for preparing nanocomposites of HMW-HDPE was to attain improved mechanical properties through the reinforcement of well dispersed

organoclay without compromising the processability of the base resin during the film blowing operation. In particular, the project was focused on using the aminosilane treated organoclay in order to extend advancements[58] made with linear polypropylene to high molecular weight HDPE clay nanocomposites. Addition of aminosilane treated clay to PP has been shown to impart strain hardening extensional viscosity behavior necessary for foaming and film blowing. This effect is especially noticeable when the organoclay is treated with chosen silane coupling agents. The proper formulation of nanocomposite with HMW-HDPE matrix must have good dispersion and adequate coupling, brought about by the reaction between the aminosilane and the maleic anhydride in the compatibilizer. In addition, the entanglement density of the compatibilizer chains must be sufficient to keep the strain hardening behavior in the melt.

CHAPTER 2
MATERIALS, PROCEDURES AND CHARACTERIZATION

2.1 Materials

The polymeric matrix used to study solid state die-drawing was isotactic polypropylene (i-PP) homopolymer (Dow grade 5D37) with a density of 0.905 g/cc and a melting temperature of 166(±2)^{o}C. The polymer had a M_W of 249400, a polydispersity index of 4.7 and a melt flow rate of 2.8 g/ 10 min. Two grades of untreated talc particles were used as fillers. The first grade, TC-100 by Luzenac was used to mold composite billets for lab-scale die-drawing runs. The talc had specific gravity in the range of 2.7 to 2.8; the median equivalent spherical diameter of the talc particles was 16.4 microns. Another grade of talc-FDC by Luzenac was used to mold billets for pilot scale-die drawing runs. This grade of talc had more controlled particle size, with a median equivalent spherical diameter of 18 microns. The particle size distribution for this talc is shown in Figure 2.1. The specific gravity of the talc was 2.8 and it had a surface area of 1-2 m^2/g.

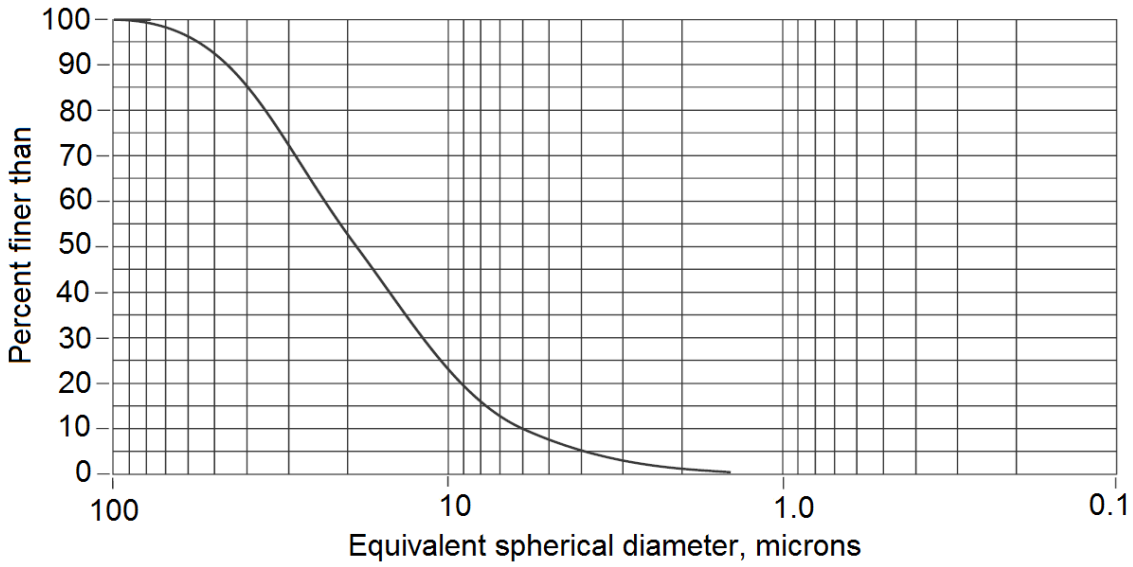

Figure 2.1: Particle size distribution for FDC talc.

2.2 Experimental Procedures and Material Characterization

2.2.1 Billet Preparation

The polypropylene was compounded with TC-100 talc in a continuous mixer (Farrel CP250) and injection molded into a 45 cm long billet for the die drawing operation on the lab-scale die drawing set up. The molded billet had cross-sectional dimensions of 1.27 cm x 0.317 cm and a 10 cm long shaped tail that would fit the converging die. The filler content in the molded composite was fixed at 38 wt. % (16.5 vol. %) as determined by the ash content test (ASTM D5630-06).

For die drawing runs on a pilot scale set up, one billet for each polypropylene/FDC talc composite (92.5/7.5 vol/vol) and neat PP was compounded in a co-rotating intermeshing twin screw extruder, at the compounding laboratory at Dow Chemicals, Midland. The compounding was done in a side fed 3.81 cm single screw extruder operated at 190^{o}C.

Billets of rectangular cross section (5.08 cm x 1.52 cm) were extruded by controlling the haul off rate, so as to obtain a shaped tail that will fit in the solid phase die drawing line in the next step. The filler content as determined by the ash content test (ASTM D5630-06) in extruded billet was 20 wt. % (16.5 vol. %).

Before performing the die-drawing runs, the molded billets were marked with thick marker lines along their widths. The intermediate billet sections- between two draw rates were identified based on the spacing between the marked lines, which were then discarded.

2.2.2 Die-Drawing Runs

2.2.2.1 Lab-scale Die Drawing

Figure 2 shows a schematic of the lab scale die drawing process and the converging die used for the same.

The undrawn billet of a given material was supported inside of a heated oven. The converging die in this setup reduced the cross sectional area of the inlet billet by a factor of 3.2 (1.6 in the width direction and 2 in the thickness direction). The ratio of billet cross sectional area to the cross-sectional area of the die exit is also known as the nominal draw ratio of the die. The converging section of the die is 7.62 cm long and it has a die length of 2.54 cm. The billet of a given material was preheated to 150^{o}C for an hour and drawn using 5 different draw rates, specifically, 2.54 cm/min, 12.7 cm/min, 25.4 cm/min, 50.8 cm/min and 101.6 cm/min. At each draw rate the billet was drawn to an approximate length of 30.48 cm. The drawn material was cooled using a freezer spray to avoid relaxation before cutting it approximately 4 cm away from the die exit. During the

drawing process, a load cell attached to the pulling unit recorded the applied load as a function of displacement of the material away from the die.

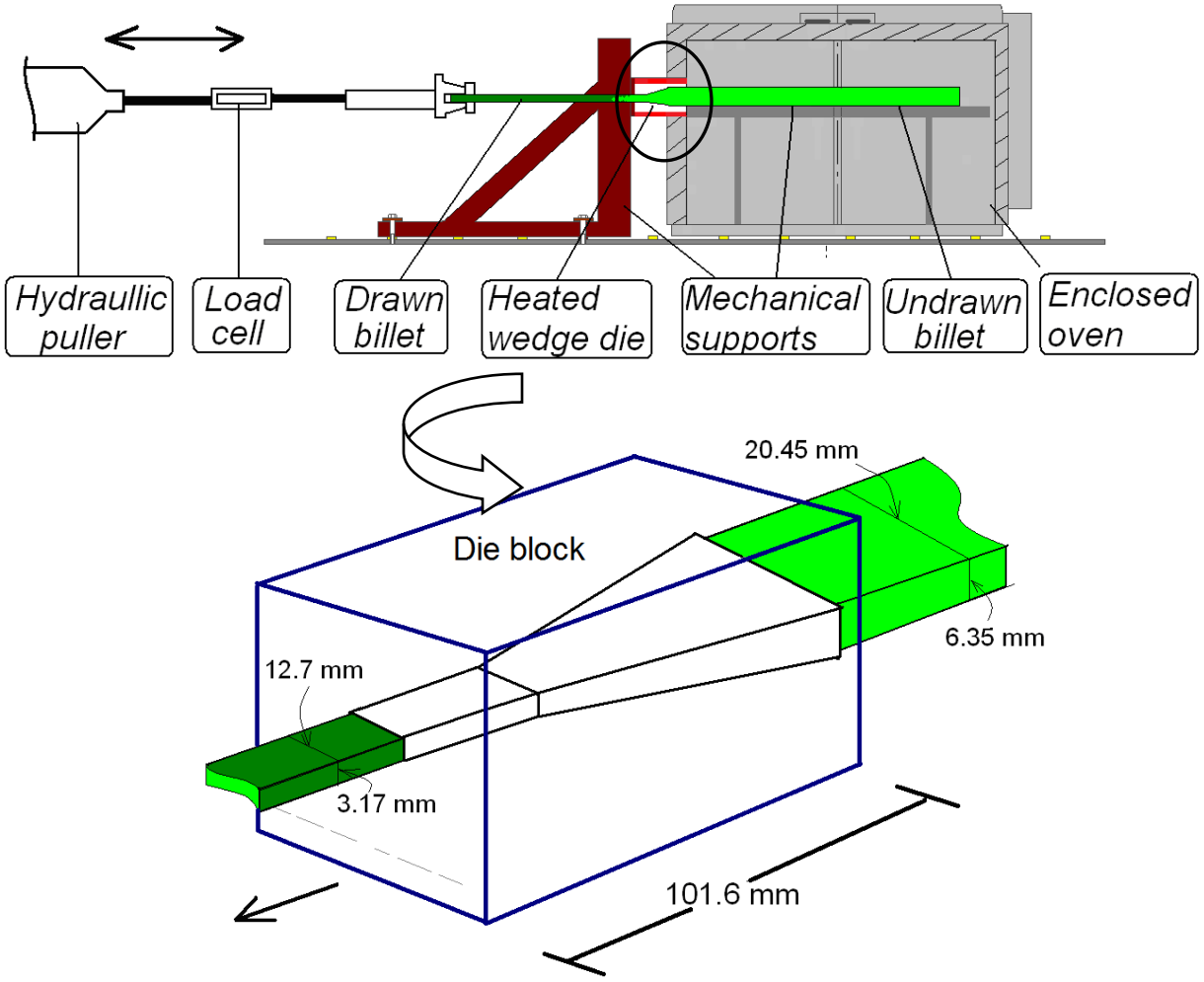

Figure 2.2: Experimental setup and the wedge die used for lab-scale die drawing runs.

2.2.2.1 Pilot-scale Die Drawing

The schematics of the die drawing setup and wedge die used for pilot-scale die drawing runs are shown as Figure 2.3. The shaped tail of a given billet was fitted through a wedge die and was taken through a water tank to the belt puller. The nominal draw ratio of the

converging die from the inlet to the exit was 2, with equal reduction ratios ($\sqrt{2}$) for the two dimensions of the die cross section.

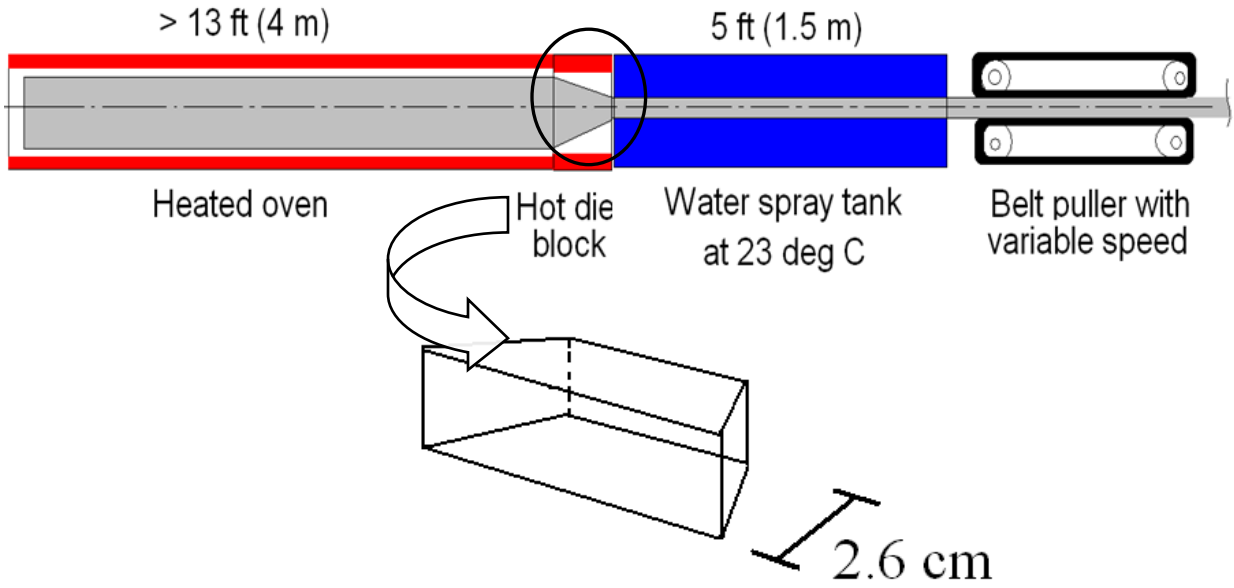

Figure 2.3: Experimental setup and the wedge die used for pilot-scale die drawing runs.

The given billet was preheated for an hour and a half to 145^{o}C before drawing through a wedge die maintained at the same temperature. To avoid breaking of the material, the preheated billet was drawn by gradually increasing the draw rate. During the drawing process, the drawn billet was cooled by a water spray tank maintained at 23^{o}C. When sufficient length of the drawn material was obtained at one speed, the drawing speed was gradually increased to a higher rate. The drawn material in the transition zone was then discarded. The die drawing was performed using the following 4 different draw rates: 0.91, 2.44, 3.66 and 5.73 m/min. Specimens of undrawn and drawn PP-talc composite cut away from the die are shown in Figure 2.4.

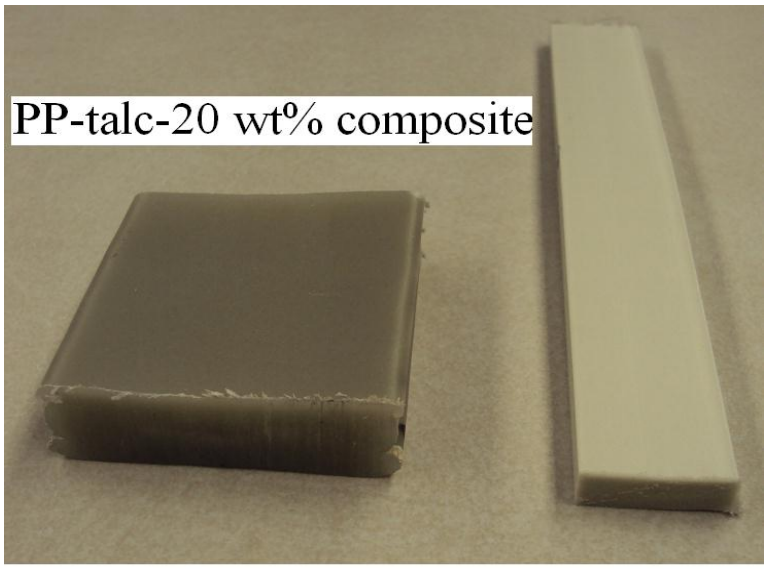

Figure 2.4: Samples of PP-talc-20 wt. % (or 7.5 initial vol. %) composite cut from its billet before and after die drawing runs on pilot-scale setup.

2.2.3 Density Measurements

Densities of the samples before and after drawing were measured using the Sartorius density determination kit -YDK-01, which works on Archimedes's principle. The kit is equipped with hydrostatic balance that enables weighing of the samples in air (W_{air}) as well as in water ($W_{liq.}$). For die-drawn samples, a minimum of three specimens taken farther from the die-exit were tested to get an average density for the final draw ratio. The density of a given specimen was calculated using equation 2.1. There was a variation of ± 0.003 in the density measurements.

$$\rho = \frac{W_{air} \cdot \rho_{liq.}}{W_{air} - W_{liq.}} \qquad (2.1)$$

2.2.4 Scanning Electron Microscope

2.2.4.1 Sample Preparation

Microscopic pictures were obtained for cuboidal specimens cut from the composite billet before and after die-drawing. The specimens for drawn billets were viewed in a plane perpendicular to the width direction, as well as in a plane perpendicular to the thickness direction, as shown by filled planes in Figure 2.5(a) and 2.5(b) respectively.

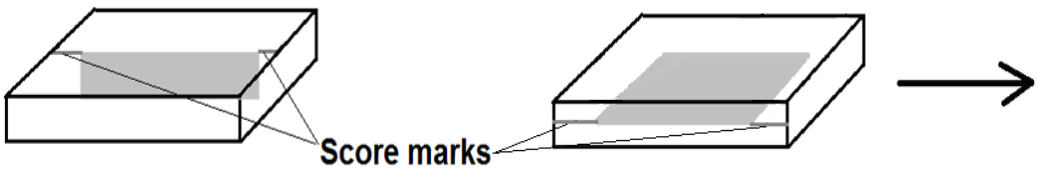

(a) **(b)**

Figure 2.5: Schematics of specimens used for SEM preparation. The shaded planes shown (a) perpendicular to the width and (b) perpendicular to the thickness direction were viewed under SEM; the arrow indicates draw direction.

The composite specimens were scored along the score marks with a razor blade and immersed in liquid nitrogen for 20 to 30 minutes. The specimens were removed from the liquid nitrogen and fractured along the score marks. The fractured samples were then mounted on SEM stubs and sputter coated with either gold or osmium to make the sample conductive, and to eliminate charging during imaging. The prepared specimens were kept in a dessicator for a minimum of 24 hrs. to remove any moisture.

2.2.4.2 Testing Procedure

Microscopic images of the specimens were obtained on a JEOL JSM-6400 SEM using an accelerating voltage of 8 to10 kV. Care was taken to avoid images too close to the edges of the sample, which may have been altered during scoring and fracturing of the sample.

For each specimen viewed, multiple images were gathered, at varying magnifications to ensure that an accurate portrayal of the sample was obtained.

2.2.5 X-ray Diffraction (XRD)

2.2.5.1 Experimental Setup

Crystal orientations in drawn and undrawn billets of neat PP and PP-talc composite were characterized using a theta-2theta Scintag XDS-2000 wide angle X-ray diffractometer in reflection mode. The computer-controlled diffractometer consisted of a Huber pole figure goniometer mounted at its center and coupled to sealed-anode CuK_{α} X-ray tube. The X-ray tube was operated with an accelerating voltage of either 35 or 40 kV, and a corresponding amperage of 35 or 40 mA to generate nickel filtered monochromatic beam of CuK_{α} radiation ($\lambda = 1.542\ A^{o}$). A high accelerating voltage and amperage was applied for the composite samples because the crystalline talc present in the material absorbs much of the X-rays. The incident beam was collimated by a 1 mm diameter collimator. For die-drawn samples obtained from lab-scale die drawing runs, rectangular specimens of 15 x 10 x 2.4 mm^3 dimensions were cut and machined for XRD studies. Here, 10 mm and 2.4 mm are the final dimensions of the composite billet drawn at the highest draw rate along the transverse direction (TD) and normal direction (ND) respectively. For billet samples collected before and after die drawing runs on the pilot-scale setup, circular specimens of 14 mm diameter were machined from the cut cuboidal sections of dimensions 20 x 16.5 x 5 mm^3. Here, the width=16.5 mm (along the TD) and thickness = 5 mm (along the ND) were same as the final cross-sectional dimensions of the neat PP drawn at the highest draw rate. The samples were exposed to X-rays by placing the

thickness parallel to the diffraction plane; an example for a circular sample is shown in Figure 2.6. The distance between the sample holder and the detector was fixed at 270 mm. For a given specimen the goniometer was used to get a one-dimensional 2 theta (θ) scan over the detector angle, as well as to get pole figures by rotating and tilting the specimen. The 2-theta XRD patterns and pole figures were obtained with the help of the DMSNT software (version 1.37).

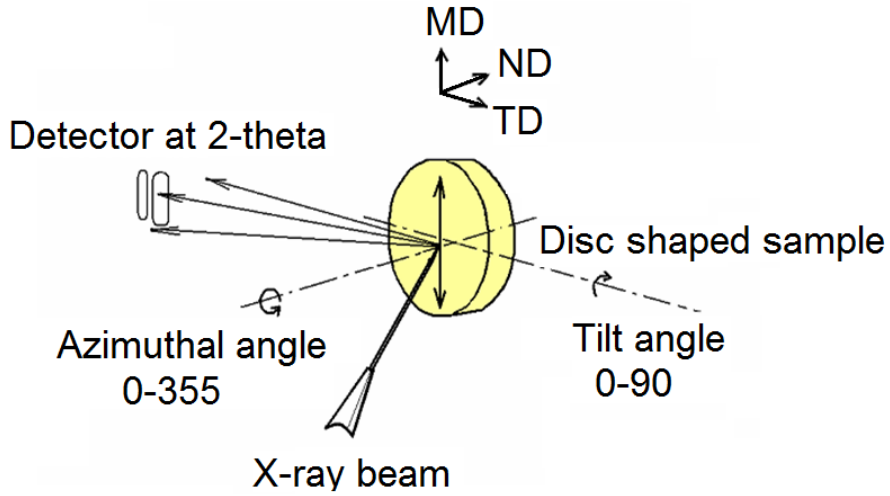

Figure 2.6: Schematic of the X-ray diffraction experiment.

2.2.5.2 Pole Figure Measurements

After an initial linear diffraction (2θ) scan, azimuthal scans were run with the detector positioned at a 2θ angle of either α(110) crystal plane or α(040) crystal plane reflection of the iPP matrix. Pole figures were obtained by varying the azimuthal angle (φ) from 0^o to 355^o and tilt angle (χ) from 0^o to 85^o, with an angle step of 5^o in either sweep. Pole figures acquired by the azimuthal scans were processed and corrected for background intensities using BEARTEX 2008 software (version 3.3). The software incorporates

WIMV algorithm[59], which was used to calculate orientation distribution of the intensities for pole figures with incomplete range of tilt angles. The pole figure intensities were plotted in the units of multiplication of a probability density for random distribution (m.r.d.: 0.01 is equal to the pole density of random distribution). To understand some of the features of crystal orientation in greater detail, pole figures of individual crystal axes of the matrix phase were obtained using the PCAL routine of the BEARTEX software, an orthorhombic symmetry of the PP unit cell was assumed. Figure 2.7 shows the reference directions and the 15^{o} net of tilt and azimuthal angles used for discussion of the pole figures.

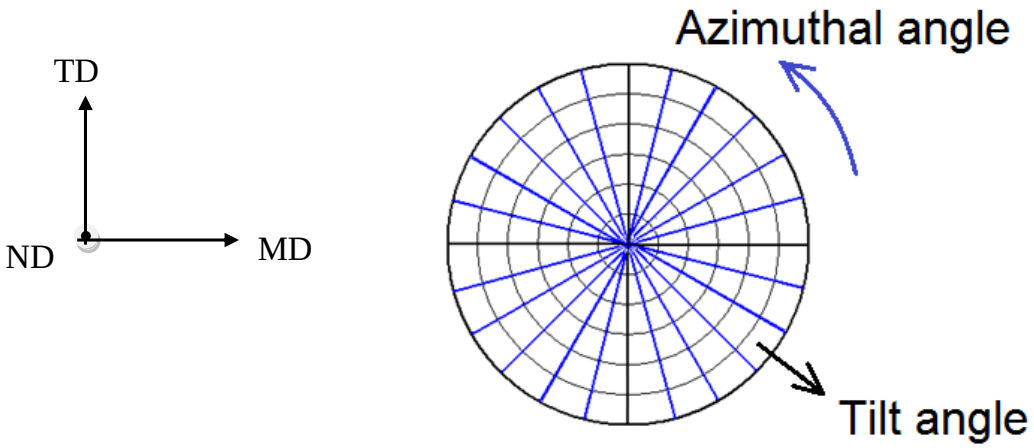

Figure 2.7: The reference directions and the 15^{o} net used for reading pole figures.

2.2.6 Tensile Tests

Tensile test specimens were cut for undrawn and drawn billets from the pilot-scale setup as per ASTM D638 type-I standard. Following the work by Mourad et al.[60], the length of

the tensile bars was kept higher than the standard (Figure 2.8) to avoid fracturing of the specimens at the grip regions.

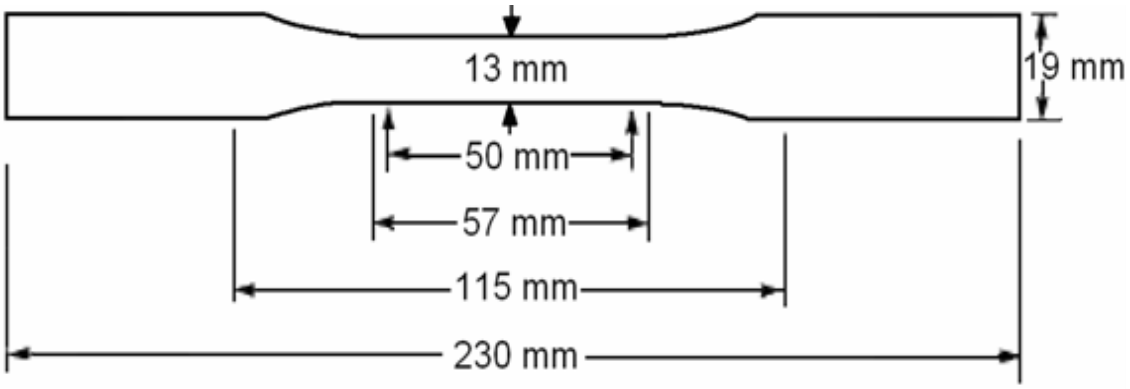

Figure 2.8: Schematic of ASTM D638- type I tensile bar with total length of 230 mm.

Tensile tests were carried out on the Universal tensile tester that was fitted with 20kN load cell and a 50 mm gauge length axial extensometer (Epsilon model-3542-050M-035-ST). All the tests were carried out at room temperature with a cross head speed of 5.08 mm/min. Experimental data in terms of load cell output and extensometer displacement were monitored using the data acquisition software Datum 4.0, installed on a personal computer. The captured data was then post-processed to obtain nominal stress-strain curves for tensile modulus determination.

2.2.7 Differential Scanning Calorimetry (DSC)

Differential scanning calorimetry (DSC) is a thermo-analytical technique in which a pan of given sample and a reference pan are subjected to a controlled temperature program; the changes of the differences in heat flow rate of the sample with respect to the reference are measured. The pan of a given experimental sample is prepared by taking 5-10 mg of

the polymeric substance and hermetically sealing it in an aluminum pan. The reference pan is just an empty sealed aluminum pan without any sample in it. When the sample is subjected to a specified temperature ramp (dT/dt), the instrument tries to maintain the reference at the same temperature as that of the experimental sample. The differential changes in enthalpy involved are recorded with time to produce a differential scanning calorimeter (DSC) curve. The DSC curve of a given thermoplastic material can provide information about its various thermal characteristics, such as glass transition temperature, melting temperature, crystallization temperature, crystalline fraction, etc.

Thermal properties of drawn and undrawn specimens were measured on a DSC-Q10 by TA instruments operated under a nitrogen purge of 50 ml/min. The DSC curve for a given billet sample was obtained by heating 5-10 mg specimen, from 40^{o}C to 200^{o}C, at a heating rate of 5^{o}C/min. Values of heat of fusion were obtained with the help of Universal Analysis 2000 software (version 4.5A) by TA instruments. The percentage crystallinity of a given sample was determined using equation 2.2.

$$\chi_c = \frac{\Delta H_f \cdot 100}{\Delta H_f^0 \cdot \omega_m} \qquad (2.2)$$

Where, χ_c is the total crystallinity, ΔH_f is the heat of fusion obtained in DSC test, ΔH°_f is the equilibrium heat of 100% crystalline polypropylene and ω_m is the weight fraction of the polymer in the material. The heat of fusion of 100% crystalline polypropylene was taken as 209 J/g for fully crystalline PP[61].

CHAPTER 3

DRAW STRESS AND MORPHOLOGY OF DIE-DRAWN PP-TALC COMPOSITES

3.1 Introduction

The deformation of a given polymeric material during its die drawing process takes place mainly in two zones[1, 37] a) within the converging die and b) in the post-die deformation zone outside the die. The amount of draw load required to make the material flow in the die zone is determined by its flow stress which essentially depends on its yield stress[38]. The yield stress of neat PP has been recorded to increase with increased strain rate[62-64] and decreased temperature [44, 62, 64] of drawing. In the die drawing operation, the amount of work required to draw a given billet would also depend on its volume and therefore its dimensions prior to drawing. For neat PP, the draw stress (ratio of steady die drawing load to final cross sectional area of the drawn billet) has been found to increase with nominal draw ratio of the die, applied draw rate as well as reduced draw temperature[65]. Mohanraj et al.[41] also observed a positive slope on the plot of draw stress vs. draw ratio for unfilled PP. When they plotted similar curves for die drawn billets of PP filled with low modulus elastomer, they noted that the slopes of these curves decreased with increasing content of the elastomeric phase. With the addition of untreated rigid particles, the yield stress of PP goes down[12-13]**.** Therefore, during die drawing of PP- composites loaded with rigid filler particles, the required draw stress is expected to be lower.

At the microscopic level, the damage in the material during die drawing of a given PP composite would take place by various micromechanical mechanisms such as shear yielding, cavitation in the matrix phase, debonding and crazing[21-23]. Among these the last three failures result in dilation of the material and hence a reduced density. Both experimental[15-19, 21-22] and numerical results[23] (using finite element method) suggest that for non-polar polymers such as PE and PP composites filled with untreated particles like glass beads or talc, debonding is the dominant mechanism of failure, as it requires lower stress than the other micromechanical mechanisms. Further deformation of the composite would lead to crazing, shear yielding and void growth. The dominance of one or the other mode depends on the temperature of drawing, interparticle distance and stress-strain state in the material.

3.2 Background

Room temperature tensile test studies[15-22] done on polymer composites filled with micron sized rigid particles have shown that during the drawing process, the particles get completely debonded from the matrix phase. This process of void initiation is then followed by void growth around the debonded particles. For lower filler content, the voids around the debonded particles grow independently. On the other hand for the composites filled with higher filler contents, the void growth around a given particle is affected by the stress-strain distribution around its neighboring particles[19]. Dubnikova et al.[19] observed that the void aspect ratio in the latter case was lower than the mean draw ratio of the drawn material. Examination of the trends on volumetric strain (ratio of

change in volume to initial volume of the material) vs. axial strain plots by other groups[15] indicated that the growth in the volumetric strain is proportional to the fraction of debonded particles. In short, the overall degree of void growth during composite drawing is largely decided by the extent and manner of particle debonding. The microscopic phenomenon of debonding is well documented and it is shown to be affected mainly by the following factors:

Residual Stresses: During its production, when a given polymer composite is cooled from the processing temperature to room temperature, thermal stresses develop in the material because of the higher coefficient of thermal expansion of the matrix phase than that of the filler phase[24, 66]. Therefore, the difference in the coefficients of thermal expansion is inversely proportional to filler fraction as a result highly filled composites will have lower thermal stresses and vice versa. In case of semicrystalline polymers, the residual stress is also induced by the phenomenon of crystallization[67]. The magnitude of the residual stress is directly proportional to the difference in the coefficients of thermal expansion, crystal volume fraction and the applied cooling rate[68]. The residual stresses developed in the material cause the matrix to shrink around the filler particles. Therefore, for a spherical rigid particle aloof from other particles embedded in a given polymer matrix, a negative radial stress exists around it. When the polymer composite is annealed to a high temperature, the thermal stresses in the amorphous domains would relax; however, the residual stresses in the material would go up due to some additional crystallization or crystal thickening[67] in the crystalline phase. When the composite is

subjected to a uniaxial tension, the residual stresses at the poles of the particles are balanced first. The mode of further damage in the material depends on the degree of interfacial adhesion, as well as the differences in the moduli of the two phases[68].

Degree of Interfacial Adhesion: For a low modulus (1-5 MPa) elastomeric composite filled with well-bonded spherical glass beads (treated with vinyl triethoxy-silane) under tensile stress, the initial failure appeared near the particle by internal rupture of the matrix and formation of a small vacuole. The vacuole formed in the matrix then grew and reached the surface of the particle resulting in its debonding from the matrix phase[17]. When this composite was filled with less-well bonded (untreated) and weakly bonded (ethylsilane treated) particles, debonding at the interface was found to be the dominant mechanism of failure. In case of a polar thermoplastic matrix (polystyrene with an elastic modulus of 3.25 GPa) composite filled with spherical glass beads (elastic modulus ~70 GPa), Heikens et al.[18] observed that under tensile loading, crazes formed at the poles of the glass bead transverse to the direction of tensile stress when the glass beads were excellently adhered (glass beads treated with Cationic vinylbenzylsilane) to the matrix phase. For the composite of this polymer, filled with weakly adhered glass beads (treated with Vinylsilane), the craze formation was preceded by interfacial debonding. Crazes at the interface for this case were observed between the pole and equator of the spherical glass bead at about 60^{o} to the direction of tensile stress.

Matrix Modulus: For elastomeric composites filled with spherical glass beads, Gent and Park[17] found that the debonding stress increased with increased modulus of the elastomer for a well bonded system. In contrast, for less well bonded and poorly bonded elastomeric

systems it decreased with decreased modulus of the elastomer. For polyethylene-$CaCO_3$ composite under tensile loading, Sudar et al.[69] observed a less number of debonded particles when the matrix used was softer. Moreover, they found that the sizes of the voids formed in this case were larger than those formed in the drawn composite with a stiffer polyethylene matrix.

Particle filler loading and characteristics: Experimental work by Vollenberg et al. showed that in the case of PP composite filled with glass beads, the debonding stress (φ_p = 25 %) increased linearly with $1/\sqrt{r_p}$ where r_p is the average particle radius. They did not notice any debonding for the composites that were filled with glass beads of average particle diameter less than 4μm. Renner et al.[12] found that for lower filler fractions, debonding of particles occurred at stresses much lower than the yield stress of the material. For higher filler fractions, debonding of particles occurred close to the yield point. Considerable plastic deformation of the composites started after the yield point. Dubnikova et al.[13] observed that in the case of PP composites filled with spherical beads of untreated aluminum hydroxide, below a filler volume fraction of 20%, the tensile specimens of the composite showed a different mode of deformation than for the composites with φ_p >20%. Plastic deformation of the former composites occurred macro-heterogeneously. Microscopic observations of the drawn composites revealed that the voids formed around the completely debonded particles were uniformly distributed, and had grown independently or in an uncorrelated manner along the drawing direction. The average ratio of void length (l_v) to particle length (l_p) was close to the mean draw ratio of the

plastically deformed neck. The composites with higher filler fractions, particularly the ones with bigger particles (8 μm and 25 μm) deformed homogenously. The narrow plastically deformed sections of these composites showed craze-like areas with micro voids nucleated in a correlated manner by the debonded particles. These areas were perpendicular to the drawing direction and were separated by bands of polymers. The average void stretch ratio for the voids in the craze-like areas was much smaller than the mean draw ratio of the plastically deformed section. Detailed experimental and numerical analysis by Oshmyan and Muravin[19] indicated that the critical volume fraction of particles above which the stress-strain distribution around one particle affects the stress strain distribution around its neighboring particles, is dependent on the particle size distribution.

3.2 Research Objectives

During the die drawing process of PP-talc composite, the required draw stress was expected to be lower due to decreased yield stress of the material. The reduced yield stress during composite drawing might be associated with an earlier onset and growth of crystal orientation of the matrix phase; this is the topic of discussion for Chapter 4. This chapter is dedicated to the study of microscopic events of debonding and void growth responsible for density reductions in the die drawn composites of PP filled with talc. In most of the literature papers discussed in the earlier section, the phenomena of debonding and void growth were studied at room temperature, using very low tensile strain rates. The strain rates and the test temperatures in these studies were way below those that are applied in the process of solid phase die drawing. Nonetheless, the observations and conclusions of these studies that were useful in drawing some general trends expected

during the elevated temperature die drawing of PP-talc composites. For weakly adhered filler particles (relevant to our study), debonding is the preferred mode of stress relief. When a polymeric composite with these inclusions is subjected to drawing, the maximum stress in the material gets concentrated at the poles of the particles. This stress is then relieved by void initiation or debonding at these sites. As shown in Figure 3.1, the debonded portion initially encompasses about a 20^{o} to 25^{o} region at each pole of the spherical particles[25].

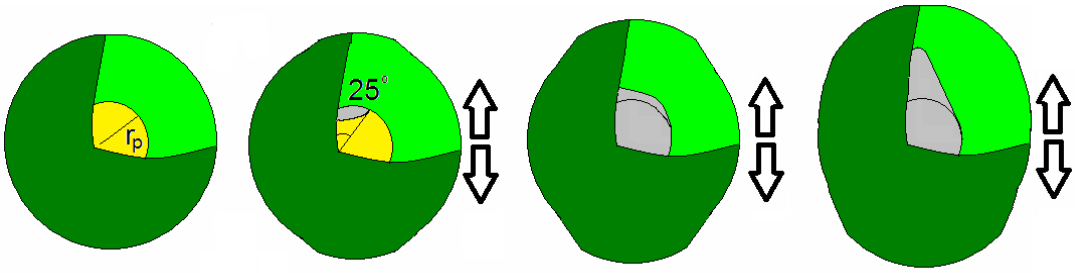

Figure 3.1: Schematic representation of different stages of void growth around an untreated particle in control volume element of a composite.

With continued drawing the debonding proceeds along the phase boundary until complete debonding of the filler particle from the matrix phase take place, and the void covers the entire surface of the filler [13,19-20,25]. At larger deformations, the voids around the debonded particles get stretched in the drawing direction[16-19, 25]. Under given processing conditions, the relative lengthening of the voids formed is decided by the filler fraction and the modulus of the matrix[15, 70]. Moreover, bigger particles have a tendency to debond first. For commonly used particle sizes, the debonding stress for untreated filler particles is lower than the yield stress of the filled material. If the particle size is

small, or if the interfacial adhesion between given particles and the matrix phase is strong, then the stress required to debond is higher and the matrix would undergo yield without debonding of the particles[16].

The phenomena of debonding and void growth can be tracked using a morphological approach as well as a phenomenological approach. The morphological approach[25, 71-12] is qualitative and involves visual observation of various morphological changes induced due to various processing conditions. The phenomenological approach[11-23] involves studying the tensile stress-strain and volumetric strain-axial strain relationship using the laboratory scale tensile testing equipment. In our study, we took the morphological approach. The objective of was to investigate the void content and nature of voids formed in the die drawn composites of PP that was filled with two different filler loadings of micron sized talc particles. For a fixed talc concentration, the effect of draw rate on void volume fraction and void shape was also studied.

3.3 Experimental

3.3.1 Materials

The polymeric matrix used to study deformation and void morphology of solid state die-drawn composites was isotactic polypropylene (i-PP) homopolymer (Dow grade 5D37) with a density of 0.905 g/cc and a melting temperature of 166(±2)^{o}C. The polymer had a M_W of 249400, a polydispersity index of 4.7 and a melt flow rate of 2.8 g/ 10 min. Two grades of untreated talc particles were used as fillers. The first grade, TC-100 by Luzenac, was used to mold composite billets for lab-scale die-drawing runs. The talc had a specific

gravity in the range of 2.7 to 2.8; the median equivalent spherical diameter of the talc particles was 16.4 microns. Another grade of talc-FDC by Luzenac was used to mold billets for pilot scale-die drawing runs. This grade of talc had a more controlled particle size, with a median equivalent spherical diameter of 18 microns. The particle size distribution for this talc is shown in Figure 2.1. The sp. Gravity of the talc was 2.8 and it had a surface area of 1-2 m^2/g.

3.3.2 Procedures

3.3.2.1 Die Drawing Runs

Two different sized billets, with two different filler loadings were molded as per the procedure given in section 2.2.1. The small billet which had 38 wt. % (or 16.5 vol. %) of Luzenac TC-100 talc was die-drawn on the lab-scale setup; and the big billet which had 20 wt. % (or 7.5 vol. %) of Luzenac FDC grade talc was die-drawn on the pilot-scale setup. The lab scale die-drawing run with the small billet was performed using a wedge die of nominal draw ratio 3.2, at a draw temperature of 150^oC, with five different draw rates viz. 2.54 cm/min, 12.7 cm/min, 25.4 cm/min, 50.8 cm/min and 101.6 cm/min. The wedge die had a converging portion that was 7.62 cm long and a die-land that was 2.54 cm long. The load cell on the pulling unit recorded force vs. displacement for a given draw rate. Billets drawn to the lengths of 30.48 cm were cooled using a freeze spray before cutting (see section 2.2.2.1 for additional details) ~4cm away from the die exit. The pilot scale die-drawing run with the big billet was performed using a wedge die of nominal draw ratio 2, at a draw temperature of 145^oC, with four different draw rates of industrial importance: 91 cm/min, 244 cm/min, 366 cm/min and 573 cm/min. The wedge

die used was 2.6 cm long and didn't have any die-land. For each draw rate, the drawn billet coming outside of the die was cooled with a water spray tank maintained at 23^{o}C. Additional details of the process can be found in section 2.2.2.2.

3.3.2.2 Characterization

The drawn samples from both lab scale setup and pilot scale setup were analyzed for a given draw rate farther from the die exit. Billet specimens measuring 1.5 cm and 2 cm in length along the drawing direction were cut from the billets of lab-scale setup and pilot-scale setup respectively.

3.3.2.2.1 Density Measurements

Densities of the samples before and after die drawing were measured using the Sartorius density determination kit –YDK-01, as described in section 2.2.3.

3.3.2.2.2 Morphological Study

Cryogenically cracked specimens of drawn billets were viewed under JEOL JSM-6400 scanning electron microscope, according to the procedure given in section 2.2.4. Morphologies of the specimens from lab scale die drawn billets were viewed in the MD-ND plane. For the specimens of the billets from pilot die drawn runs, morphologies were viewed in both the MD-ND plane as well as the MD-TD plane. The two crack planes are shown schematically in Figure 2.5.

Die drawn composites from the pilot-scale setup were further analyzed for the dimensions of the voids formed. The dimensions of the particles and voids in all of the SEM pictures were measured with the help of image analysis software – ImageJ (version:

1.43). Histograms of the measured dimensions were plotted using statistical analysis software- Minitab16.

3.4 Results and Discussion

3.4.1 Draw Stress

Figure 3.2 shows a plot of force vs. displacement measured during die drawing of the PP-talc-38 wt. % composite billet at 101.6 cm/min on the lab-scale die drawing setup.

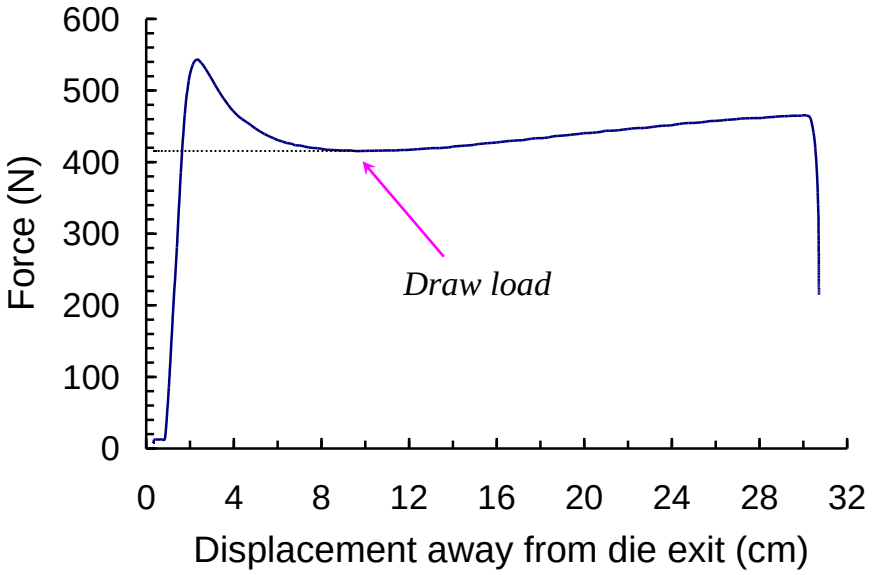

Figure 3.2: Drawing force vs. displacement during die drawing of PP-talc-38 wt. % composite for the draw rate of 101.6 cm/min.

The measurements made for different draw rates showed similar trends on their load displacement curves; the die drawing loads were lower for the lower draw rates. The draw stress for a given draw rate was calculated by dividing the draw load by the cross-sectional area of the drawn billet. During the die drawing runs of PP-talc-38 wt. % composite, the draw stress increased and the density decreased with increased draw rate, as shown in Figure 3.3.

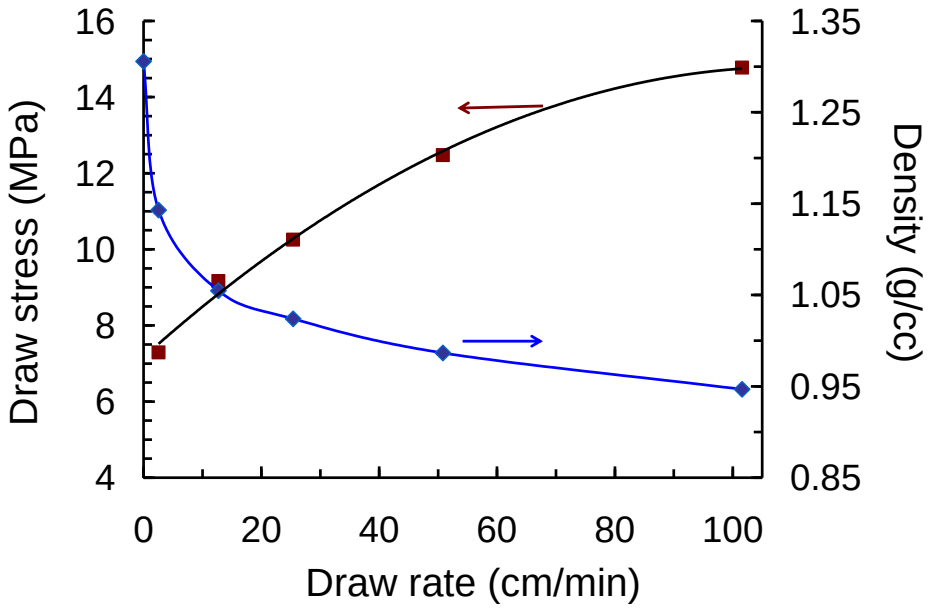

Figure 3.3: Variation in die drawing stress and density for drawn PP-talc-38 wt. % composite as a function of draw rate.

For the billets drawn to the same extents, higher draw ratios and/or strain rates attained with higher draw rates must be the main reason for the observed trends. The actual draw ratios (DR) of the drawn samples were calculated using Equation 1.1 and are presented in Figures 3.4 and 3.5 as a function of draw rate. Area ratios corresponding to these figures are given in the Figures A.1 and A.2 of Appendix A. Because of the free tensile drawing of the billets outside the die, the actual draw ratios obtained for the drawn samples were higher than the nominal draw ratio of the die used. Despite the lower nominal draw ratio of the die, the actual draw ratios obtained for PP-talc-20 wt. % composite drawn on the pilot-scale setup were relatively higher- primarily because of the higher draw rates employed for drawing this material.

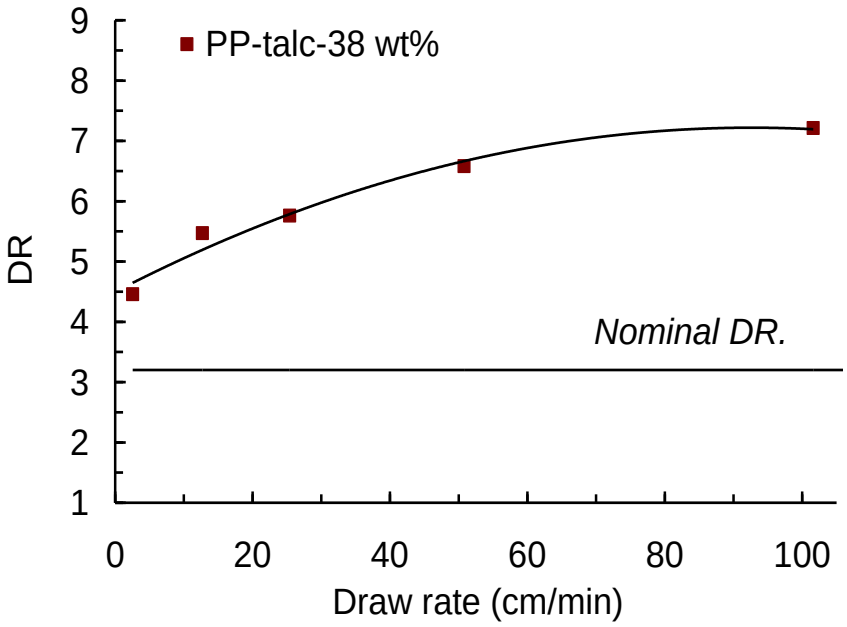

Figure 3.4: Actual draw ratio vs. draw rate for die drawn PP-talc-38 wt. % composite.

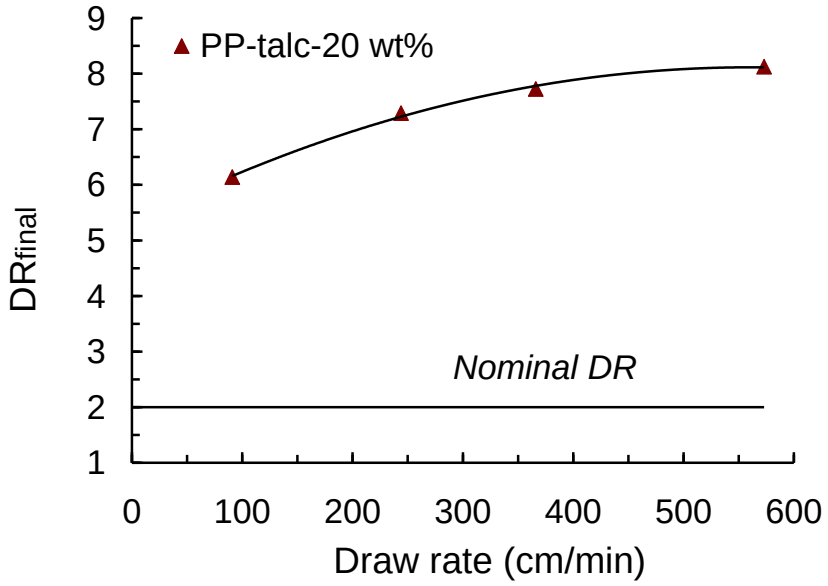

Figure 3.5: Actual draw ratio vs. draw rate for die drawn PP-talc-20 wt. % composite.

The draw stress during composite drawing increased linearly with draw ratio as shown in Figure 3.6.

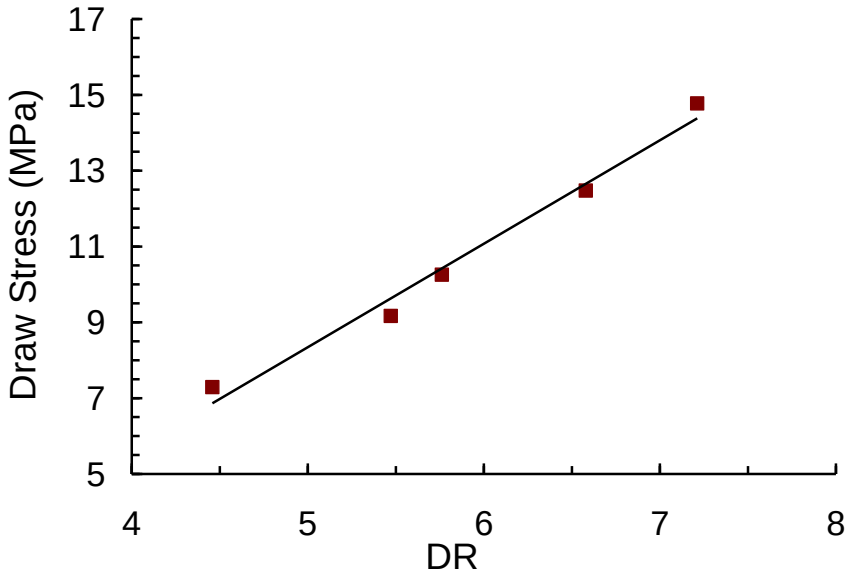

Figure 3.6: Draw stress vs. draw ratio for drawn PP-talc-38 wt. % composite.

Taraiya et al.[65] have reported a linear relationship between draw stress and draw ratio for unfilled or neat PP drawn at various temperatures. They found that for neat PP, the slopes of the lines decreased with increased draw temperatures. From their work, the slope of the line for neat PP drawn at 155^{o}C is seen to be ~6 MPa, which is more than twice the slope we saw (2.7 MPa) for the die drawn PP-talc-38 wt. % composite drawn at 150^{o}C. From these results it can be concluded that in die drawn composites, we can get equivalent draw ratios as that of drawn neat PP by applying lower levels of draw stresses. This is expected because for similar processing conditions the yield stress or the plastic flow during composite drawing sets in at a lower stress levels than the neat polymer[11-14, and 16].

3.4.2 Void Growth

As described in the introduction, during die drawing runs in our study, the materials underwent deformation in the die zone and in the post-die zone. The deformation in the post-die zone was controlled by forced cooling, using a freezer spray for the smaller billets drawn on the lab-scale setup and using a water spray tank for the bigger billets drawn on the pilot-scale setup. For discussion purposes, the draw ratio calculated for a sample of drawn billet at the final location (where the deformation was almost complete) is called the DR_{final}. Figures 3.7(a)-(b) show that the die drawing runs on the lab-scale setup, as well as on the pilot-scale setup, led to saturation in density or the void volume fraction above a DR_{final} of 7.

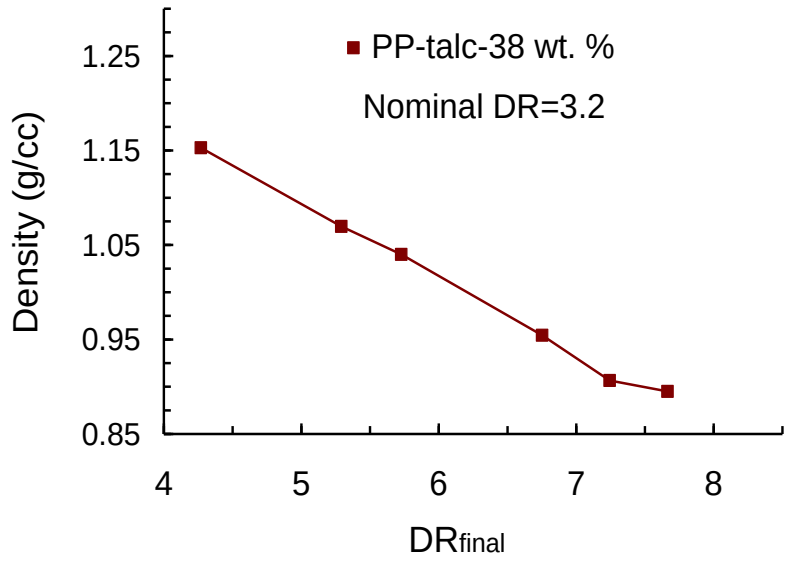

(a)

Figure 3.7: Density vs. DR_{final} for (a) PP-talc-38 wt. % composite drawn on lab-scale setup and (b) PP-talc-20 wt. % composite drawn on pilot-scale setup.

Figure 3.7 (cont'd).

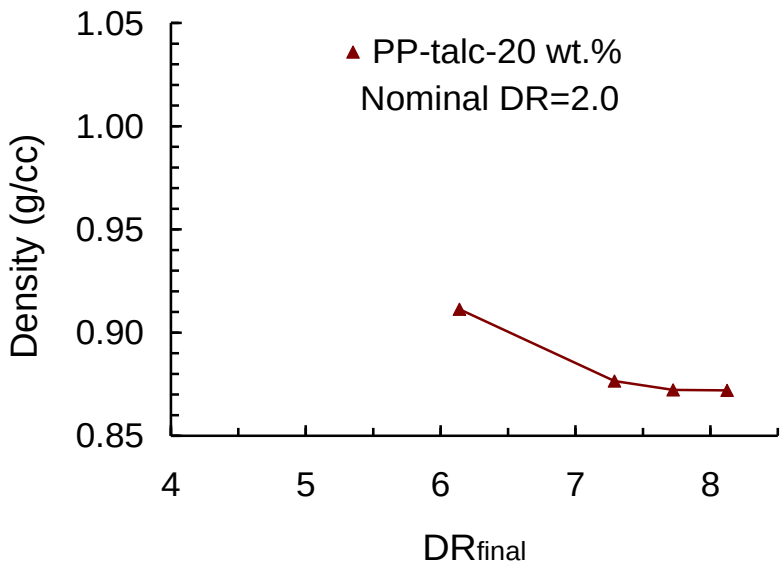

(b)

The increment in the values of DR_{final} for higher draw rates was gradual and for saturated density levels it was mainly due to a slightly higher reduction in the cross-sectional areas at these draw rates. The final void volume fraction calculated using density measurements, was 30 % for die drawn PP-talc-38 wt. % composite and 17 % for die drawn PP-talc-20 wt. % composite. The ratio of final void fraction to initial filler volume fraction was found to be lower (1.81 vs. 2.26) for the drawn composite with higher talc loading. Room temperature tensile tests[9-17] on PP composites with different filler loadings of big micron sized particles have frequently shown that the debonding of particles for the composites with higher filler loadings occurs close to the yield point. Once the material yields and deforms plastically, further deformation leads to void growth around the debonded particles. The observed differences in the above discussed ratios of the drawn composites could be due to the differences in their stress amplification

factors. Higher stress amplification in the case of composite with higher talc loading might have led to an earlier yield of the material, permitting only a fraction of particles to get debonded from the matrix phase. SEM images in the MD-ND plane of the die drawn samples obtained on the lab-scale die drawing line and the pilot-scale die drawing line are presented in Figure 3.8(a)-(b) and Figure 3.9(a)-(b) respectively. The drawing direction for each sample is indicated by a two headed arrow in the right corner of the image.

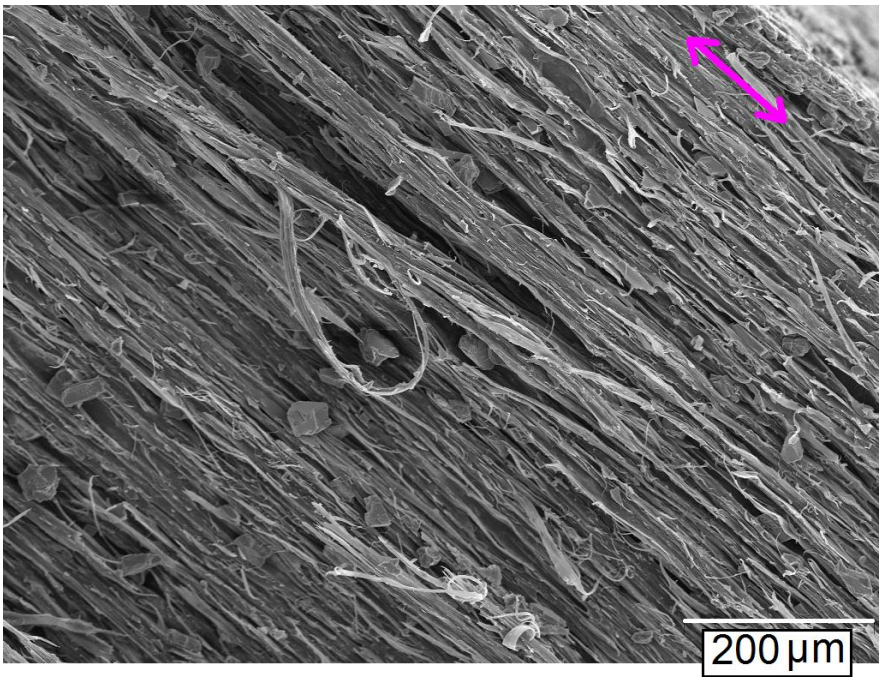

(a)

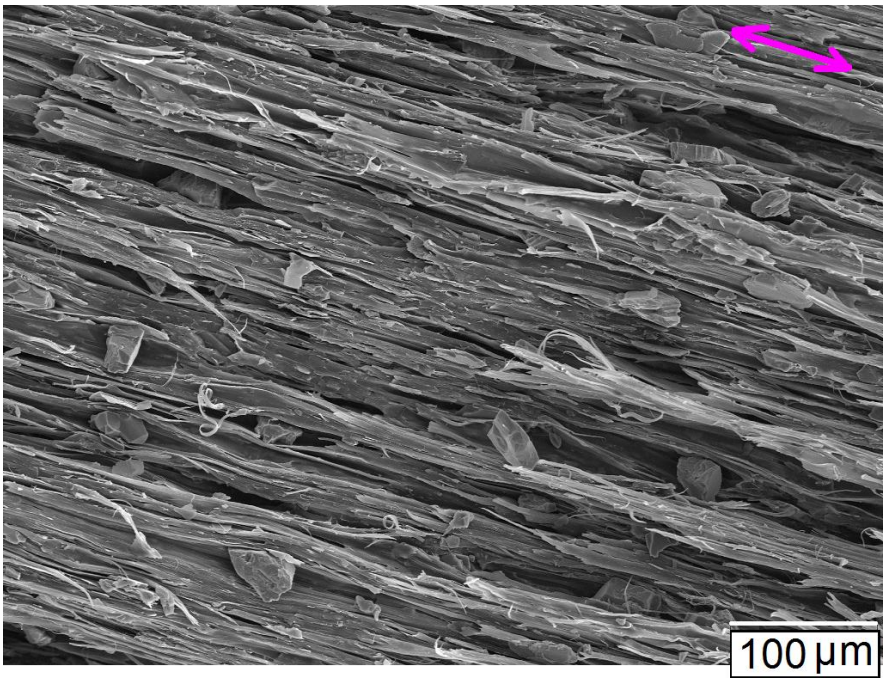

(b)

Figure 3.8: SEM images of PP-talc-38 wt. % composite drawn on lab-scale setup with a draw rate of (a) 12.7 cm/ min, DR_{final}=5.3(scale bar =200 µm) and (b) 50.8 cm/min DR=6.6 (scale bar =100 µm)

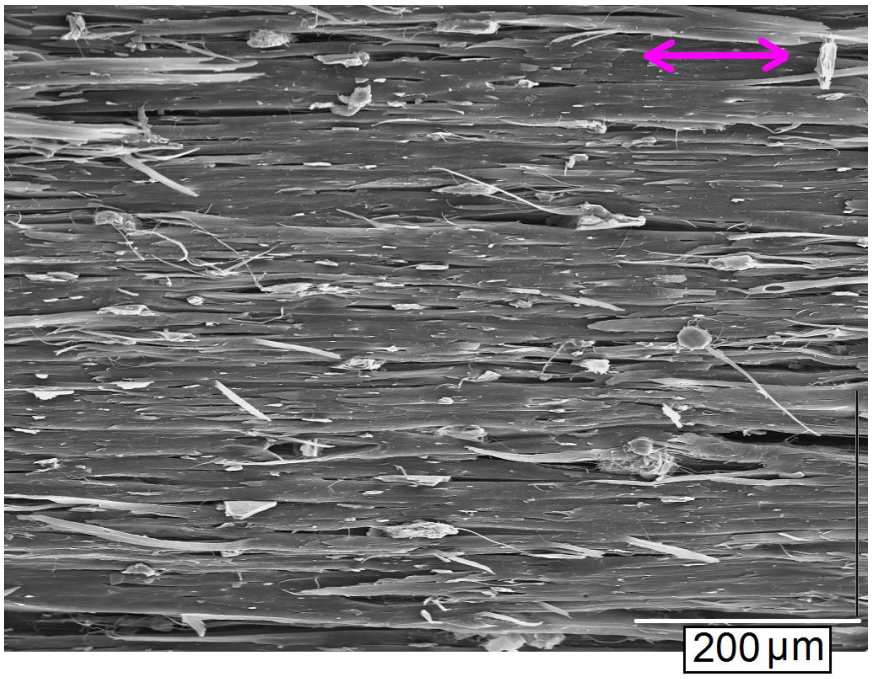

(a)

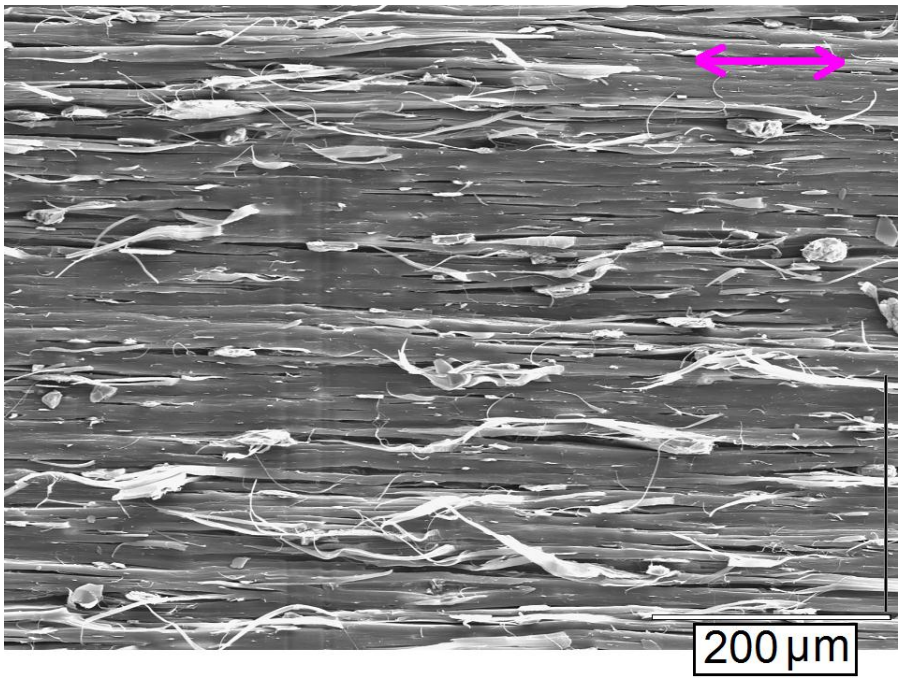

(b)

Figure 3.9: SEM images of PP-talc-20 wt. % composite drawn on lab-scale setup with a draw rate of (a) 91.4 cm/ min, DR_{final}=6.1 (scale bar =200 µm) and (b) 573 cm/min DR=8.1 (scale bar =200 µm)

Morphological images of the drawn composite samples did not show any particles that were bonded to the matrix phase. All the particles in these images were seen debonded and trapped inside the elongated voids. The voids were stretched in the drawing direction, and voids with higher stretch ratios were seen at higher values of DR_{final}. Unlike the samples of die drawn PP-talc-38 wt. % composite, the polymer ligaments in the die drawn samples of PP-talc-20 wt. % appeared much more intact. The cracked surfaces in the former case were severely torn; a relatively larger number of particles had left these surfaces. The differences in the voids formed in the two drawn composites can be highlighted with the help of SEM images filled with colors, see Figure 3.10(a)-(b). Figure 3.10 (a) corresponds to the SEM image given in Figure 3.8 (a) and Figure 3.10 (b) corresponds to the SEM image given in Figure 3.9 (a).

In addition to a lower interparticle distance in die drawn PP-talc-38 wt. % composite, the highlighted areas also indicate that the void thickness around the debonded particles was relatively higher. There was a wider distribution of void lengths due to coalescence of voids in some areas. This effect, combined with the highly uneven surface of the cryogenically cracked samples made it difficult to measure the void dimensions with enough accuracy. From the void morphologies, it seems that stress in the composite was largely concentrated in the pole, as well as equatorial regions of the flake shaped talc particles. This type of stress distribution must have led to a slight triaxial debonding of the particles and voids of lower aspect ratios. The presence of voids of higher aspect ratios in the die drawn samples of PP-talc-20 wt. % composite suggests concentration of the stress points mainly in the pole areas of the particles. The stress distribution in drawing of this composite must have been more of tensile or uniaxial in nature.

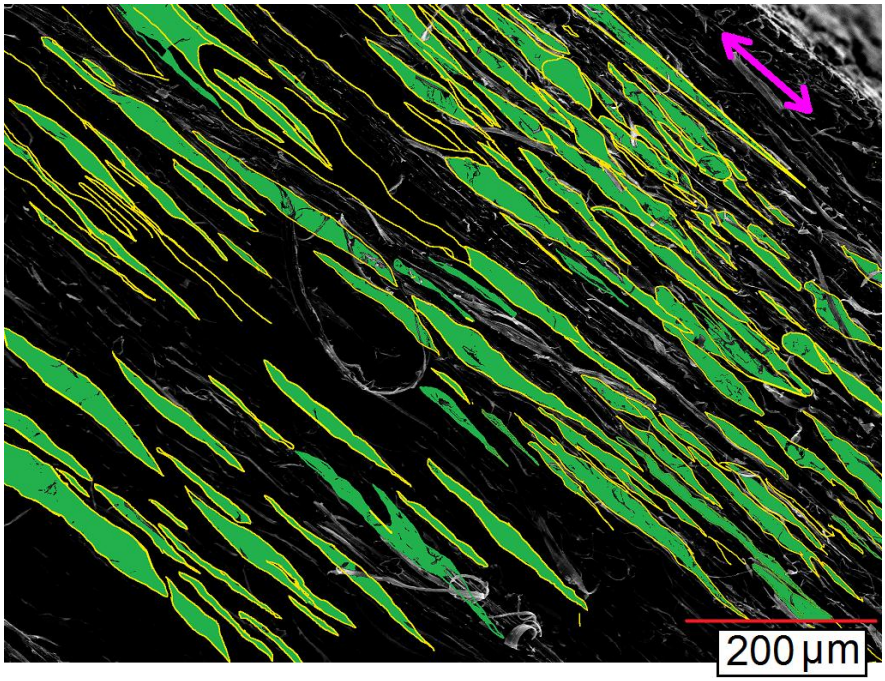

(a)

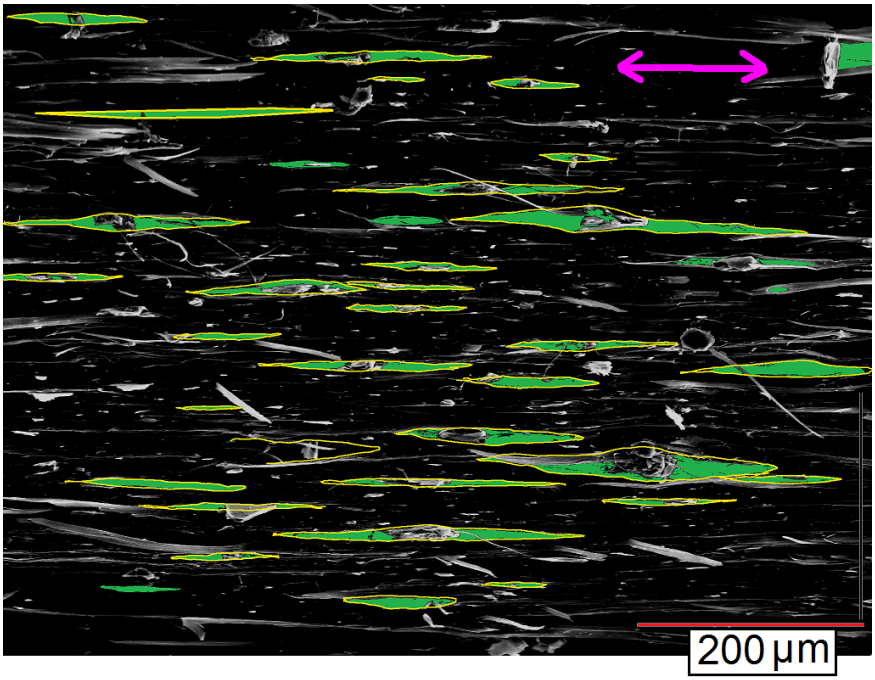

(b)

Figure 3.10: Colored SEM pictures of (a) drawn PP-talc-38 wt. % DR_{final}=5.3 (scale bar =200 µm) and (b) drawn PP-talc-20 wt. % DR_{final}=6.1 (scale bar =200 µm)

The void dimensions of the die drawn composite with lower talc loading could be measured with better accuracy, so more SEM images of these samples were obtained both in the MD-ND as well as in the MD-TD planes. Microscopic images of PP-talc-20 wt. % composite before and after die drawing at a draw rate of 366 cm/min are shown in Figure 3.11(a)-(b) and Figure 3.12(a)-(b). When observed in the MD-ND plane (Figure 3.11), the particles in drawn PP-talc-20 wt. % composite were seen well trapped inside the voids. When the specimens of drawn samples were cracked for viewing their MD-TD planes (Figure 3.12), the particles could not be confined inside the voids. The dimensions of voids in the TD-ND plane (plane perpendicular to the MD) were assumed to be same as that of the particles trapped inside them. Based on the visual examination of SEM images given in Figures A.3 to A.6 in Appendix A, as well as many other additional images (not presented here) this assumption seemed reasonable.

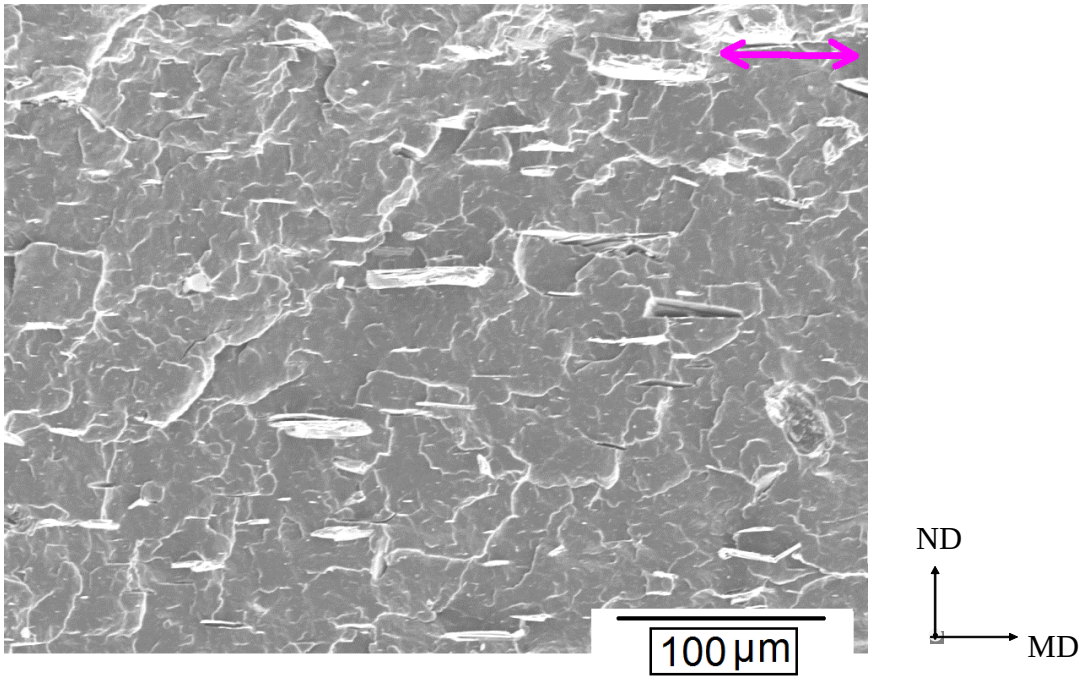

(a)

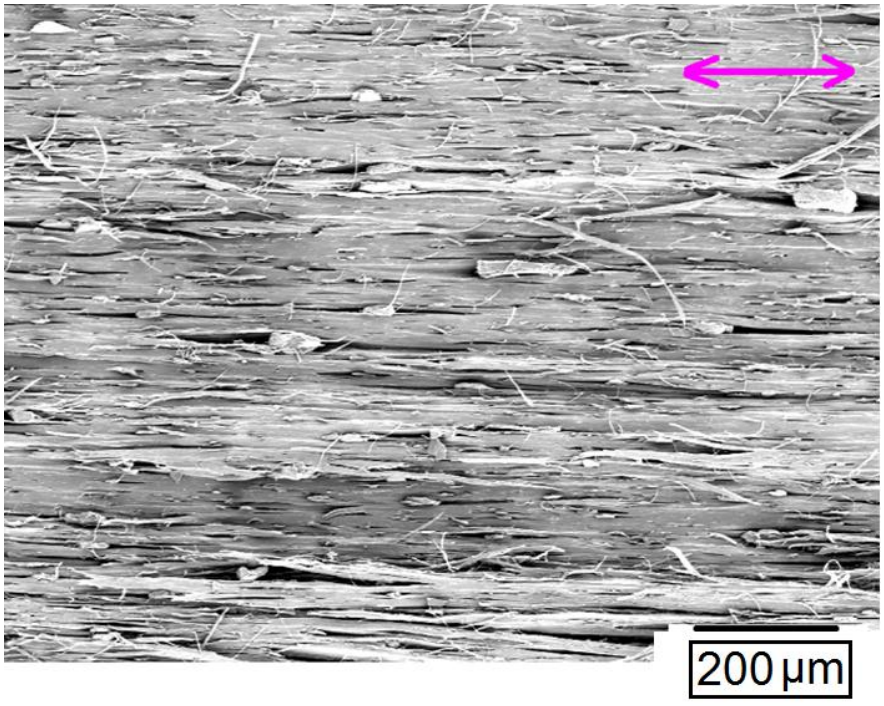

(b)

Figure 3.11: SEM images of MD-ND planes for (a) undrawn PP-talc-20 wt. % (scale bar =100 µm) and (b) drawn PP-talc-20 wt. % DR_{final}=7.7 (scale bar =200 µm)

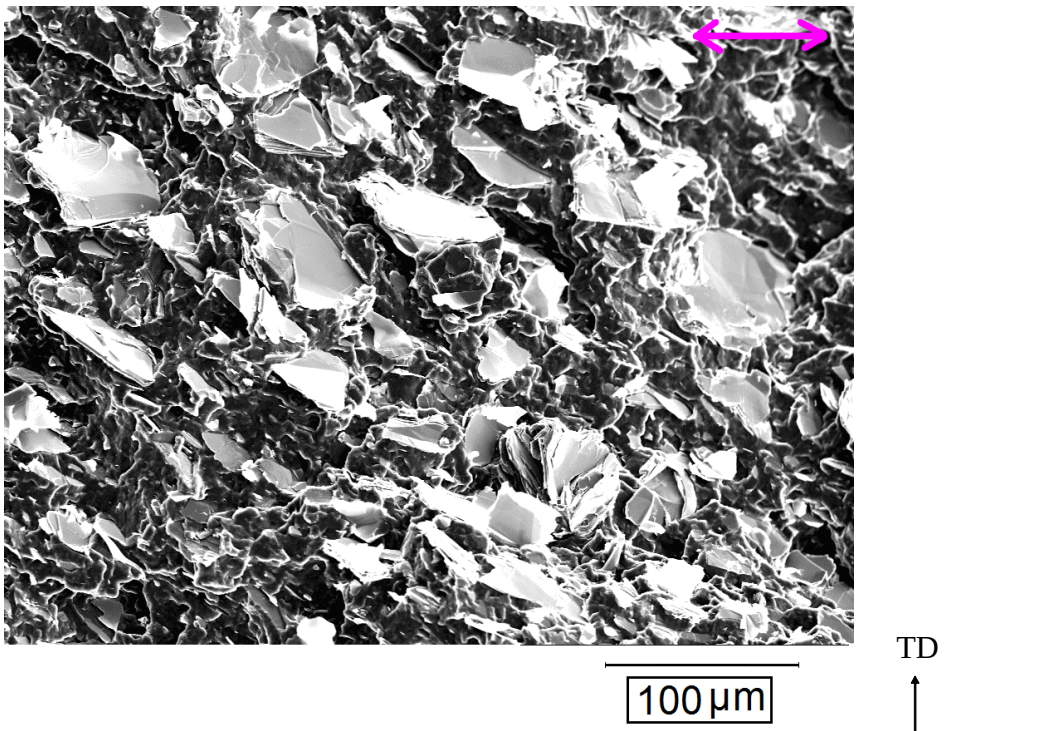

(a)

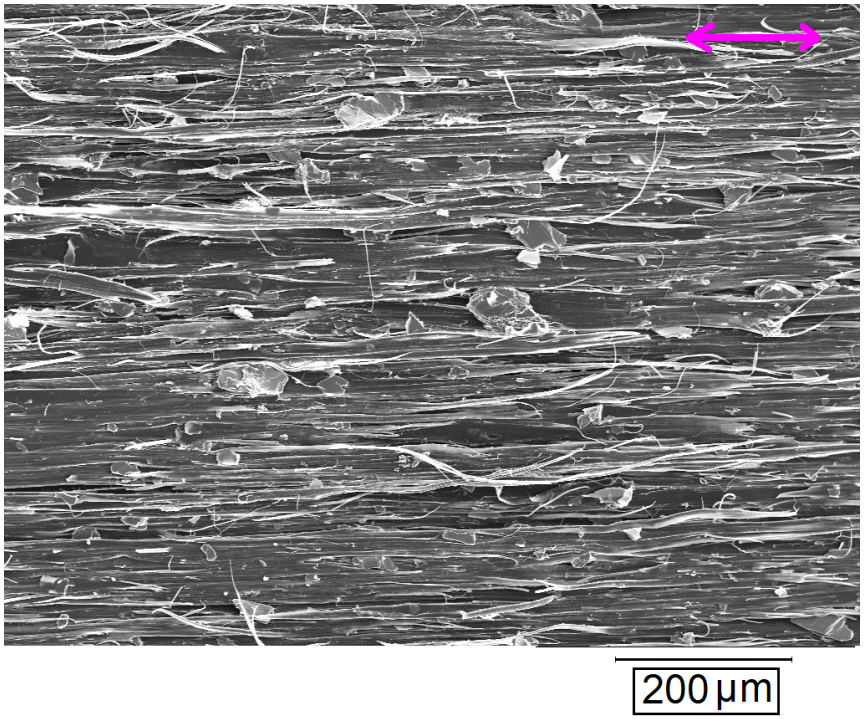

(b)

Figure 3.12: SEM images of MD-TD planes for (a) undrawn PP-talc-20 wt. % (scale bar =100 µm) and (b) drawn PP-talc-20 wt. % DR_{final}=7.7 (scale bar =200 µm)

Histograms of the particle dimensions for more than 1800 talc particles in each of the MD-ND and MD-TD planes of the drawn samples are given in Figure 3.13 and Figure 3.14 respectively.

It was clear that for the most part, the particles were oriented with their longest dimension along the MD and the shortest dimension along the ND. The average particle size of these elliptical disc shaped particles was found to be 37 x 14 x 7.5 (μm^3).

For each draw rate, histograms of void stretch ratios (i.e. the ratios of measured void lengths to the corresponding particle lengths) in the MD were obtained; these are presented in Figure 3.15 (a)-(d). The average void stretch ratio against the final DR is plotted in Figure 3.16. As seen there, both the void stretch ratio as well as the density ratio leveled above an actual draw ratio of 7. The final void lengths were 4-6 times that of the particle lengths. The details on how the final draw ratios affect the crystal orientations and tensile moduli of the drawn products are covered in the next chapter.

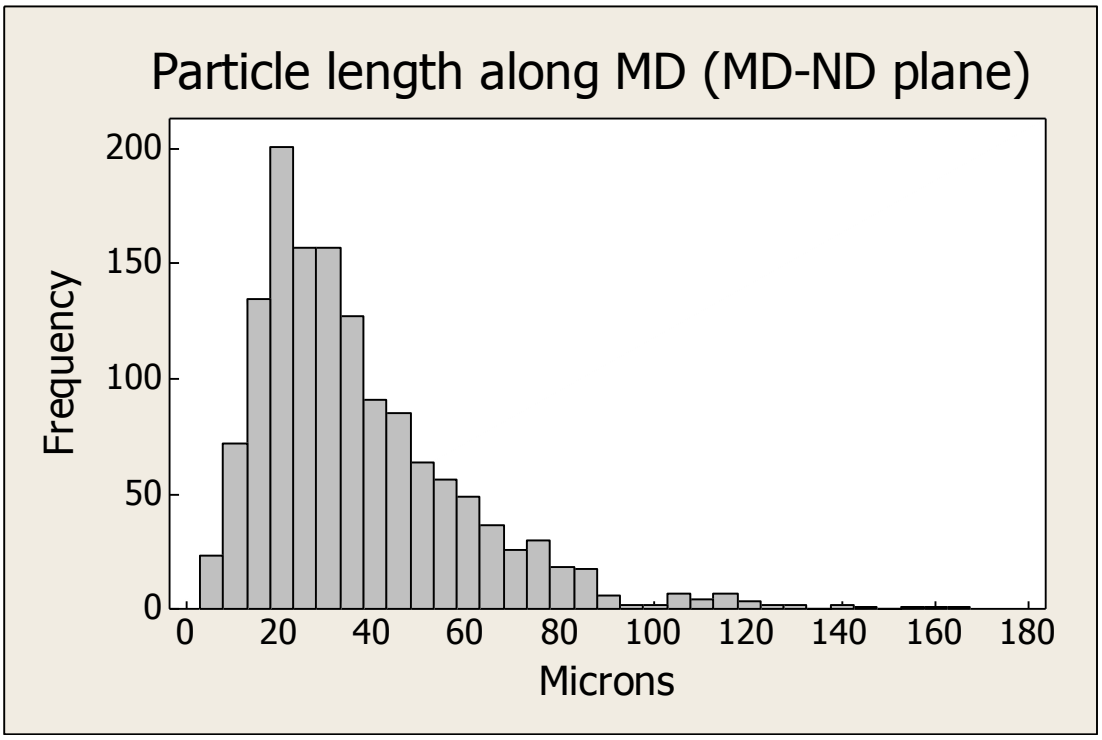

(a)

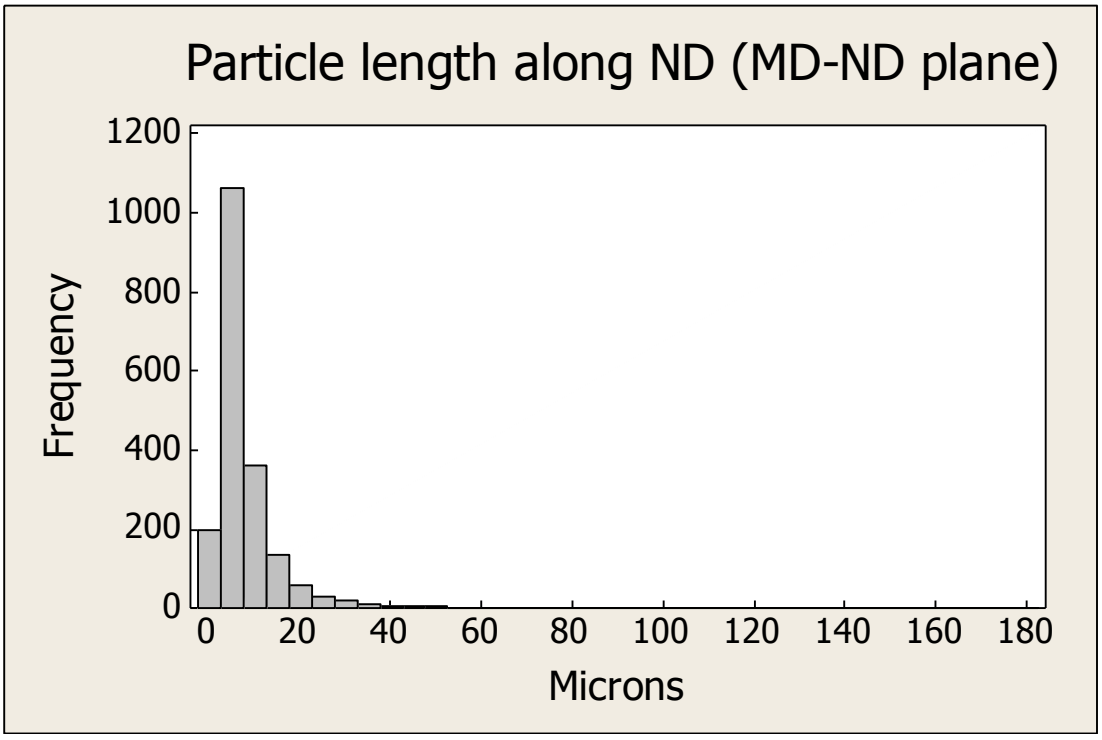

(b)

Figure 3.13: Particle lengths (a) in MD and (b) in TD measured in MD-ND planes for pilot die drawn samples.

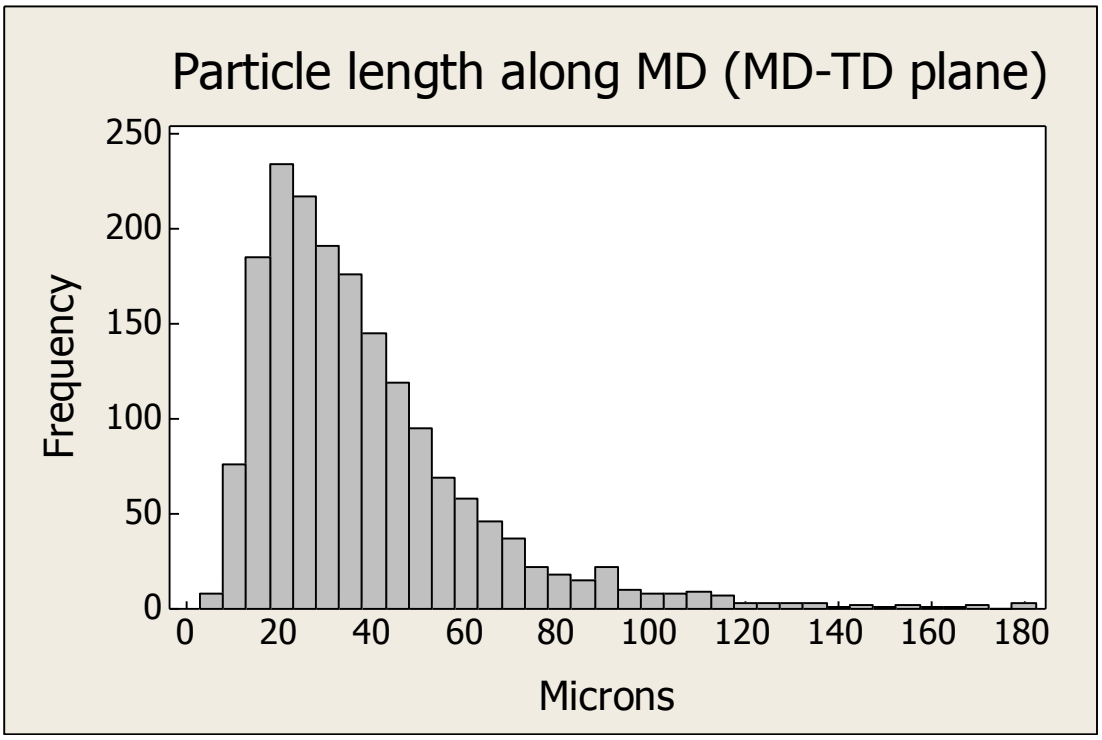

(a)

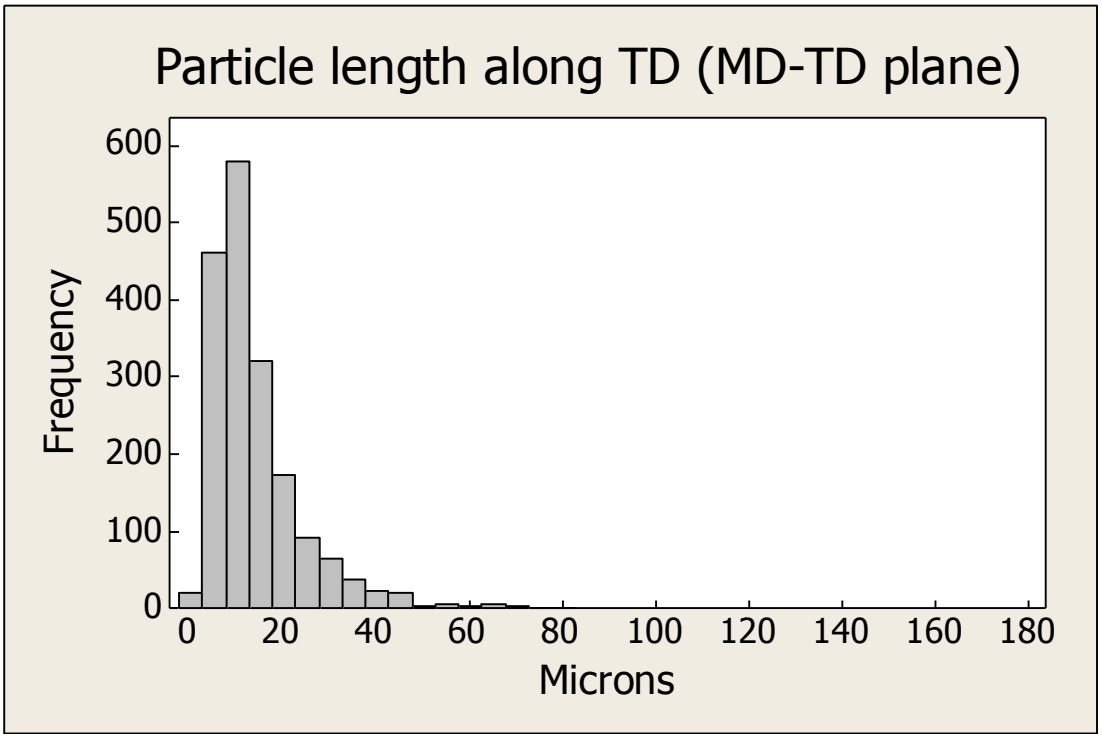

(b)

Figure 3.14: Particle dimensions measured in MD-TD planes of pilot die drawn samples.

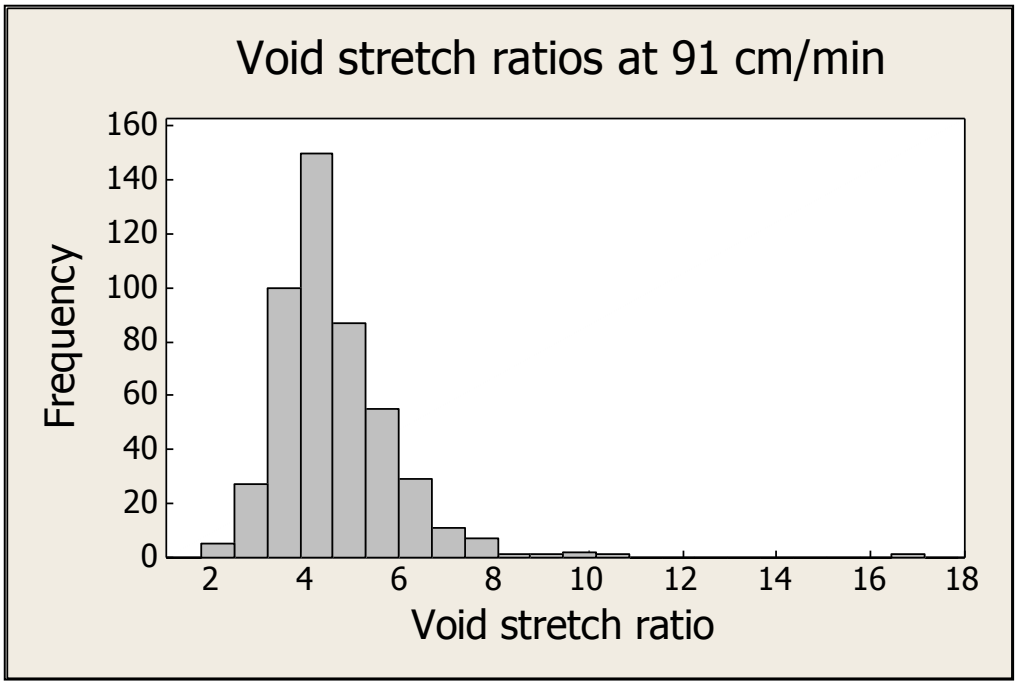

(a)

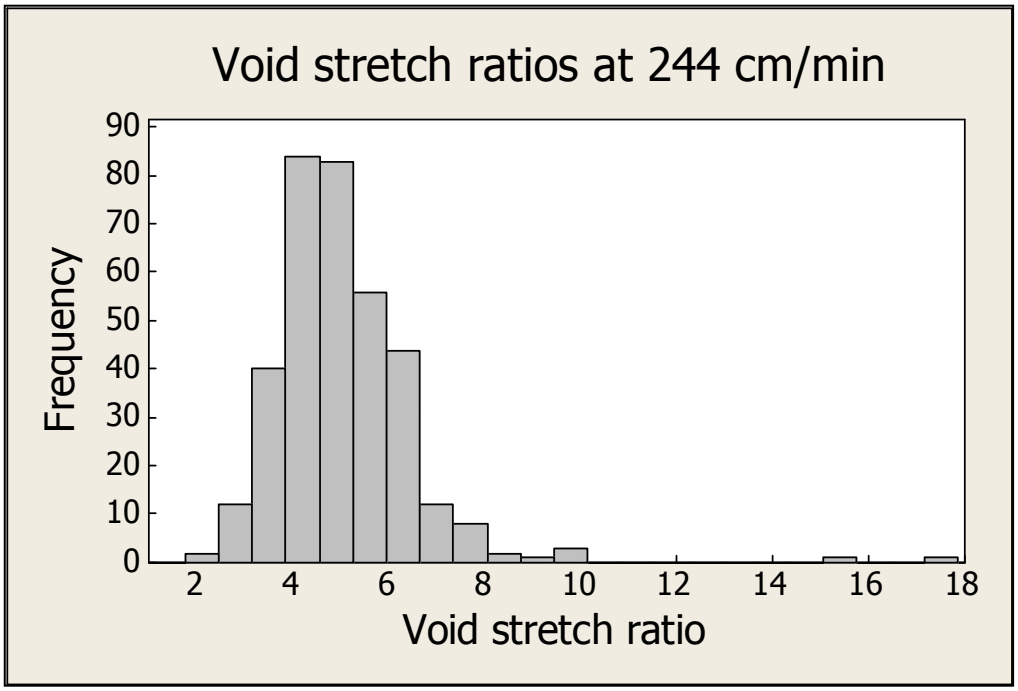

(b)

Figure 3.15: Histograms of void stretch ratio for PP-talc-20 wt. % composite samples drawn on the pilot-scale setup at (a) 91, (b) 244, (c) 366 and (d) 573 cm/min.

Figure 3.15 (cont'd).

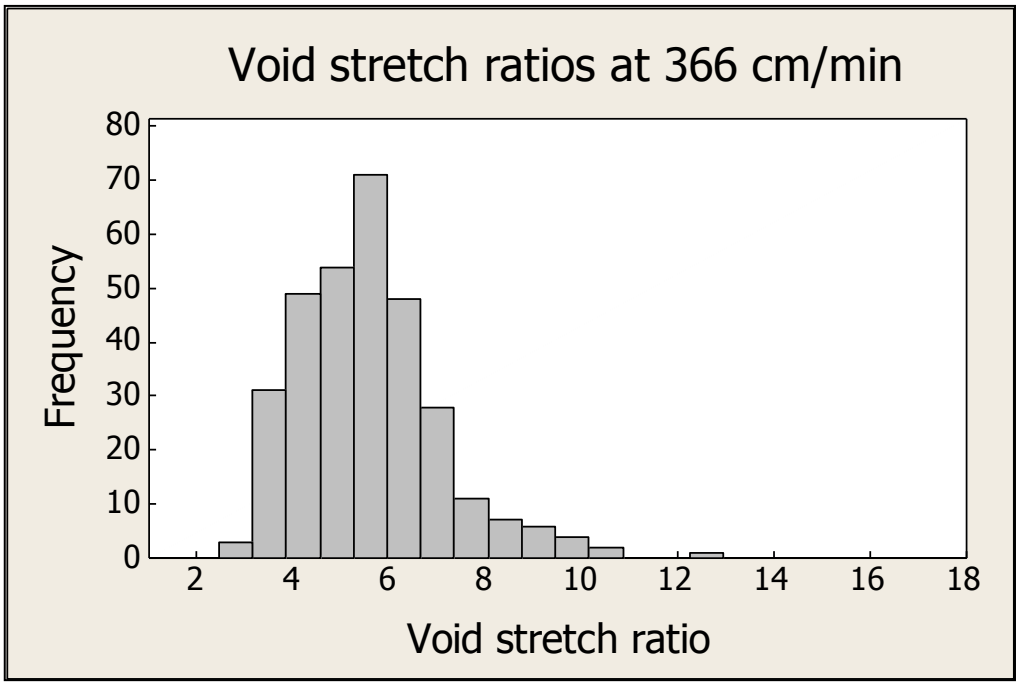

(c)

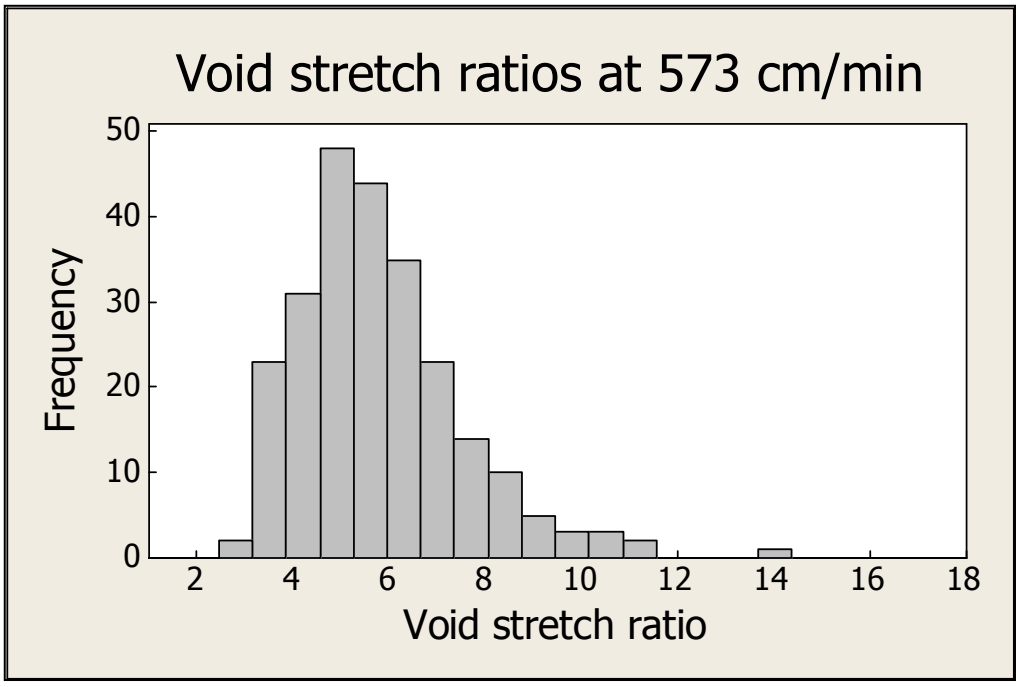

(d)

3.5 Conclusions

During elevated temperature die-drawing of PP-talc composite, the draw stress increased linearly with draw ratio. Die drawing runs with the lab-scale setup as well as the pilot-scale setup led to saturation in density or in void volume fraction above an actual DR of 7, as given in Figure 3.16. At higher draw rates, the increment in the values of DR_{final} was gradual, and for saturated density levels it was mainly due to an increase in the area ratios of the drawn billets. The final void volume fraction calculated using density measurements was 30 % for drawn PP-talc-38 wt. % composite and 17 % for drawn PP-talc-20 wt. % composite. The ratio of final void fraction to initial filler volume fraction was found to be lower (1.81 vs. 2.26) for the drawn composite with higher talc loading. Morphological analysis of the drawn samples showed that all of the particles were debonded and the voids around them had grown in the drawing direction. Visual examination of the SEM images indicated that the voids formed in drawn composite with a higher talc loading had lower aspect ratios and wider distribution of stretch ratios. In the MD, the lengths of voids formed in drawn PP-talc-20 wt. % were 4-6 times that of the lengths of particles trapped inside of them. The average void stretch ratio in these composites saturated above an actual DR of 7 (Figure 3.16).

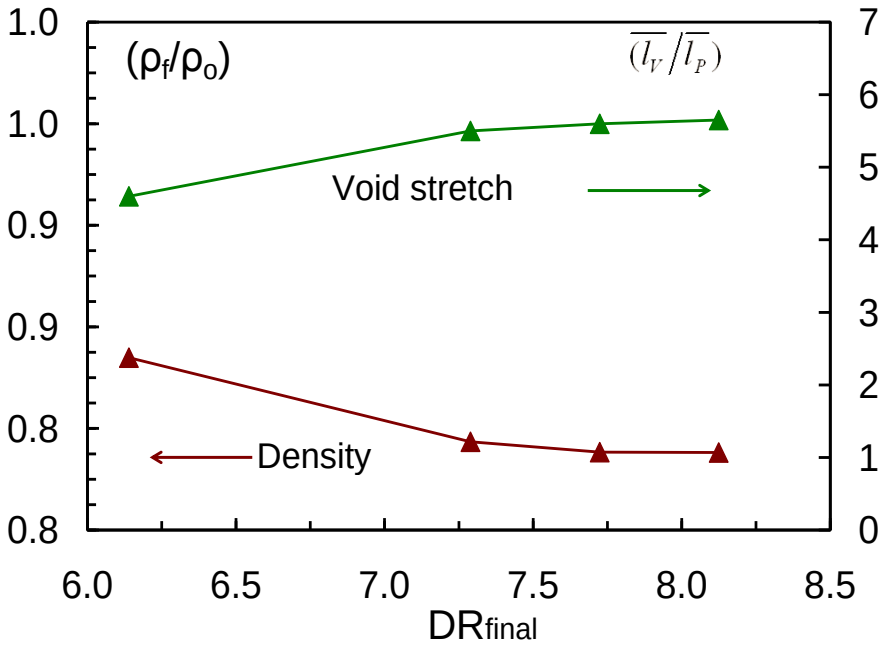

Figure 3.16: Density ratio (final/initial) and void stretch ratio vs. DR_{final} for drawn PP-talc-20 wt. % composite.

CHAPTER 4

CRYSTAL ORIENTATION AND MODULUS OF DIE DRAWN PP-TALC COMPOSITE

4.1 Introduction

4.1.1 Crystalline Morphology of PP-talc Composites

Isotactic polypropylene contains hierarchical polycrystalline structures[26-36] such as various levels of micro-scale spherulites, axialites or shish-kebabs, nano-scale crystalline lamellae and atomic-scale crystal unit cells with different packing geometries like monoclinic (α), trigonal (β), triclinic (γ) and smectic (δ). The stacks of lamellae are separated by highly disordered amorphous domains, and within the stacks the lamellae are separated by thin sections of amorphous phase which contains tie chains. The fractions of various structures in a given sample of PP are decided by the material factors such as its molecular weight and molecular weight distribution, presence of foreign particles, as well as the external factors, such as temperature and stress-strain profiles to which the polymer is subjected. Foreign particles like nucleating agents or fillers, when present in the material, provide high nucleation densities during the crystallization of the polymeric melt and force the crystals to grow in one direction: perpendicular to the fiber surface. This type of forced crystallization typically results in formation of layers with columnar crystals known as transcrystals[73]. Since the transcrystals are formed on the filler surfaces, reinforcements that have higher surface areas are more likely candidates to give greater amounts of transcrystalline regions. Quan et al.[74] have reviewed the literature on transcrystallinity to study different mechanisms responsible for the

formation of transcrystals. Most of the studies in their review have reported transcrystallinity in the case of polymeric composites filled with reinforcing fibers; however, this is not always a necessary criterion. Transcrystalline regions have also been found in the composites filled with particulate fillers such as talc, copper, aluminum, etc. From the summary of their work, it can be concluded that the extent and nature of the transcrystalline regions are composite specific and are decided by the filler fraction, molecular weight of the semicrystalline polymer, differences in the thermal conductivities, moduli and surface energies of the two phases, nucleation ability of the substrate, residual stress in the material and the applied cooling rate.

The morphology of the matrix phase in PP-talc composite extruded for our study was expected to be different than that of neat PP. Naiki et al.[55] observed micron sized transcrystalline regions when the iPP melt was crystallized under quiescent conditions, on the surface of a talc-rock. At a given crystallization temperature, the thickness of the transcrystals increased with increased cooling time. For instance, when the PP melt was crystallized to 140^{o}C, the thickness of the transcrystalline region increased from 30 μm to 50 μm as the cooling time was increased from 30 min. to 50 min. For the extrusion-molded composite in our case, where the crystallization had occurred at room temperature with a rather short cooling time, the thickness of the transcrystalline regions was expected to be lower. The relative size of the micro-scale crystals (spherulites vs. transcrystals) formed in a given PP-talc composite seems to be affected not only by the cooling rate, but also by the size of the talc used. For example, when Naiki et al.[55] carried out isothermal crystallization of PP melt on a talc-rock, they obtained

transcrystalline regions, which were as thick as the radius of the spherulites nucleated in the bulk. In another study[54] on PP-talc composite filled with talc powder, crystallization of PP under isothermal condition resulted in a large number of relatively smaller spherulite type structures, most of which were on the surface of talc-particles. The reported wide angle X-ray diffraction studies indicated that in the former case, the growth direction of the transcrystals was along the a*-axis of the PP phase. In the latter case, the growth direction of the spherulite type crystal structures was along the b-axis of the PP phase. The growth of crystals along the b-axis of PP phase in PP-talc microcomposites has also been observed by other groups[52-55] under non-isothermal crystallization conditions, which are frequently encountered in common molding processes. For the spherulitic type crystal structures, from now on referred as the radially oriented crystal structures, 300 to 500 nm thick layers of closely packed lamellae were observed[30, 55] near the PP-talc interface. Farther from the interface the lamellae were seen to be loosely packed and randomly oriented. For our study we used a talc powder of flake shaped talc particles with an equivalent spherical diameter of 18 μm. In our case, we expected radially oriented crystal structures with 1 micron thick layers, at the most, of closely packed lamellae. We were interested in understanding the effect of an initially different morphology on the crystal orientation of the matrix phase, during the high temperature solid phase die drawing process.

In a typical die-drawing process, the billet of a given polymeric material is annealed at the draw temperature for an hour or two. The step of annealing of PP at elevated temperature raises its crystallinity[28, 63]; the amount of crystallinity increases with

increasing annealing temperature, as well as the annealing time. Increased levels of crystalline volume fractions are useful for obtaining higher draw ratios[3] in a die drawing operation. The increase in crystalline volume fraction during the annealing step is attributable to the transformation of more and more amorphous domains into crystalline structures. Higher annealing temperatures also result[24-29, 75] in transformation of other crystalline forms namely, β, γ and δ, to the most stable α-form. During these transformations, the polymeric chains get disentangled, and the residual entanglements get pushed into the amorphous phase[76]. Therefore, in addition to the increased crystalline volume fraction, the annealing step may also lead to an increased entanglement density of the interlamellar amorphous phase.

4.1.2 Crystal Orientation during Die Drawing

During a die drawing operation, the annealed material would yield and undergo plastic deformation. Before the material yields, its deformation is governed mainly by the amorphous phase within the stacks of lamellae[34, 68, and 77]. The strained amorphous phase leads to separation, rotation and twisting of lamellae. Once the material has yielded, its deformation is largely governed by the crystal plasticity and the amorphous phase plays a role of stress transfer. In the post-yield deformation[34, 68, 77], the crystalline lamellae undergo coarse slip; the crystals get fragmented and the broken lamellar blocks get oriented in the direction of maximum stress. The extent of crystal disintegration and orientation is determined by the crystal morphology, the degree of entanglement in the inter-lamellar amorphous phase (concentration of tie chains), and the temperature and rate of drawing. For PP, the critical temperature range above which it is

easier to initiate plastic deformation of crystals, without breaking the network of interlamellar amorphous chains (that causes voiding or stress whitening), is found to be in the range of 40^{o}C to 70^{o}C[78].

The smectic or mesophase (an intermediate phase which is neither highly ordered nor highly disordered) in the matrix phase gets melted and becomes orientable above 60^{o}C. The amorphous phase orientation during plastic deformation has been shown to progress with crystal orientation[49, 79]. The deformation of PP crystals is expected to occur largely by slip than by twinning and martenstic transformations[77]. Since the slip planes cannot cross the chain axis (which has the strong C-C covalent bond), they are largely of (*hk0*) type. Pole figure measurements using the wide angle X-ray diffraction technique are frequently used to characterize the crystalline chain axis orientation in processed i-PP [44, 46-50]. The monoclinic unit cell of i-PP doesn't have a reflecting plane of symmetry that is perpendicular to the crystalline c-axis (equivalent to the chain axis). As a result, its orientation needs to be characterized indirectly using diffraction measurements of any two sets of planes that contain the c-axis[80]. To this end, in our study we measured the pole figures of α(110) and α(040). Figure 4.1 shows schematics of both an actual (monoclinic) and modified (orthorhombic) unit cell of α-iPP. As shown in this figure, the α-040 crystal plane has its plane normal parallel to the crystalline b-axis whereas the α-110 crystal plane has its plane normal parallel to bisector of crystalline a* and b-axes.

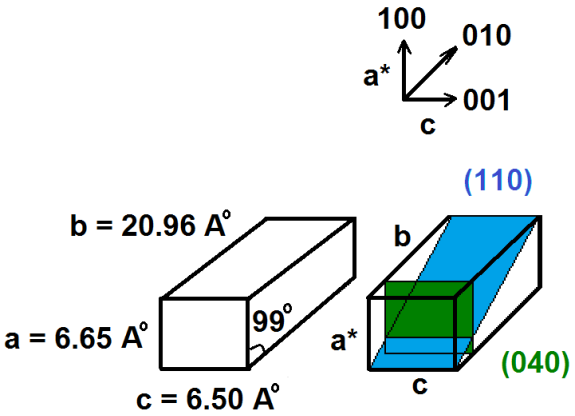

Figure 4.1: Schematics of real and modified unit cell of i-PP.

There are few papers available on crystal orientation of PP phase in molded PP-talc composites[51-54]; however, to our knowledge no study has been reported on crystal orientation of the matrix phase in die drawn PP composites. The literature[46] on texture development in die drawn neat PP is also limited, and that too is confined to the samples collected away from the die, where the deformation of the drawn materials is almost entirely complete. In this chapter, besides studying the crystal orientation of PP in the saturated deformation zone (farther from the die exit), we studied its progress within the die deformation zone, as well as the developing post-die deformation zone close to the die exit. The crystal orientation of the matrix phase was studied for both die drawn neat PP and die drawn PP-talc composite. Besides an initially different crystal morphology introduced by the particles, the orientation of the matrix phase during composite drawing was affected by other micromechanisms or phenomena, such as particle debonding and voids growth. We also analyzed the development of this void growth in various deformation zones. The modulus attained for the final expanded and oriented composite in comparison with the oriented neat PP is discussed in the last section.

4.2 Experimental

4.2.1 Materials

The materials used for the study on crystal orientation involved the polymeric matrix of isotactic polypropylene (i-PP) homopolymer (Dow grade 5D37) with a density of 0.905 g/cc and a melting temperature of 166 (±2)^{o}C. The M_w of the polymer was 249400. It had a polydispersity index of 4.7 and a melt flow rate of 2.8 g/ 10 min. The filler used Luzenac FDC talc with controlled particle size distribution. The median equivalent spherical diameter of talc particles was 18 microns. The particle size distribution for this talc is shown in Figure 2.1. The sp. Gravity of the talc was 2.8 and it had a surface area of 1-2 m^2/g.

4.2.2 Procedures

4.2.2.1 Die Drawing Runs

For this part of the work, die drawing runs made only on the pilot-scale die drawing setup are considered. The issue with the samples from the lab-scale setup is discussed in Appendix B. Billets of neat PP and PP composite filled with 20 wt. % talc were drawn using a wedge die of nominal draw ratio 2, at a draw temperature of 145^{o}C, using four different draw rates of industrial importance (91 cm/min, 244 cm/min, 366 cm/min and 573 cm/min). The wedge die used was 2.6 cm long and didn't have any die-land. The extruded billet was annealed at the draw temperature for one and half hours; it was then pulled slowly by grabbing its pre-shaped tail at a very slow speed. Once the stable drawing of the billet was ensured, it was then drawn with the lowest draw rate of 91 cm/min. On drawing sufficiently long sections at a given draw rate, the drawing rate was

increased to the next level and the intermediate billet sections were discarded. For each draw rate, the drawn billet coming outside of the die was cooled with a water spray tank maintained at 23^{o}C. Additional details are given in section 2.2.2.2. On drawing sufficiently long billets at the highest draw rate of 573 cm/min, the belt puller and the oven were switched off and the strained billet in the die-drawing line was cooled to room temperature under stress. The entire cooled billet for each of neat PP and PP-talc-20 wt. % composite was unloaded from the oven side.

4.2.2.2 Characterization

The undrawn and final drawn billet sections (farther from the die exit) were analyzed for density, crystallinity and crystal orientation measurements at different draw rates. In order to study the structural evolution in the material as a function of deformation in different zones, additional measurements were made on the billet sections of neat PP and PP-talc-20 wt. % composite that were collected after the die drawing run was over. Since the billets were annealed before die drawing operation, all the specimens collected including that of undrawn billet, were annealed for about one and half hour.

4.2.2.2.1 Density Measurements

Densities of the samples before and after die drawing were measured using the Sartorius density determination kit -YDK-01 as described in section 2.2.3.

4.2.2.2.2 X-ray Diffraction

Crystal orientations in drawn and undrawn billets of neat PP and PP-talc composite were characterized using a theta-2theta Scintac XDS-2000 wide angle X-ray diffractometer in reflection mode. The computer-controlled diffractometer consisted of pole figure device

associated with a wide-angle goniometer coupled to sealed-anode X-ray tube. The X-ray tube was operated with an accelerating voltage of either 35 or 40 kV and a corresponding amperage of 35 or 40 mA to generate nickel filtered monochromatic beam of CuK_{α} radiation ($\lambda = 1.542\ A^{o}$). Higher accelerating voltage and amperage was applied for the composite samples because the crystalline talc present in the material absorbs most of the X-rays. The incident beam was collimated by a 1 mm diameter collimator. Only the solar slits were used on the detector side. For billet samples collected before and after die drawing runs, circular specimens of 14 mm diameter were machined from the 20 x 16.5 x 5 cuboidal specimens. Here, 16.5 mm and 5 mm are the final dimensions of the neat PP drawn at the highest draw rate along the TD and ND respectively. The samples were exposed to X-rays by placing the thickness parallel to the incident beam; a schematic of the experimental setup for a circular specimen is shown in Figure 2.6. The distance between the sample holder and the detector was fixed at 270 mm. For a given sample, the goniometer was initially used to get a one dimensional 2 theta (θ) scan over detector angle, and later on to measure pole figures by rotating and tilting the specimen. The 2-theta XRD patterns and the experimental pole figures were obtained with the help of the DMSNT software (version 1.37).

After an initial linear diffraction (2θ) scan, azimuthal scans were run with the detector positioned at a 2θ angle of either $\alpha(110)$ crystal plane or $\alpha(040)$ crystal plane reflection of the iPP matrix. Pole figures were obtained by varying the azimuthal angle (φ) from 0^{o} to 355^{o}, and tilt angle (χ) from 0^{o} to 85^{o} with an angle step of 5^{o} in either sweep. The experimental pole figures acquired by the azimuthal scans were processed and corrected

for defocusing and background intensities using BEARTEX 2008 software (version 3.3). The software incorporates WIMV algorithm[27], which was used to calculate orientation distribution of the intensities for pole figures with incomplete range of tilt angles. The pole figure intensities were plotted in the units of multiplication of a probability density for random distribution (m.r.d.: 0.01 is equal to the pole density of random distribution). To understand some of the features of crystal orientation in greater detail, pole figures of individual crystal axes of the matrix phase were obtained using PCAL routine of the BEARTEX software, assuming an orthorhombic symmetry of the PP unit cell. All the pole figures obtained by this software show the MD oriented horizontally. The reference directions and the 15^{o} net of tilt and azimuthal angles used for discussion of the pole figures are shown in Figure 2.7.

4.2.2.2.3 Tensile Tests

Tensile test specimens were cut and machined for undrawn and drawn billets from the pilot-scale setup as per ASTM D638 type-I standard. Following the work by Mourad et al.[28], the length of the tensile bars was kept higher than the standard (Figure 2.8) to avoid fracturing of the specimens in the grip areas.

Tensile tests were carried out on the Universal tensile tester fitted with 20kN load cell and a 50 mm gauge length axial extensometer (Epsilon model-3542-050M-035-ST). All the tests were carried out at room temperature with a cross head speed of 5.08 mm/min. Experimental data in terms of load cell output and extensometer displacement were monitored using data acquisition software Datum 4.0, which installed on a personal

computer. The data captured was then post-processed to obtain nominal stress-strain curves for tensile modulus determination.

4.2.2.2.1 Differential Scanning Calorimetry (DSC)

Thermal properties of drawn and undrawn specimens were measured on a differential scanning calorimeter (DSC) Q10 by *TA* instruments, operated under nitrogen purge of 50 ml/min. The working principle of this analytical instrument is described in section 2.2.7. The DSC curve for 5-10 mg of the sample cut from a given billet specimen was obtained by heating from it from 40^{o}C to 200^{o}C at a heating rate of 5^{o}C/min. Values of heat of fusion were obtained with the help of Universal Analysis 2000 software (version 4.5A) by TA instruments. The percentage crystallinity of a given sample was determined using equation 2.2.

4.3 Results and Discussion

As shown in Figure 1.7, the deformation of given material during its die drawing takes place mainly in two zones: (a) die zone- within the converging die and (b) post-die deformation zone– in the free drawing region outside the die. The post-die deformation zone can be further subdivided into two zones (i) the developing zone and (ii) the final zone where the material ceases to deform. The relative volume of each of the deformation zone is determined by the material and process parameters. The extent of deformation experienced by a given material can be quantified in terms of its actual draw ratio[3-6], which can be calculated using Equation 1.1. During a die-drawing process, the actual draw ratio of a given billet in various deformation zones increases progressively with the distance. At some point in the post-die deformation zone, it gets plateued to a final value

(DR_{final}). Due to free surface drawing of the material in this zone, the DR_{final} is always higher than the nominal draw ratio of the die (DR_N= ratio of the un-drawn billet cross-sectional area to that of the die exit). The difference between DR_{final} and DR_N is determined by the process parameters and material properties. For the die-drawing runs reported here, we used a wedge die of nominal draw of 2. For various draw rates, the values of the final area ratios and the final draw ratios attained for PP and its composite are presented in Figure 4.2 and Figure 4.3, respectively. At each draw rate, both of these ratios were larger for drawn neat PP than for drawn composite. Higher values of area ratios indicate of higher degree of necking. Neat PP did not show any change in its density on die-drawing, and with the highest draw rate (573 cm/min) the final draw ratio (DR_{final}) attained for it was 8.8 (± 0.05). For the same draw rate, the DR_{final} attained for drawn PP-talc-20 wt. % composite was 8.1 (± 0.05). Debonding of the talc particles and subsequent void growth had led to around 17% reduction in the density of the composite at this DR_{final}.

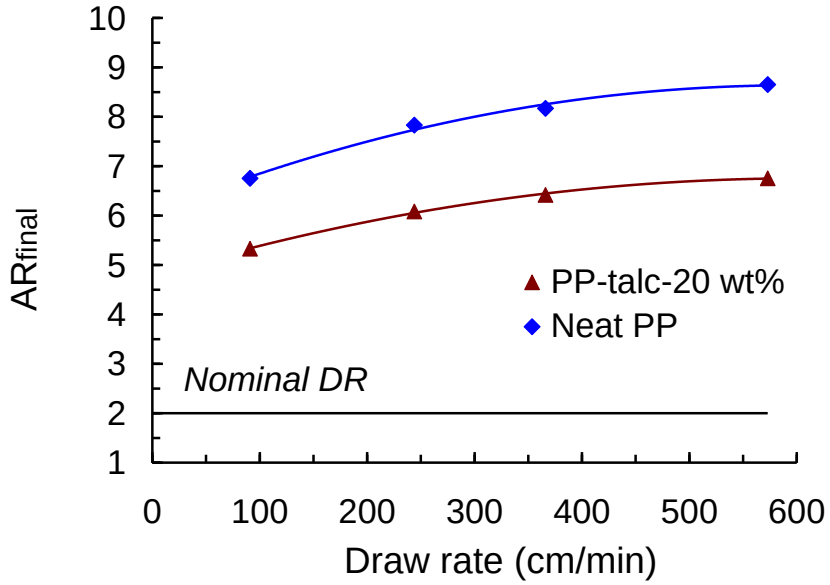

Figure 4.2: Final area ratio of the die drawn neat PP and PP-talc-20 wt. % composite vs. draw rate.

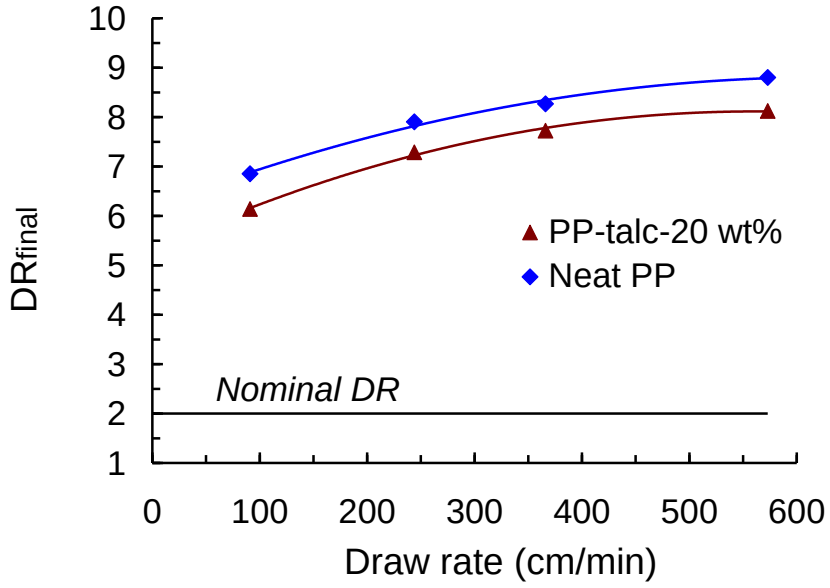

Figure 4.3: Actual draw ratio of die drawn neat PP and PP-talc-20 wt. % composite vs. draw rate.

To understand the progress of void growth and crystal orientation, billet sections of PP-talc composite and neat PP collected from the die deformation zone and the developing portion of the post-die deformation zone were analyzed. Photographs of these billet sections are shown in Figure 4.4; die entry and exit lines for each billet, as well as the reference directions are also shown in the figure. Depending on the die geometry and other process parameters, the billet in the die-zone may leave the die wall before the die exit[39-41]. In our study, the billets of both neat PP and its composite were observed to be in touch with the die-wall, all the way to the die exit.

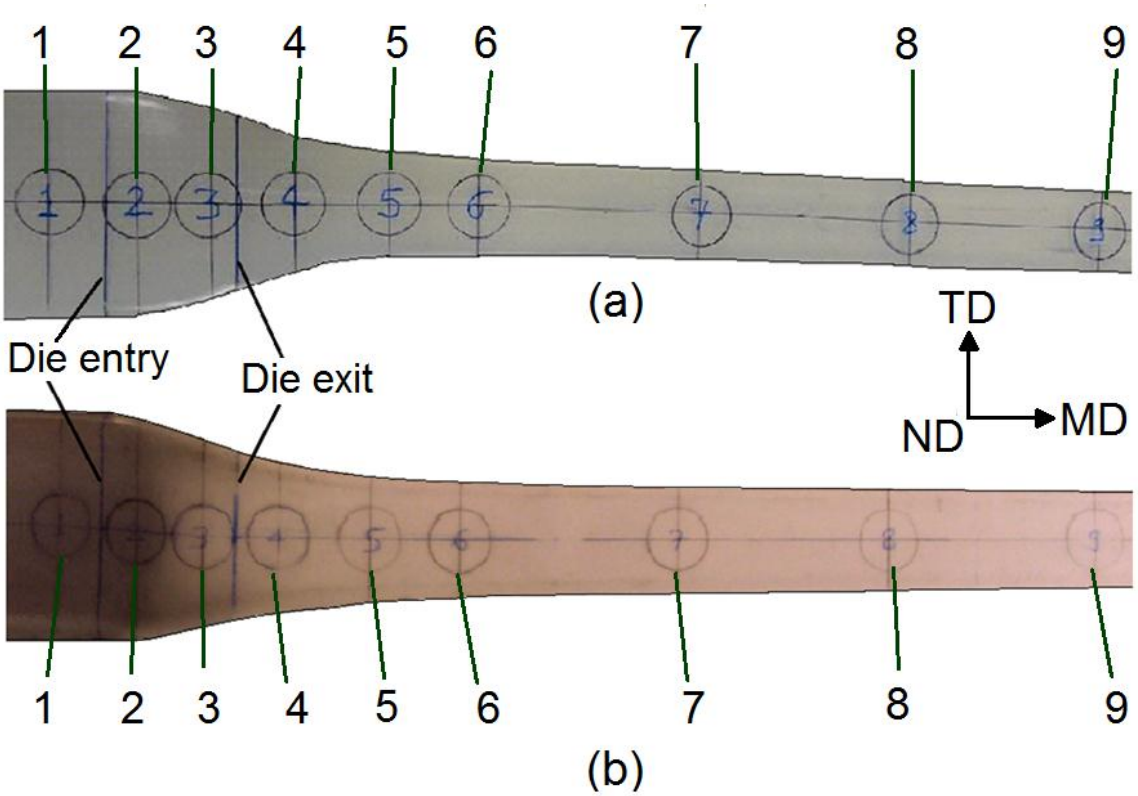

Figure 4.4: Billet sections of (a) neat PP and (b) PP-talc-composite collected after die-drawing runs at 573 cm/min.

4.3.1 Rates of Density reduction and Draw Ratios

Through visual inspection of the billet sections, it was noticed that the billet of neat PP, which was opaque before entering the die, turned transparent at the die exit; the transparency of the billet increased farther from the die exit. The composite billet showed a color change at the die entry; which must be due to the debonding of the talc particles in this region as established by the density measurements. Density measurements of the two billets at different locations are presented in Figure 4.5. Vertical lines in the figure show die entry and exit points.

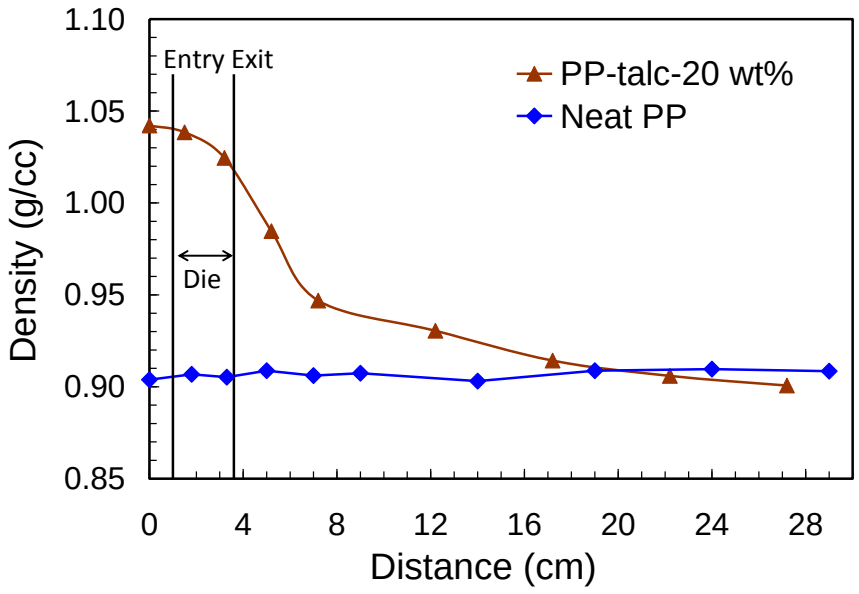

Figure 4.5: Density variations in different deformation zones.

Within the error of experimental measurements, the density of drawn neat PP remained unchanged. On the other hand, the composite density was reduced in three zones: (i) within the die zone, where it reduced gradually (ii) in the developing post-die deformation zone close to the die exit, where a maximum density reduction occurred and (iii) in the final post-die deformation zone- farther from the die exit, where it again

reduced slowly before leveling to a value of 0.87 g/cc. Neat PP billet showed a shaper reduction in cross-sectional area than billet of PP-talc composite. The cross sectional dimensions of each billet were measured at the center lines of the circles marked at different locations (Figure 4.4). These circular discs with 14 mm diameter in the MD-TD plane and 5.0 mm thickness in the ND, were then cut and characterized using density and XRD measurements. The actual draw ratio (Equation 1.1) for a given disc was calculated using the measured values of density and cross sectional dimensions at the disc location.

The relative velocity profiles for the two billets at different DRs were established based on the assumption that they reached the applied draw rate of 573 cm/min at their final draw ratios (DR_{final}). A rough estimate of the flow time for each disc was then calculated using its distance from the first specimen. The trends in the actual draw ratio with flow time for the two materials are presented in Figure 4.6. From this graph, it can be seen that higher values of actual draw ratios were obtained for neat PP. For each of the drawn material, maximum in the draw ratio rate was reached in the post-die deformation zone just outside the die; this rate was relatively higher for the drawn billet of neat PP.

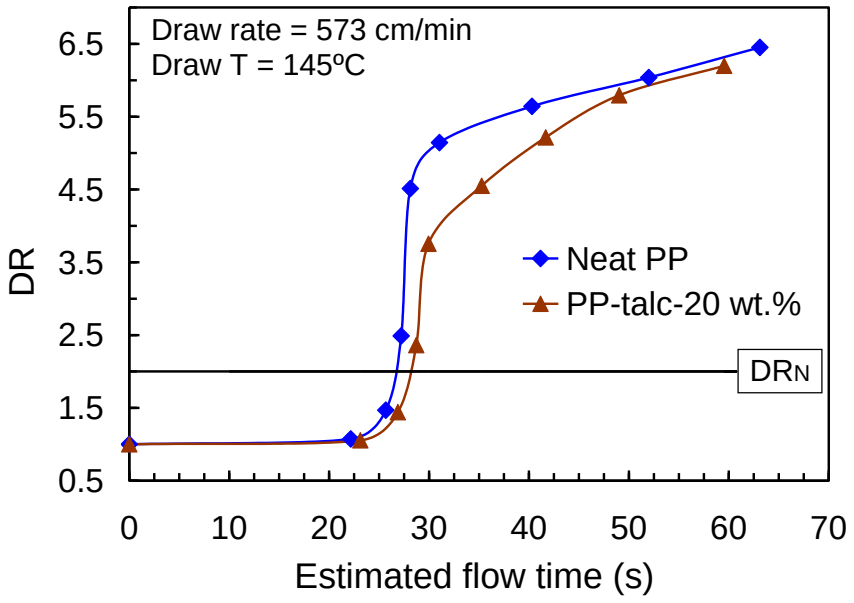

Figure 4.6: Rate of change of DR in the die and developing post-die deformation zones.

4.3.2 Crystallinity and XRD Patterns

The linear 2θ XRD patterns for the two undrawn materials are presented in Figure 4.7.

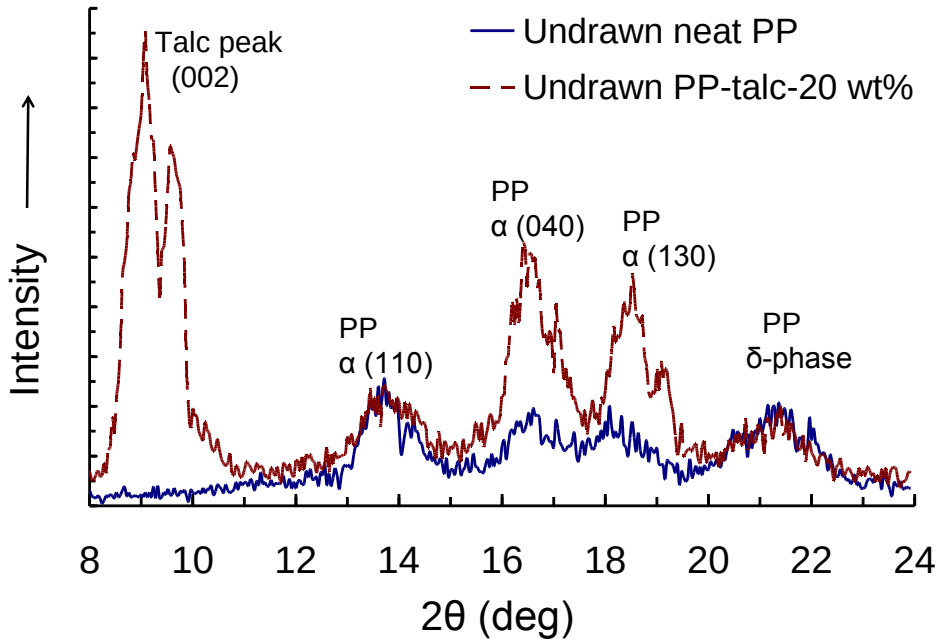

Figure 4.7: Linear XRD patterns of un-drawn neat PP and un-drawn PP-talc composite.

Crystalline reflection peaks occurring at $2\theta = 13.8^{o}$, 16.7^{o} and 18.5^{o} correspond to the Miller indices of (110), (040), (130) in the monoclinic α- crystal of iPP[46, 51, 81]. The smectic or mesoform of PP crystals can be identified by the appearance of the crystalline peak[44, 81] occurring at $2\theta = 21.2^{o}$. In some studies[29, 51, 82], the appearance of the peak at this position is ascribed to the α(111) plane, and it has been associated with the alpha crystals with a better packing of the polymeric chains. Linear XRD patterns of the two materials indicated crystals of α-form, as well as smectic form before drawing. Additional peaks for crystalline talc appeared on the XRD patterns of the composite samples. The relative intensity of the (130) and (040) crystal planes w.r.t. (110) crystal planes was higher for the composite. In some of the X-ray diffraction investigations on molded PP-talc composites, the ratio of intensity I(040)/I(110) has been associated with the nucleation ability of talc[30,52] on the PP crystallization.

The billets of neat PP, as well as PP-talc-20 wt. % composite were annealed at 145^{o}C for an hour and a half before drawing. Figure 4.8 shows the endotherms of a neat PP pellet and a sample from the neat PP billet that was annealed before drawing. It is clear that annealing of neat PP at 145^{o}C resulted in an increase in the enthalpy of the crystalline melting peak. Calculations with equation 2.2 showed an increase of 7 to 8 % in the crystallinity. The endotherms of undrawn materials also showed a shoulder at around 150^{o}C. The presence of the shoulder at this temperature can be attributed to the presence of thermally less stable crystal structure or smectic phase in the polymer.

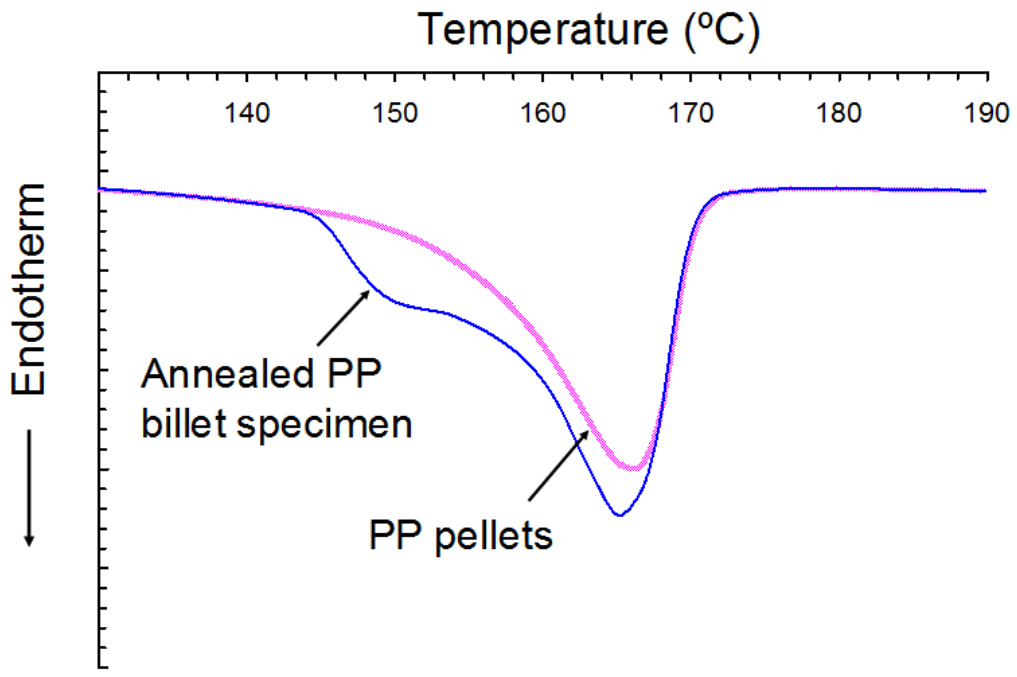

Figure 4.8: DSC endotherms of neat PP before and after annealing.

The DSC endotherms measured for deformed samples of neat PP and PP-talc-20 wt. % composite, collected from locations close to the different specimens shown in Figure 4.4, are presented in Figure 4.9(a)-(b). The actual draw ratio, to which the specimen at a given location was deformed, is also indicated for each curve. The DSC endotherms of the deformed specimens appeared narrower, and their depths increased at higher draw ratios. The endotherms of the final drawn samples were nearly 2 to 2.5 times longer than that of the corresponding undrawn materials.

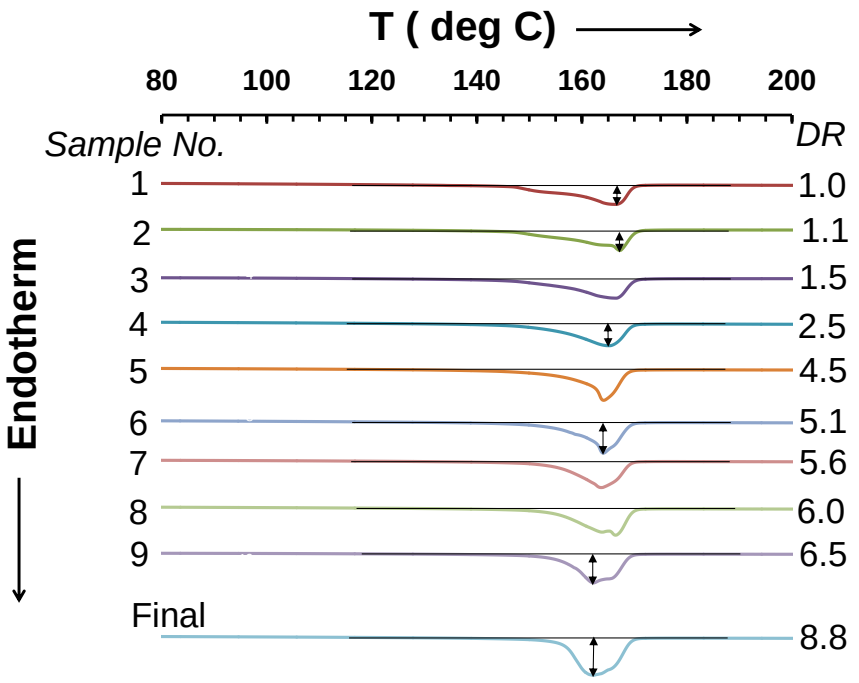

(a)

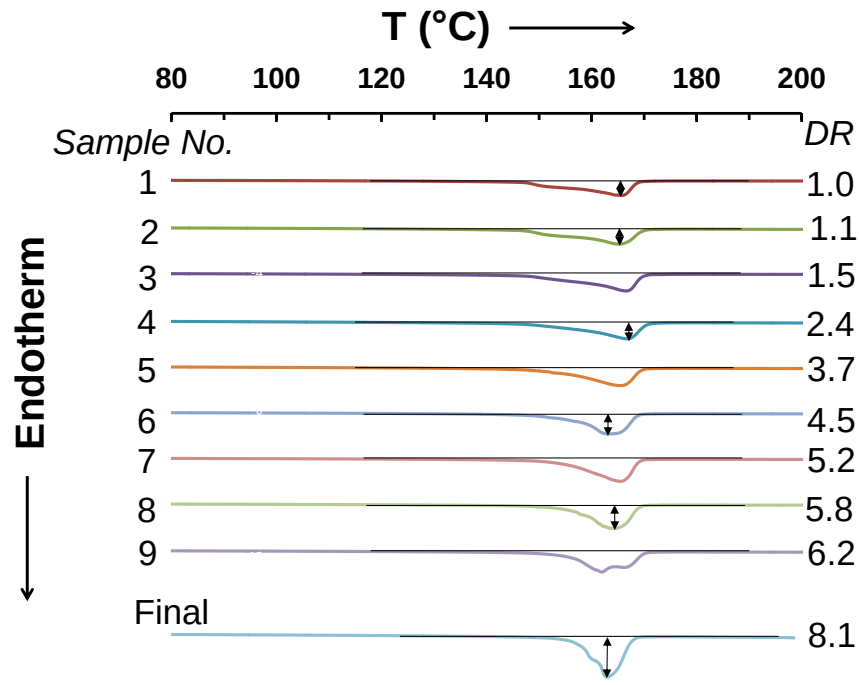

(b)

Figure 4.9: Effect of deformation on DSC endotherms of (a) die drawn neat PP and (b) die drawn PP-talc-20 wt. % composite.

The crystalline volume fractions of the two materials for different draw ratios are given in Table 4.1.

Sample No.	Neat PP	PP-talc-20 wt. %
1	49.8	50.4
2	51.3	47.6
3	49.1	51.5
4	52.7	50.6
5	52.4	50.9
6	52.0	52.1
7	53.2	54.2
8	53.9	56.2
9	54.0	53.7
Final	55.4	57.3

Table 4.1: Percentage crystallinity of neat PP and PP-talc-20 wt. % billets at different locations. The sample numbers in the table correspond to different locations shown in Figure 4.4.

It can be seen that the process of die drawing led to about a 5-7 % increase in the crystallinity of the matrix phase in die drawn billets of both the materials. The endotherms of drawn samples were shifted towards a slightly lower temperature, and they occasionally showed a secondary peak at 160^{o}C. Taraiya et al.[65] have related the appearance of this type of secondary peak to the presence of 'extended chain crystals' in drawn PP. The term 'extended chain crystals' was used to describe crystals formed from unfolded tie chains, these crystals are of different form than the regular α-form with well-folded chains. The XRD patterns of neat PP and PP-talc-20 wt. % composite corresponding to the positions given in Figures 4.9(a)-(b) are presented in Figure 4.10(a)-(b).

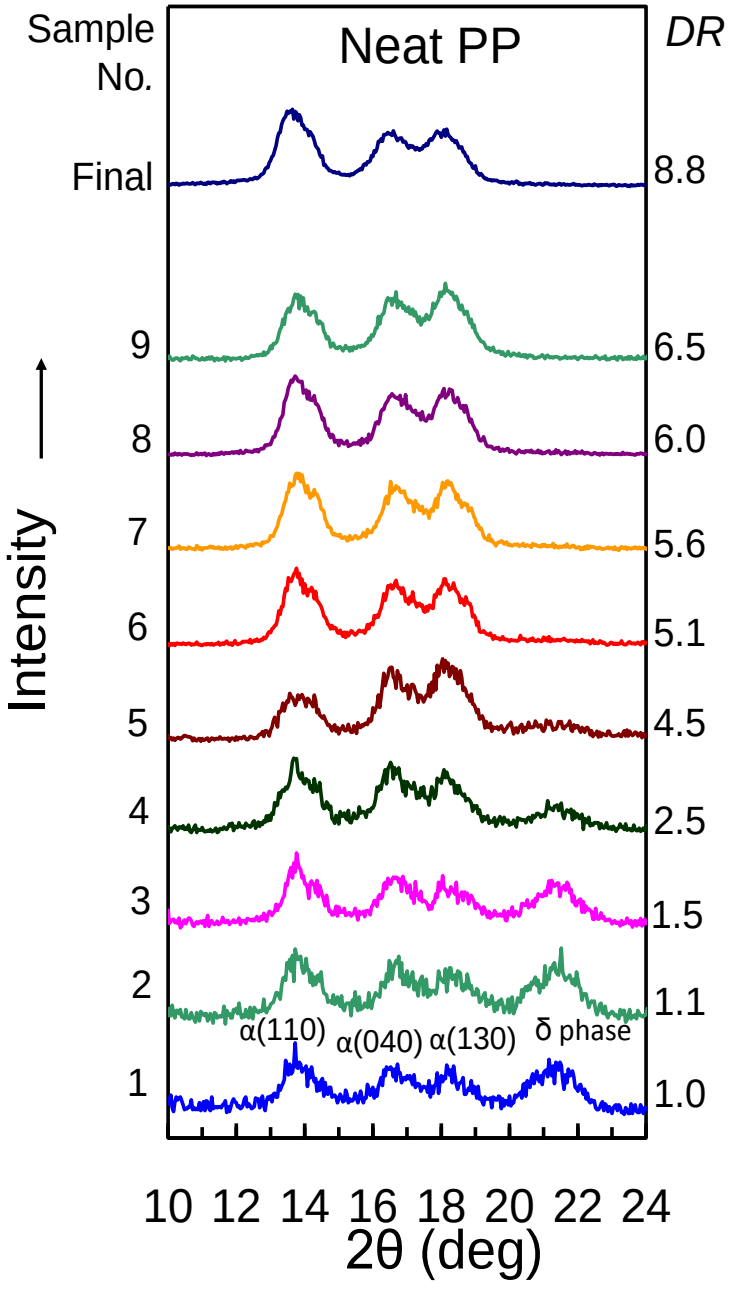

(a)

Figure 4.10: Effect of deformation on the linear XRD patterns of (a) die drawn neat PP and (b) die drawn PP-talc-20 wt. % composite.

Figure 4.10 (cont'd).

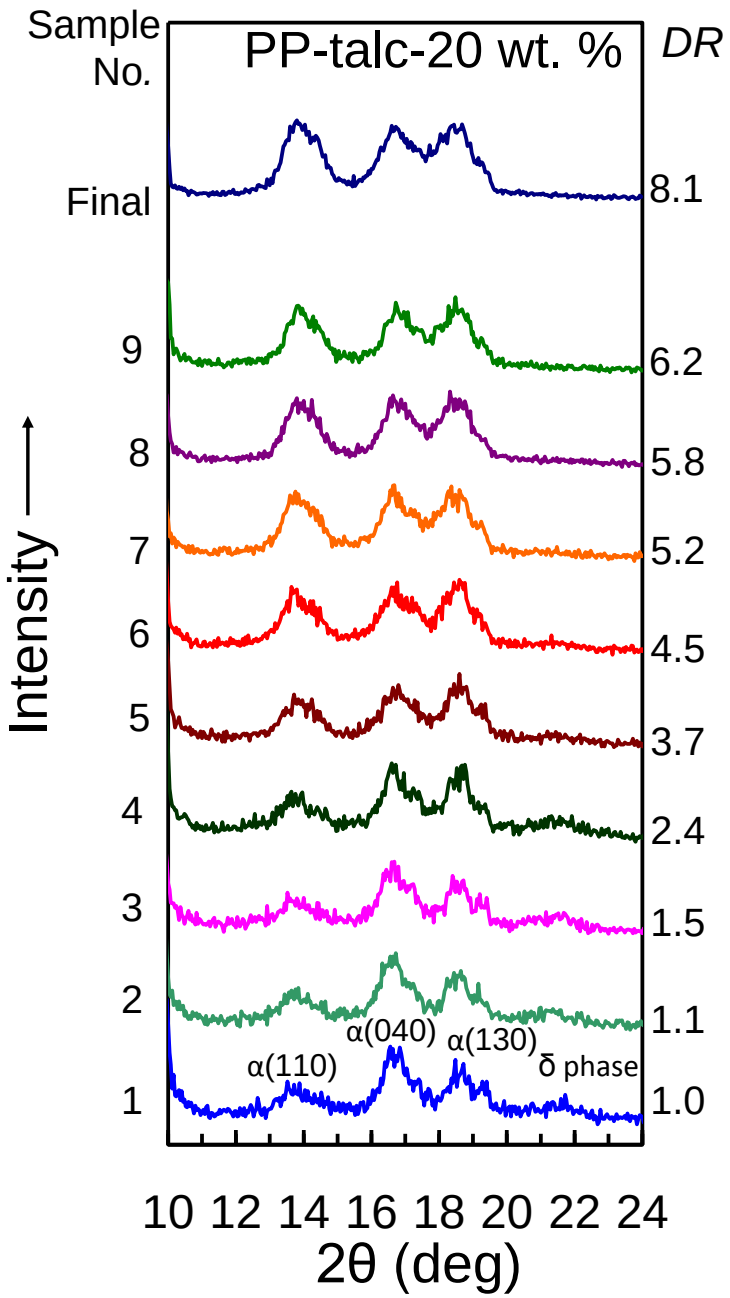

(b)

With an increasing draw ratio, the crystalline peak occurring at 2θ =21.2^{o} started disappearing. Above an actual draw ratio of 4.5, it disappeared completely for both the

drawn materials. The absence of the peak at this position can be noticed on the linear XRD patterns reported for die drawn neat PP by Chaffey and others[46]. Zuo et al.[44] have related the disappearance of the crystal peak at this position to the orientation of iPP crystals. With the help of in-situ wide angle XRD measurements, they concluded that the concentration and mobility of the interlamellar tie chains play key roles in determining the mode of crystal orientation. If the highly entangled tie chains offer significant resistance, then it would lead to crystal fragmentation and formation of oriented mesomorphic phase[84-85], with extended chain conformation. Some groups[86-87] have proposed that stretching of PP restricts the configuration of the polymeric chains, and they cannot form crystals with correct helical hand registration resulting in lamellae with less perfect crystals. The presence of an oriented mesomorphic phase with extended chain crystals can be evidenced by overlapping of the α(110), α(040) and α (130) crystal peaks[82, 88]. The linear XRD patterns of the drawn samples in our study showed some overlap of α(040) and α (130) crystal peaks; the extent of this overlap increased gradually with draw ratio. These patterns however, indicated that for the most part, the orientation of the matrix phase by die drawing had resulted largely in folded-chain crystals. As proposed by Zuo et al.[44], the higher draw temperature in our study would have resulted in a relatively higher mobility of the interlamellar amorphous phase, allowing chain disentanglement during the orientation process. This, not only resulted in formation of well-folded crystals but also in increased volume fraction of the crystals. The texture of these crystals and their orientation levels were characterized with help of pole figure measurements.

4.3.3 Texture Evolution

Optical microscope images of undrawn and die drawn samples of neat PP (drawn at 573 cm/min) are presented in Figure 4.11(a) and Figure 4.11(b), respectively.

The spherulitic morphology in undrawn PP changed to axialite morphology (lamellar stacks oriented along the draw direction) on die-drawing. Optical transmission images for the composite specimens could not be obtained due to the presence of talc particles. The orientation levels in both of the materials were therefore tracked using the X-ray pole figures.

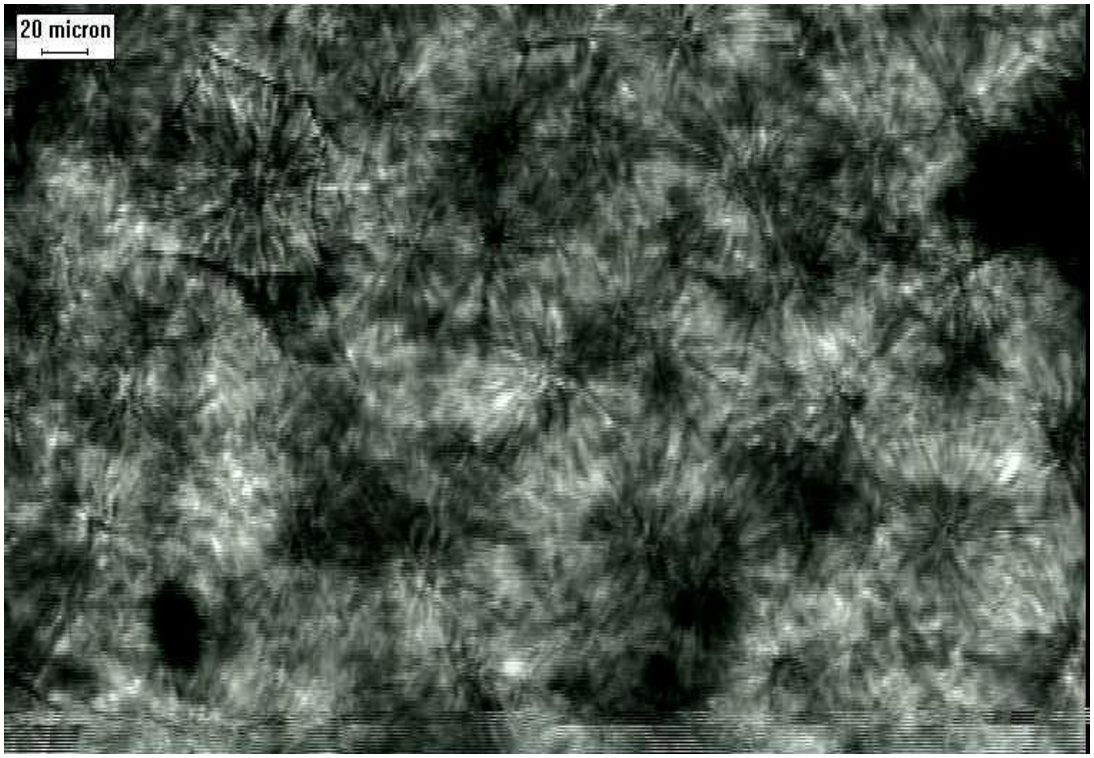

(a)

Figure 4.11: Optical images of neat PP (a) un-drawn and (b) die-drawn at 5.73 m/min (DR_{final}=8.8).

Figure 4.11 (cont'd).

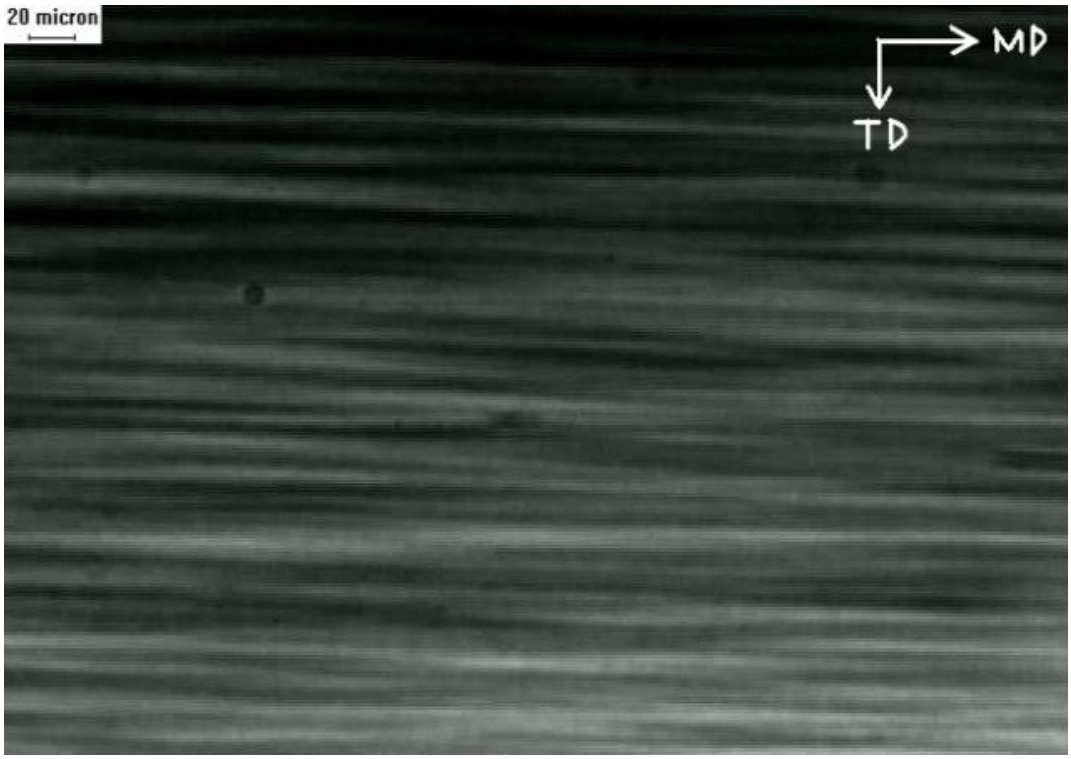

(b)

4.3.3.1 Polymer Crystal Morphology in Undrawn Materials

As explained in section 4.1.2, the monoclinic unit cell of i-PP doesn't have a plane of symmetry that is perpendicular to the crystalline c-axis (equivalent to the chain axis). Therefore, its orientation needs to be characterized indirectly from the diffraction measurements of any two planes containing the c-axis[80]. From the comparison of 2θ XRD patterns of PP-talc composite and the talc powder (Figure B.2 in Appendix B), it was noticed that the crystal peaks of α(040) and α(110) of the PP phase were not interfered with any of the crystal peaks of the base talc. Pole figure of these planes were measured in order to evaluate crystal orientation in the matrix phase. As shown in Figure 4.1, the α-040 crystal plane has its plane normal parallel to the crystalline b-axis, whereas

the α-110 crystal plane has its plane normal parallel to bisector of crystalline a* and b axes. Pole figures of α(110) and α(040) measured for undrawn neat PP and PP-talc composite are presented in Figures 4.12(a) and 4.12(b) respectively.

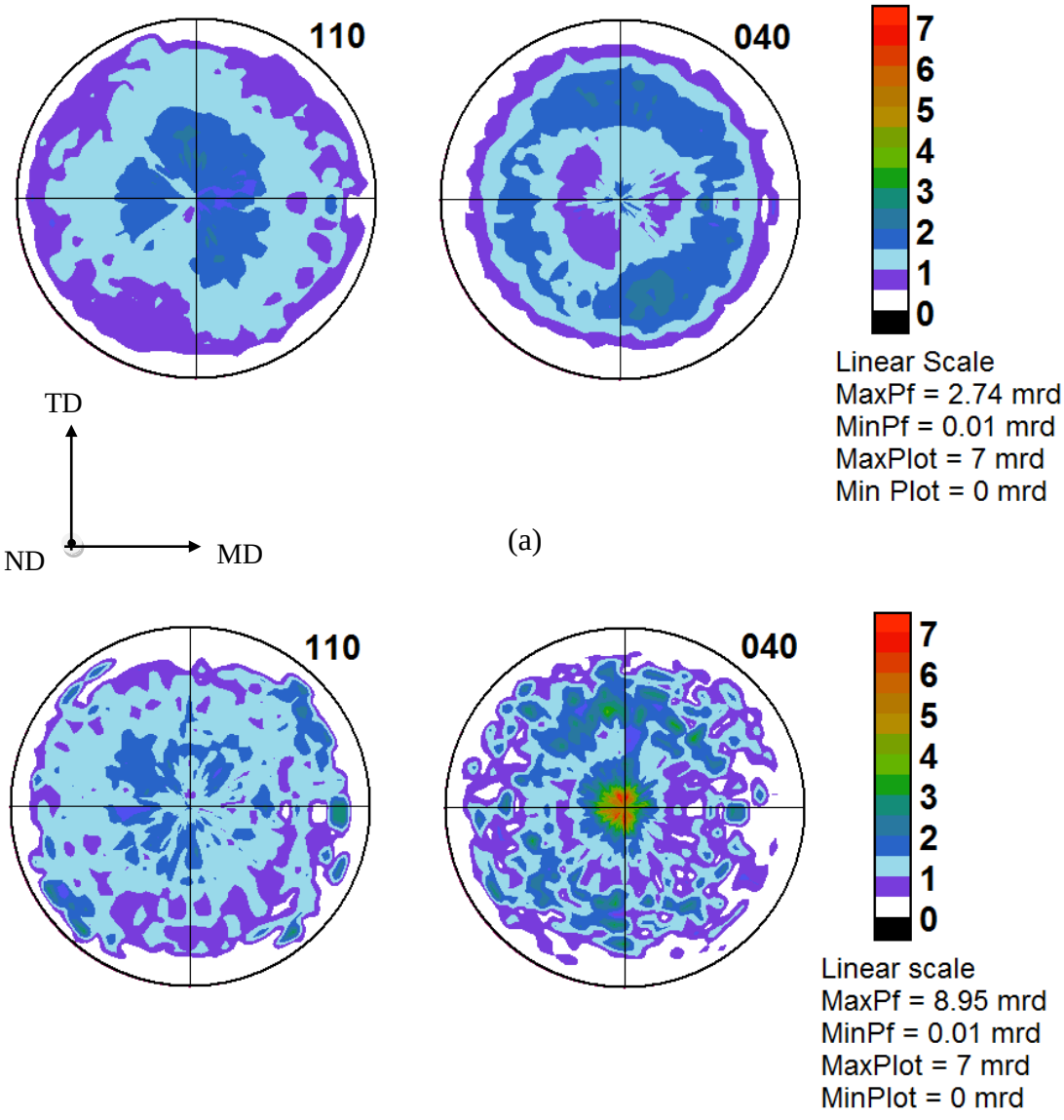

Figure 4.12: Pole figures of α(040) and α(110) crystal planes of iPP in (a) un-drawn neat PP and (b) un-drawn PP-talc-20 wt. % composite

In the case of undrawn neat PP (Figure 4.12(a)), (110) poles showed strong orientation around the ND, extending in the spherical region up to 45^{o} from the ND. The maximum corresponding to this crystal orientation on the (040) pole figure can be seen in the region between 30^{o} to 75^{o} from the ND. The orientation of (110) poles in undrawn composite was nearly similar to that of undrawn neat PP; however, the (040) poles in the composite specimen were strongly oriented along the ND. This peculiar orientation can be attributed to the nucleating effect of the talc particles, which provide additional nucleation sites and trigger piling up of the α(040) planes of PP on their surfaces. Other groups[30, 52-54] have also reported preferred orientation of the PP crystals, perpendicular to the plate planes of the talc particles.

Calculated pole figures of the individual crystal axes of PP, corresponding to the measured pole Figures 4.12(a) and Figure 4.12(b), are presented in Figure 4.13(a) and Figure 4.13(b), respectively. The calculated pole figures are useful in decoupling the information on the measured pole figures of α(110) and α(040) crystal planes. For instance, the crystal orientation which showed higher intensities 45^{o} from the ND on the (110) pole figure, would give maximum intensities in the regions ~15^{o} to 60^{o} from the ND, on (100) or a*-axis pole figure and ~30^{o} to 75^{o} from the ND, on the (010) or b-axis pole figure. Additional details on the orientation state of the crystalline c-axis equivalent to the chain axis of interest could be obtained directly from the (001) pole figure.

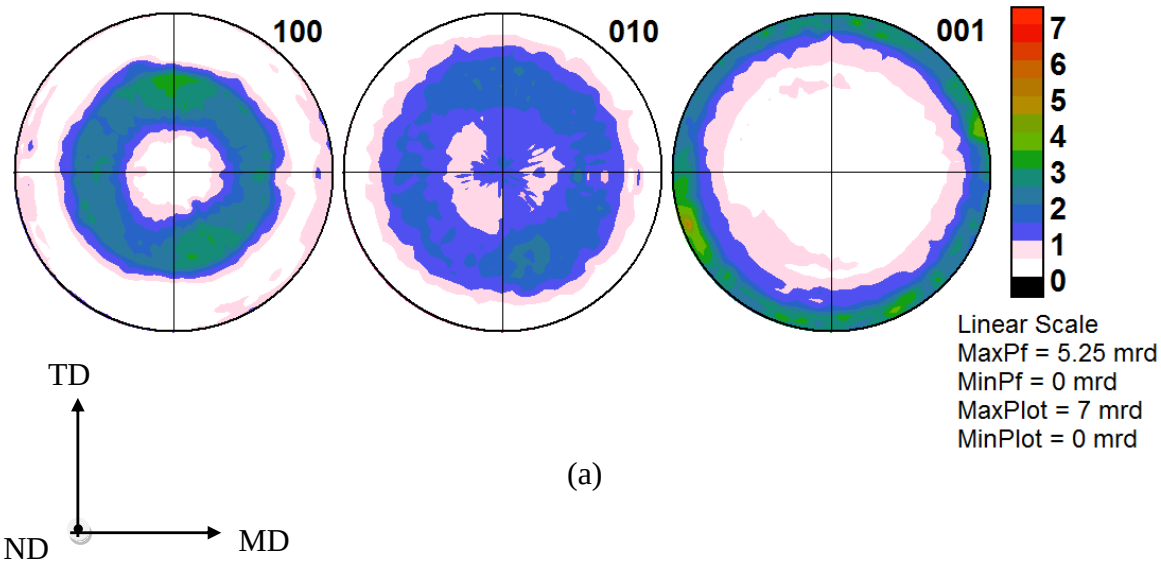

(a)

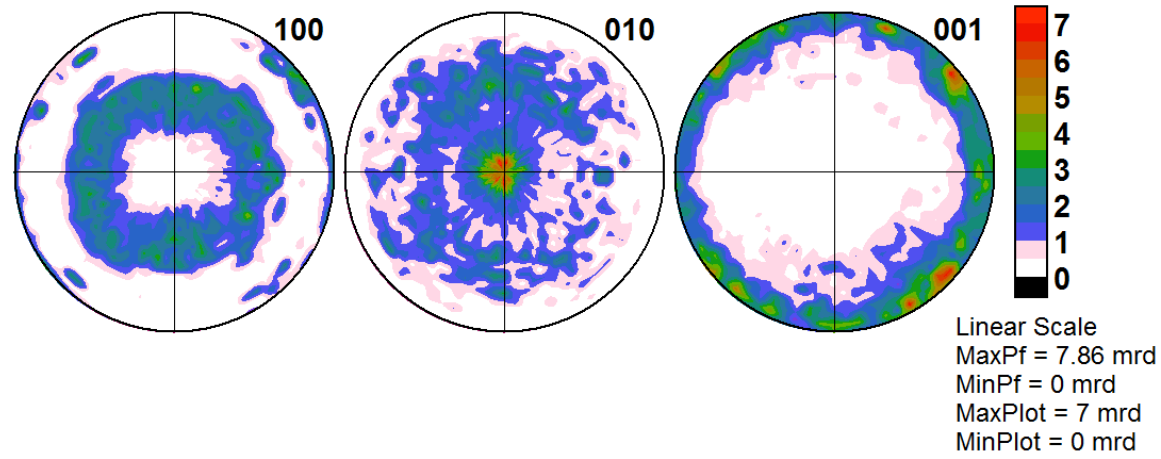

(b)

Figure 4.13: Pole figures of individual crystal axes of iPP in (a) un-drawn neat PP and (b) un-drawn PP-talc-20 wt. % composite.

Before die drawing, the crystalline c-axis in both of the materials was randomly oriented. However, its intensity was concentrated mainly in the flow plane (MD-TD); more so for the composite, than for the neat PP. The intensity distributions of the maxima in the 15^{o} to 60^{o} region from the ND on the a*-axis pole figure, and the 30^{o} to 75^{o} region from the ND on the b-axis pole figure of the undrawn composite were nearly similar to that of

undrawn neat PP. This indicated presence of radially oriented crystal structures in the undrawn composite. For an extruded PP-talc powder composite that was cooled to ambient temperature using a fast cooling rate, the presence of spherulite type domains in the matrix seemed obvious. The intensity of the b-axis along the ND in the composite sample was more than double the intensity of corresponding maximum for neat PP. This suggests that a majority of the spherulitic type domains in the composite were nucleated on the surface of the talc particles. This is in agreement with the observations made by others[30, 55, and 89]. Keeping with these observations, the radially oriented crystal structures formed in the undrawn composite must have been of smaller size than the spherulites formed in the unfilled PP.

4.3.3.2 Texture Development in Die Drawn Materials with Draw Ratio

Under a similar set of processing conditions, higher draw ratios and rate of draw ratio were developed during die drawing of neat PP (Figure 4.6). These differences combined with the above discussed difference in the crystalline morphology of the matrix phase in un-drawn materials were expected to result in different textures on die-drawing. The analyses of linear XRD patterns and DSC endotherms were useful in understanding the transition of the amorphous and smectic phases to a highly oriented crystalline phase on die-drawing. However, these analyses were insufficient to understand any significant differences in the textures of matrix phases between the die-drawn PP-talc composite and the die-drawn neat PP. The differences and similarities in the texture development of the two materials were analyzed with the help of X-ray pole figure measurements.

Pole figures of the individual crystal axes of the matrix phase in die drawn samples of neat PP and PP-talc composite collected at different locations corresponding to Figure 4.4,

are presented in Figure 4.14-Figure 4.18. Figure 4.14(a)-(b) shows pole figures for the two materials at the die entrance.

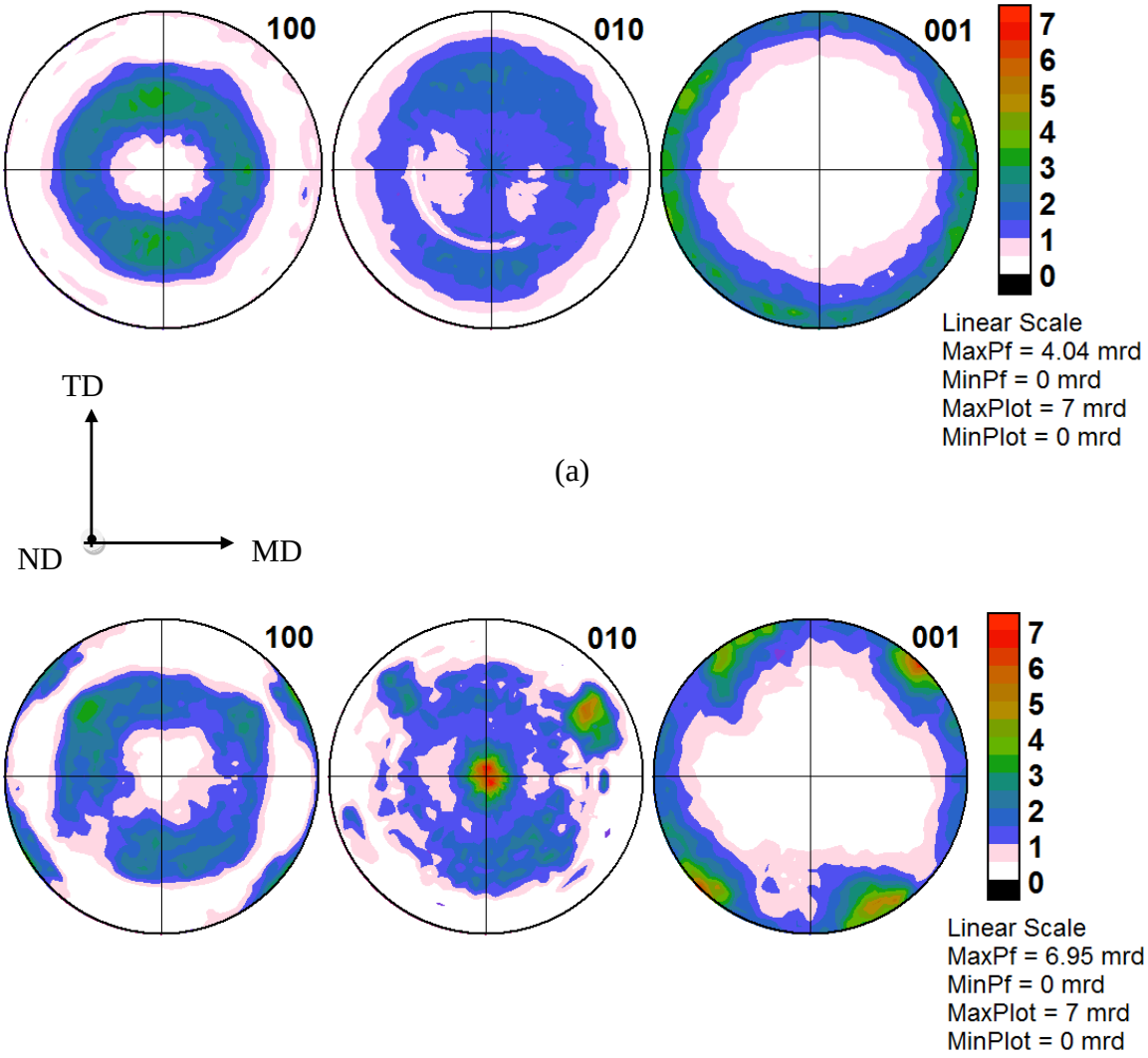

Figure 4.14: Pole figures of individual crystal axes of iPP for (a) neat PP at the die entrance, DR=1.07 and (b) PP-talc-20 wt. % composite at the die entrance, DR=1.06.

Neat PP pole figures at this location (DR=1.07) showed no change from that of the un-drawn PP sample; the a*-axis was oriented 15^{o} to 60^{o} from the ND, the b-axis was oriented 30^{o} to 75^{o} from the ND, and the c-axis was oriented randomly in the MD-TD

plane. As like un-drawn composite, the composite sample at this location (DR=1.06) too showed the b-axis strongly aligned along the ND. However, the c-axis and a*-axis of the composite at this location were oriented 45^{o} between MD and TD. A possible reason for this type of texture could be the orientation of the crystalline domains close to the talc particles. On entering the converging section of the die, the dispersed talc particles in the partly molten matrix might have started to orient with their longer dimension parallel to the MD. Pole figures of the two materials at the die exit are given in Figure 4.15(a)-(b). Neat PP at this location (DR=1.47) showed dramatic changes on its pole figures. The a*-axis was strongly oriented in the ND, whereas the b-axis was oriented in the flow plane particularly along the TD. The c-axis orientation in the flow plane was still random. Such types of sudden changes on the pole figures of neat PP have been reported at its yield point, and are associated with the coarse slip or breaking of the spherulitic domains containing the cross-hatched α-crystals[44, 79]. The pole figures of the composite sample at the die exit (DR=1.44) showed the b-axis still aligned in the ND, but at this point, the a* and c axes were randomly oriented in the flow plane, probably due to increased concentration of the debonded particles.

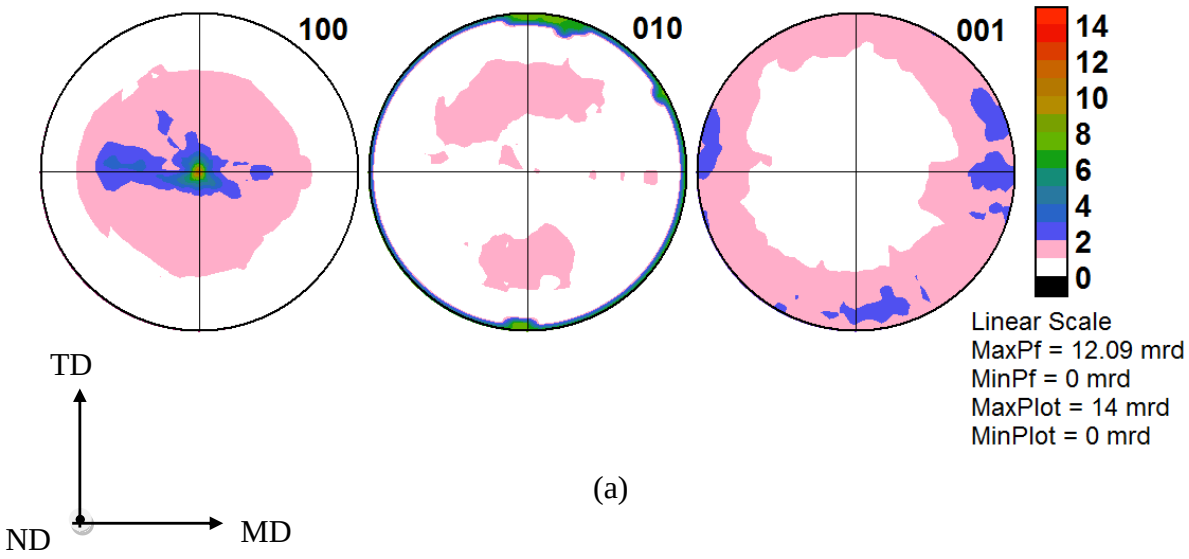

(a)

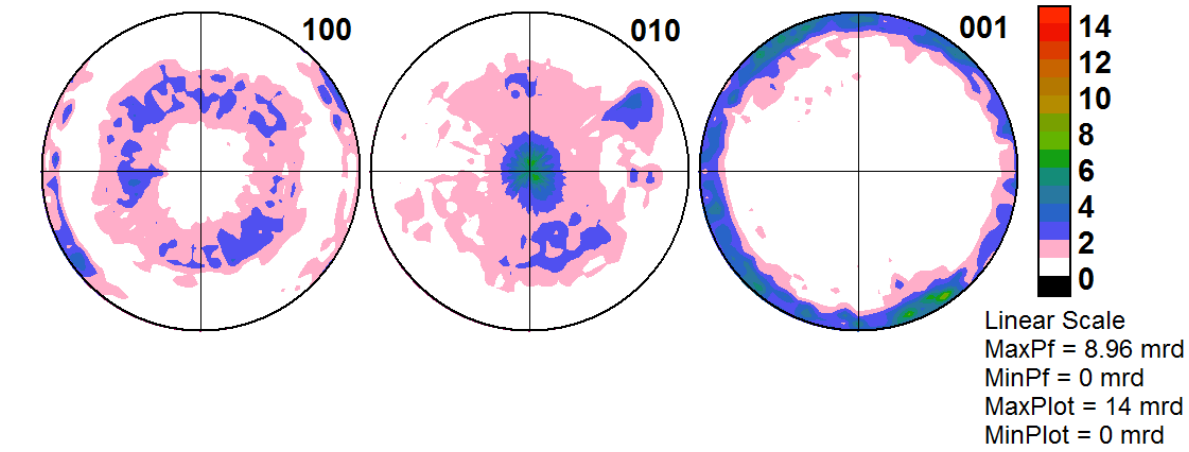

(b)

Figure 4.15: Pole figures of individual crystal axes of iPP for (a) neat PP at the die exit, DR=1.47 and (b) PP-talc-20 wt. % composite at the die exit, DR=1.44.

Pole figures of the samples collected from the free surface drawing region right outside the die (location 4) are presented in Figure 4.16(a)-(b). For drawn neat PP at this location (DR=2.49), a* and b axes were clustered in the ND-TD plane, largely between ND and TD. The crystalline c-axis in drawn neat PP at this location showed a noticeable orientation along the MD. As like neat PP, the drawn composite (DR=2.36) at this location showed clustering of the a* and b axes in the ND-TD plane. But unlike neat PP,

the b-axis poles in the composite were still oriented strongly along the ND and the c-axis exhibited a gradual orientation in the flow (MD-TD) plane.

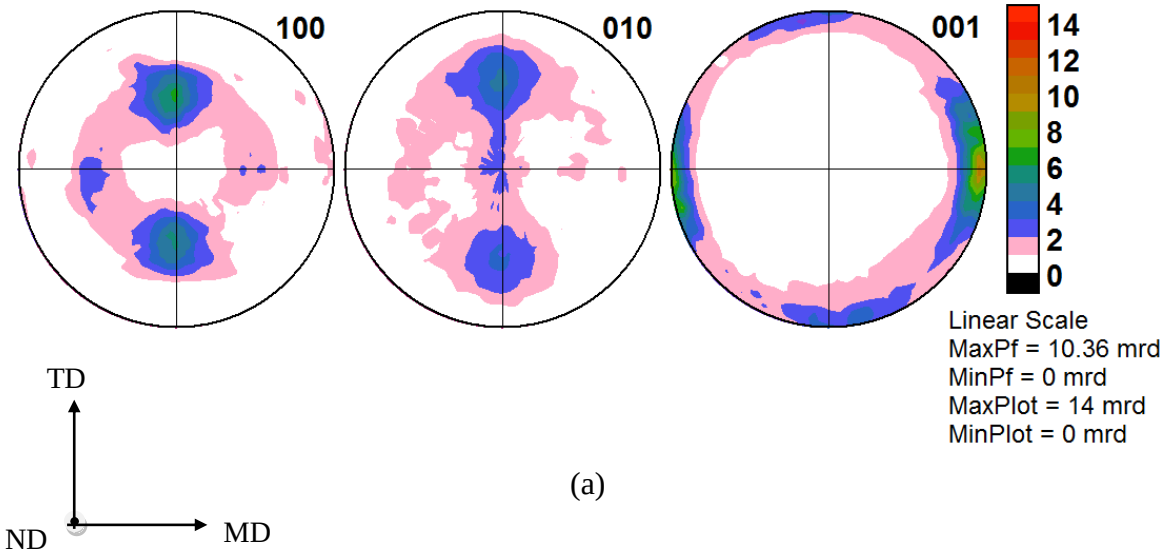

(a)

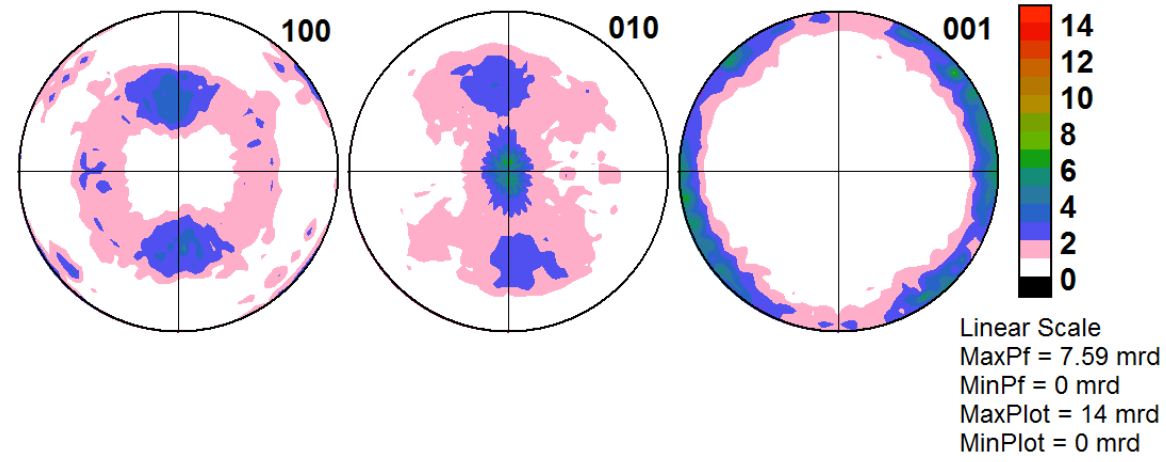

(b)

Figure 4.16: Pole figures of individual crystal axes of iPP for (a) neat PP at location 4, DR= 2.49 and (b) PP-talc-20 wt. % composite at location 4, DR= 2.36.

Figure 4.17(a)-(b) shows pole figures of the two materials collected from location 6, where they were subjected to some additional free surface deformations. Neat PP at this location attained a DR of 5.14, and showed increased orientation of the c-axis along the

MD; the a*-axis was more uniformly oriented midway between ND and TD, while the b-axis orientation was split between the ND, and midway between the TD and the ND. Drawn composite sample collected from this location had reached a DR of 4.55, and it also showed well developed orientation of the c-axis along the MD.

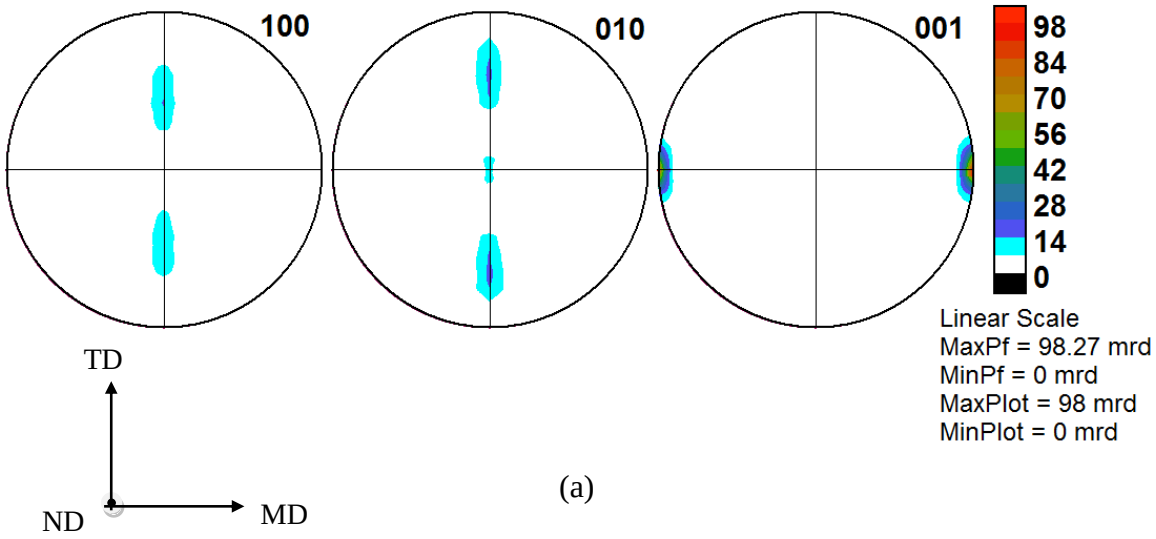

(a)

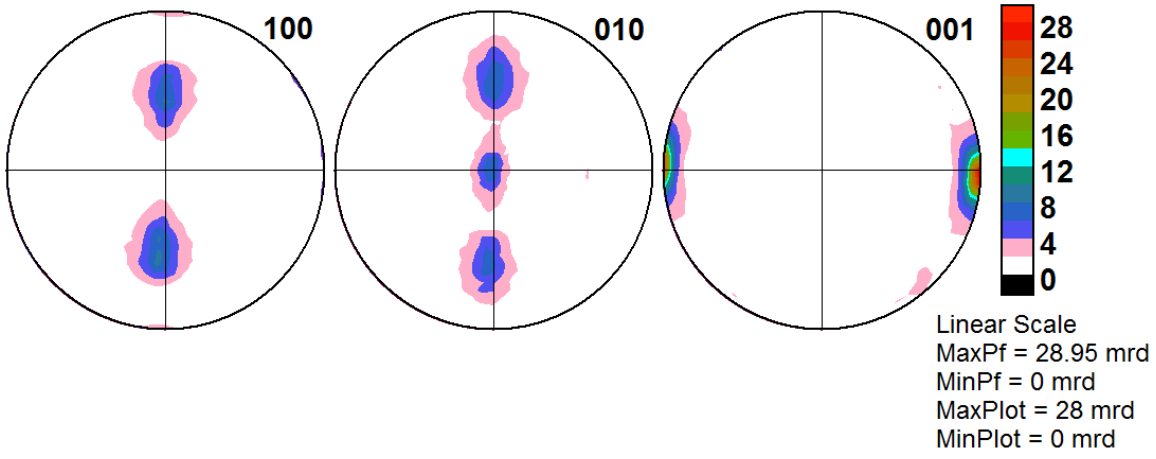

(b)

Figure 4.17: Pole figures of individual crystal axes of iPP for (a) neat PP at location 6, DR=5.14 and (b) PP-talc-20 wt. % composite at location 6, DR=4.55.

The orientation of a* and b axes in the drawn composite was nearly similar to the corresponding neat PP sample, but with a wider spreads of the intensities. With an increased draw ratio in the post-die deformation zone, the orientation of all crystal axes became similar between neat PP and PP-talc composite, as displayed in Figure 4.18(a)-(b).

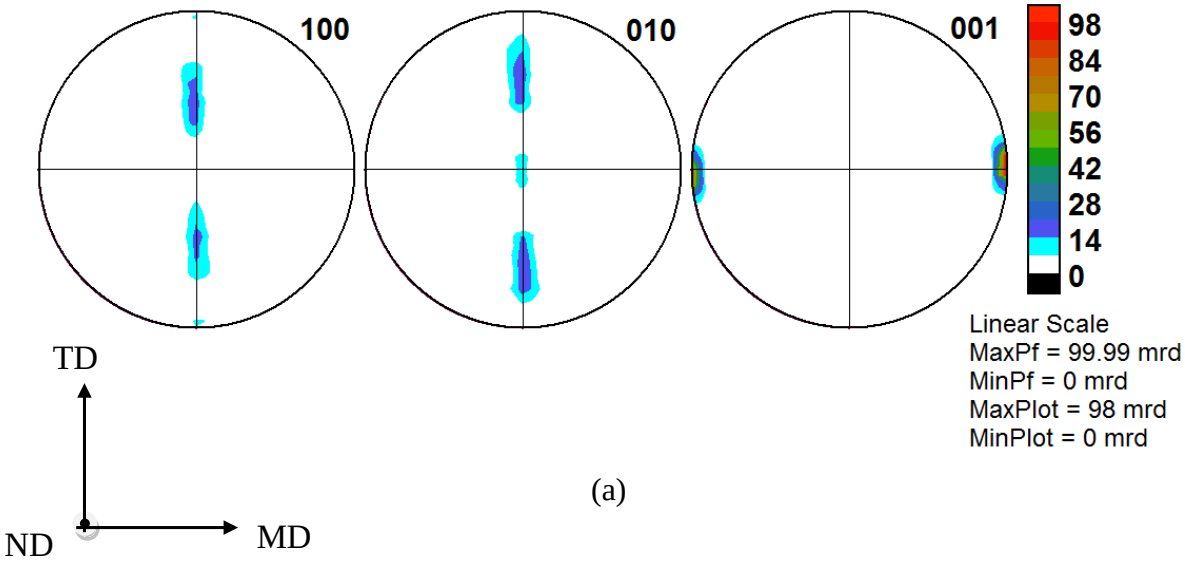

(a)

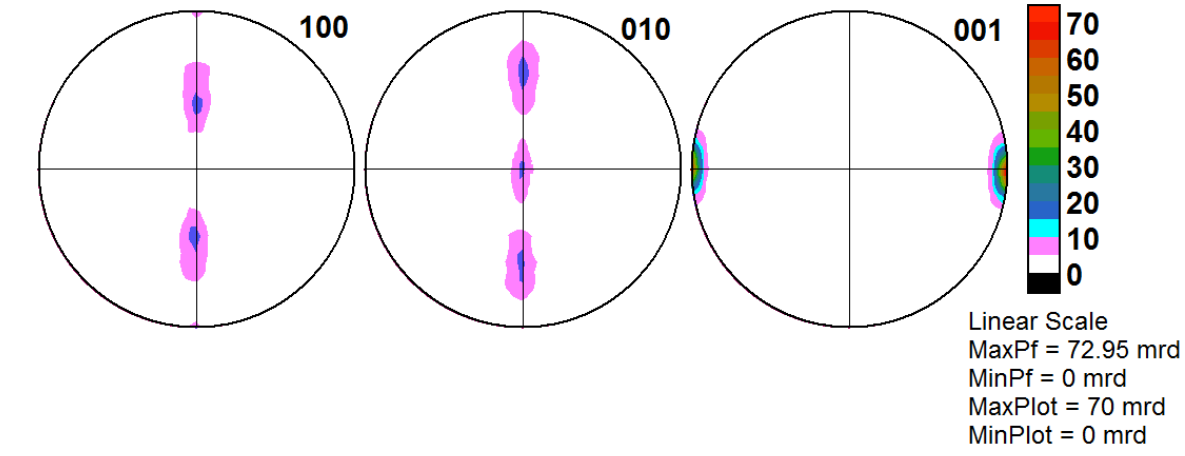

(b)

Figure 4.18: Pole figures of individual crystal axes of iPP for (a) neat PP at location 8, DR=6.04 and (b) PP-talc-20 wt. % composite at location 8, DR=5.79.

To see the effect of DR on the crystal orientation, we quantified the crystalline c-axis orientation in terms of its Herman orientation parameter. In pervious studies by other groups[46, 49-50, 92-93], the c-axis orientation in processed isotactic PP has been quantified indirectly, with the help of orientation distributions on the measured pole figures of (110) and (040). In our work, we were able to calculate the c-axis orientation directly from the intensity values of (001) pole figures using Equation 4.3:

$$\left\langle \cos^2 \phi_{cM} \right\rangle = \frac{\int_0^{2\pi} \int_0^{\pi/2} I(\varphi,\chi) \cos^2 \varphi \sin^3 \chi \, d\phi \, d\chi}{\int_0^{2\pi} \int_0^{\pi/2} I(\varphi,\chi) \sin \chi \, d\phi \, d\chi} \tag{4.3}$$

Herman orientation parameters for the c-axis orientation in MD were then computed using Equation 4.4:

$$f_{cM} = \frac{3\left\langle \cos^2 \varphi_{c,M} \right\rangle - 1}{2} \tag{4.4}$$

The range of values for f_{cM} is between -0.5 and 1. When it is -0.5, the c-axes are all aligned perpendicular to the draw direction. When f_{cM} is 0, the orientation is random; when f_{cM}=1, the chain axes are all aligned with the draw direction.

The calculated values of Herman orientation parameters for the crystalline c-axis, with respect to the MD vs. DR, are plotted in Figure 4.19.

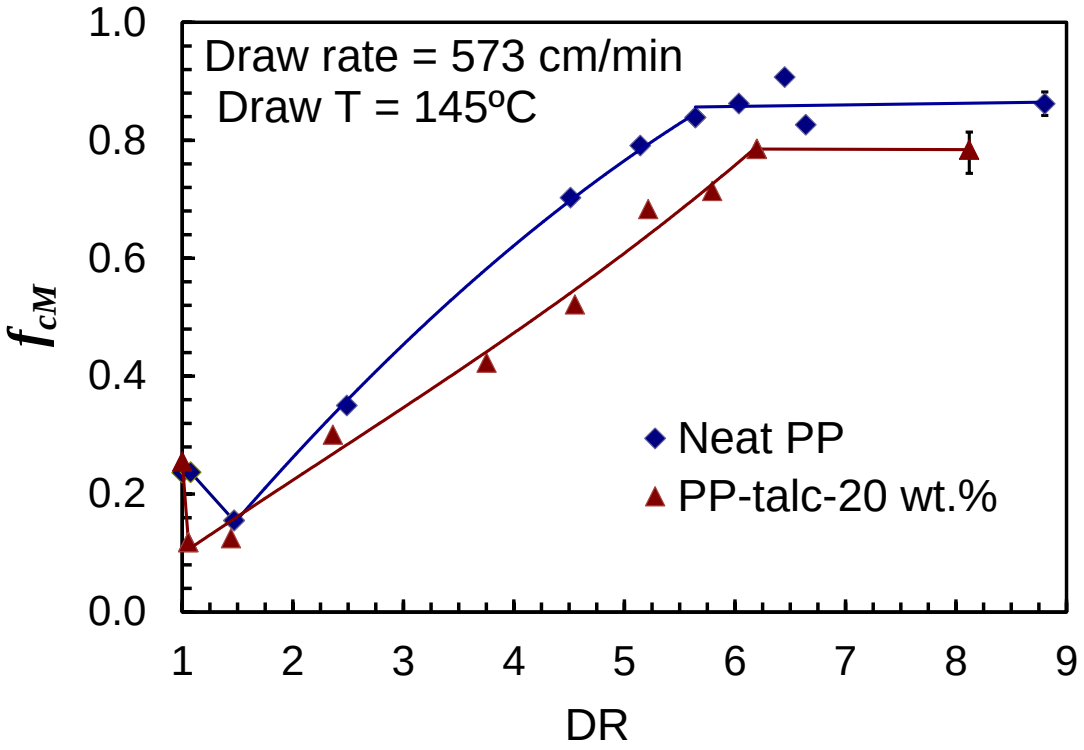

Figure 4.19: Evolution of the Herman orientation parameter of the crystalline c-axis of PP phase.

Before subjecting them to die drawing, the c-axis orientation parameters in the two materials (1st point on each curve) were nearly similar. Initial deformation of both neat PP and PP-talc-20 wt. % composite led to a decrease in the c-axis orientation. Huy and coworkers[79] have associated the randomization of c-axis orientation to an increased level of local strains, which ultimately cause the matrix to yield. It is clear from this plot that the composite yielded at a lower DR ($\leq$ 1.1) attained at or before the die entrance (2nd data point on the composite graph), whereas neat PP yielded at a higher DR of ~1.5, attained close to the die exit (3rd data point on the neat PP graph). For both the drawn materials, the crystalline c-axis of the matrix phase started to get oriented strongly along the MD, right outside the die-exit. From Figure 4.16, it can be seen that this transition

occurred for both the materials at their inflection points on the plot of DR vs. flow time. Despite an earlier onset of the plastic deformation region, the post-yield crystal orientation of the matrix phase in drawn composite was more gradual than that of drawn neat PP. In the final, saturated portion of the post-die deformation zone, drawn samples of both the materials showed saturation in c-axis orientation, as indicated by the last point on each graph. The error bar on this point was established by characterizing 3 different samples of drawn materials collected farther from the die exit. The c-axis orientation parameter in drawn neat PP leveled above a DR of 5.14. The leveling of c-axis orientation in die-drawn composite started at a higher DR of 6.2.

The process of die-drawing led to increased orientation of the crystalline c-axis of the matrix phase in both neat PP and PP-talc composite. The intensity profiles on the pole figures indicate that the development of (hk0)[001] type texture elements in drawn samples are largely responsible for this type of crystal orientation. A (hk0)[001] type texture shows that the majority of the crystals are oriented with their (hk0) poles perpendicular to the surface and the c-axis oriented along the drawing direction[10]. During their plastic deformation, crystals of PP undergo coarse slips; because they cannot cross the chain axis with the strong C-C covalent bond, the slip planes are of (*hk0*) type[47-58, 77, and 91]. The chain slip is the easiest system to be activated. The texture analyses of neat i-PP, deformed by various processes like free tensile drawing[44], plane-strain compression[48], unidirectional film drawing[49, 53], sequential[47] and simultaneous bidirectional film drawing[47, 92] have shown development of (hk0)[001] type texture

elements. The calculated pole figures of the individual crystal axes, corresponding to the ideal orientations of commonly found (110)[001] and (010)[001] type textures are shown in Figures 4.20 (a) and (b), respectively. Comparing these ideal textures with the pole figures in our study, particularly from the free surface drawing zone, indicated development of (110)[001] and (010)[001] type texture elements in the matrix phase. The pole figures show an approximate spread of 45^{o} in the ND-TD plane, most likely due to the non-ideal polymorphic nature of the crystals.

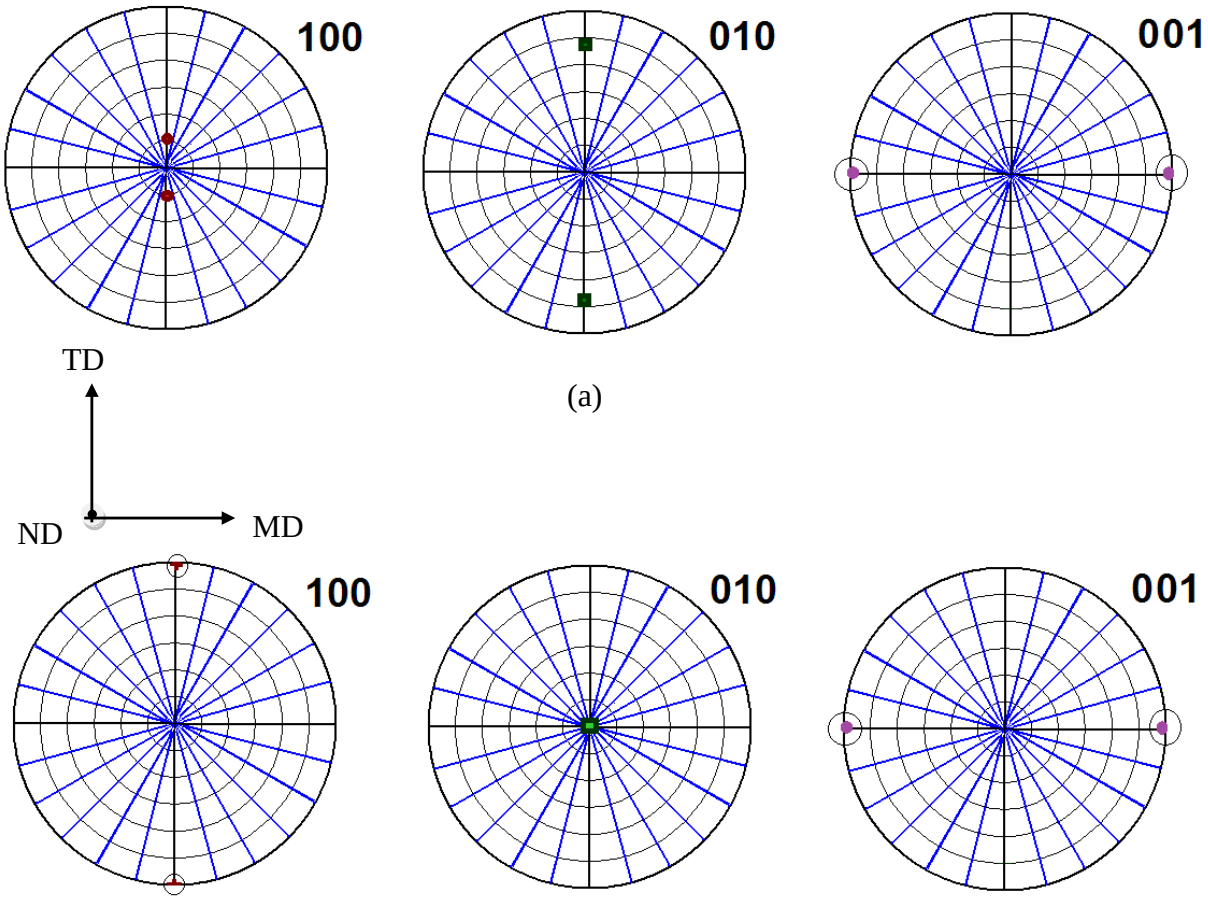

(a)

(b)

Figure 4.20: Calculated positions of ideal (a) (110)[001] type and (b) (010)[001] type texture elements on (100) and (010) and (001) pole figures

Figure 4.21 (a)-(d) provides more details on the orientation of the a* and b axes in the ND-TD plane for various draw ratios, particularly in the post-die deformation zone. The TD is shown by the ± x-axis; the y-axis at 0^o represents the ND. Intensity values collected at 90^o azimuthal angles, at various tilts are presented on the positive x-axis, whereas the values collected at 270^o azimuthal angles are presented on the negative x-axis.

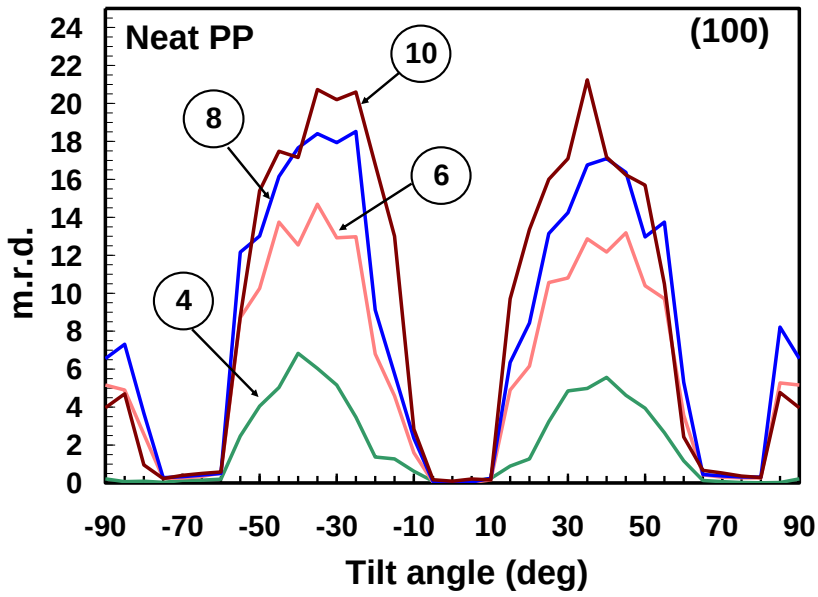

(a)

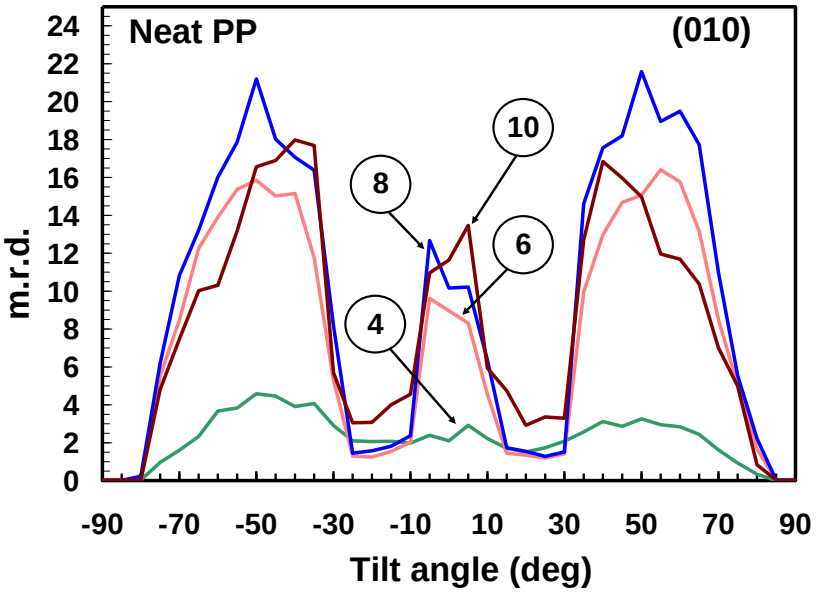

(b)

Figure 4.21: Peak intensities in the ND-TD plane on (a) 100-axis and (b) 010-axis of neat PP at locations 4, 6, 8, 9 and 10 or Final with corresponding DRs of 2.5, 5.1, 6.0, 6.5 and 8.8 (c) 100-axis and (b) 010-axis of PP-talc-20 wt. % at locations 4, 6, 8, 9 and 10 or Final with corresponding DRs of 2.4, 4.5, 5.8, 6.2 and 8.1.

Figure 4.21 (cont'd).

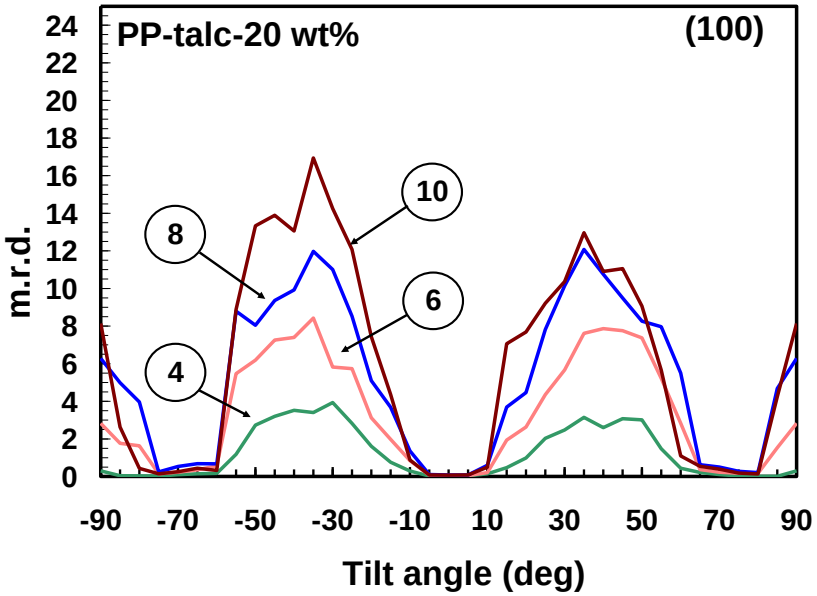

(c)

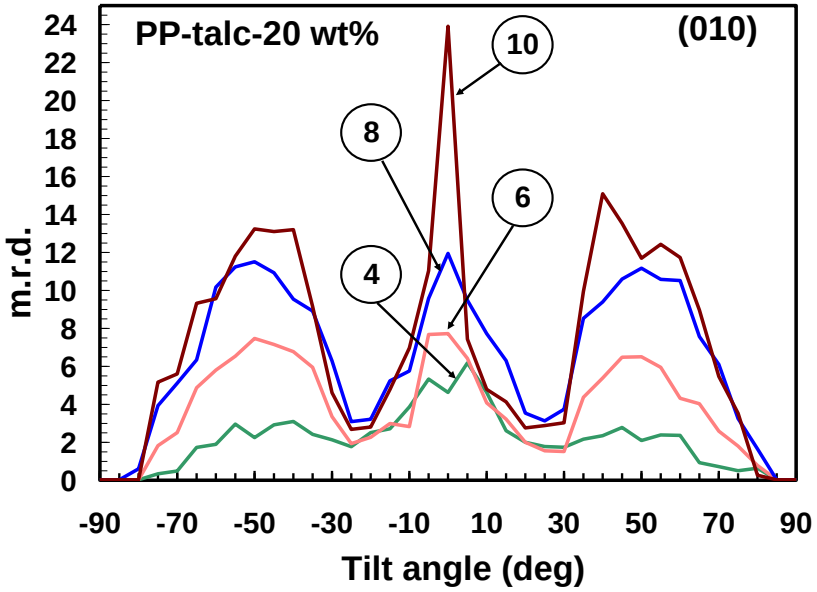

(d)

The stronger alignment of the b-axis along the ND within the drawn composite, at the final draw ratio is strikingly evident. In case of neat PP, the b-axis orientation was

stronger at the midway position between ND and TD. For comparison purposes, the relative extents of the two textures: (110)[001] or T_1 and (010)[001] or T_2 in the drawn materials were evaluated using the intensity maxima in the ND-TD planes of a*-axis and b-axis pole figures. Specifically, we noted the maximum values at $\pm 35^o$ on the (100) pole figures to asses T_1 and at 0^o on the (010) to asses the T_2. The relative intensities of the two texture components T1 and T2 have been plotted against draw ratio for the neat PP in Figure 4.22(a) and for the PP-talc composite in Figure 4.22(b).

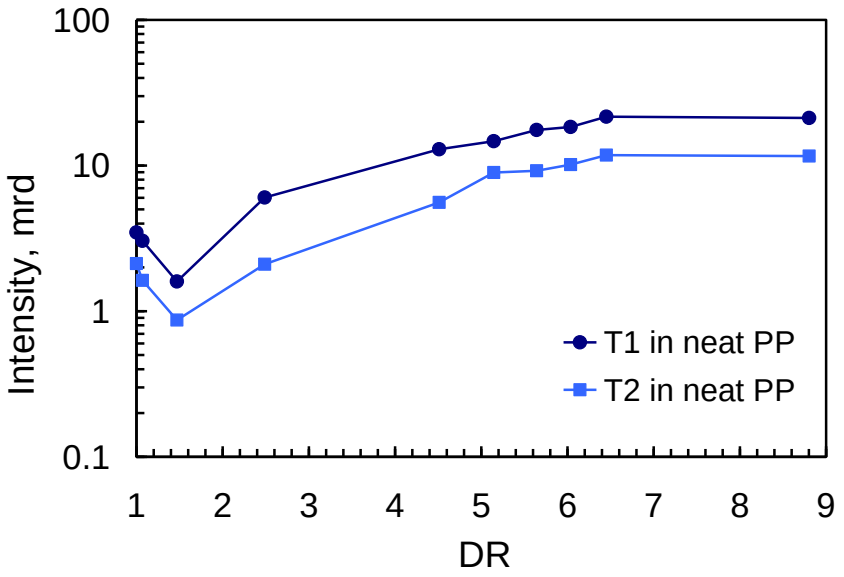

(a)

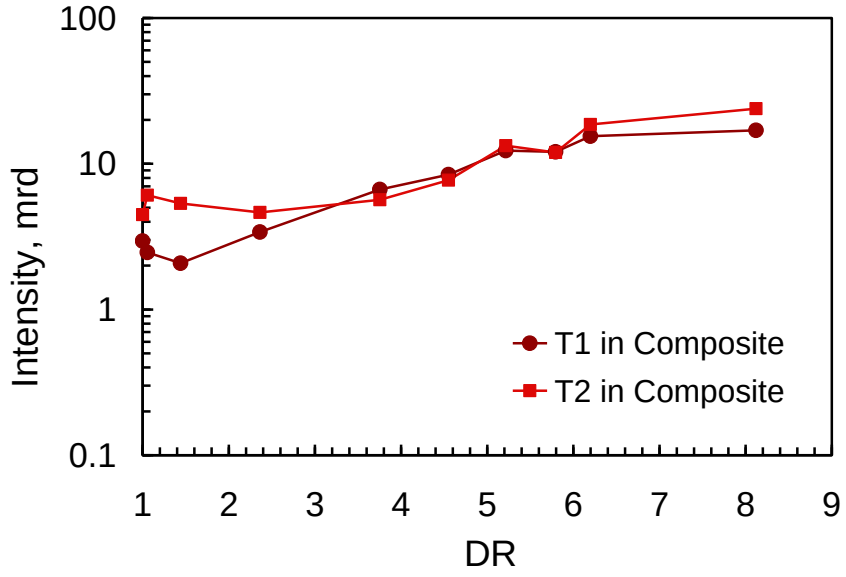

(b)

Figure 4.22: Development of the two texture elements viz. (110)[001]=T_1 and (010)[001]=T_2 vs. DR in (a) die drawn neat PP and (b) die drawn PP-talc composite.

The original (110)[001] texture is destroyed at the yield point, which occurs close to the die exit for neat PP (DR=1.5) but near the die entrance (DR=1.1) for the composite. After yield, both texture components are built up well into the free draw zone but the texture

development saturates for the neat PP at a draw ratio of 5.1 while this continues to a higher draw ratio of 6.2 in the case of the PP-talc composite. Furthermore, the developing texture and the final texture are dominated by T_1 for the neat PP while in the case of the composite; the final texture is dominated by T_2. The ratio of T_2 to T_1 was always higher for the composite (Figure 4.23). For both materials, the maximum draw ratio achieved is greater than the draw ratio at which the texture development saturates. This would indicate that the amorphous phase orientation continues to develop after the crystalline texture saturates.

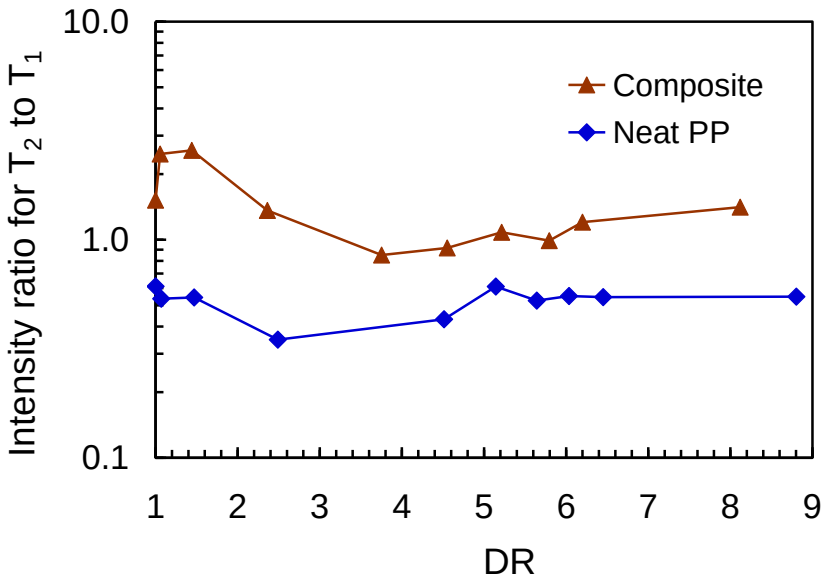

Figure 4.23: Plot of intensity ratios of texture T_2 to texture T_1 vs. draw ratio for the die-drawn samples of PP-talc-20 wt. % composite and neat PP.

The final crystalline c-axis orientation; attained at each draw rate tested is plotted against draw ratio in Figure 4.24. For similar draw rates, lower values of DR_{final} and c-axis orientation parameters were attained for the drawn composite than for the drawn neat PP.

Within the error bar, the crystal orientation in both drawn neat PP and drawn PP-talc-20 wt. % composite saturated above a DR_{final} of 7.

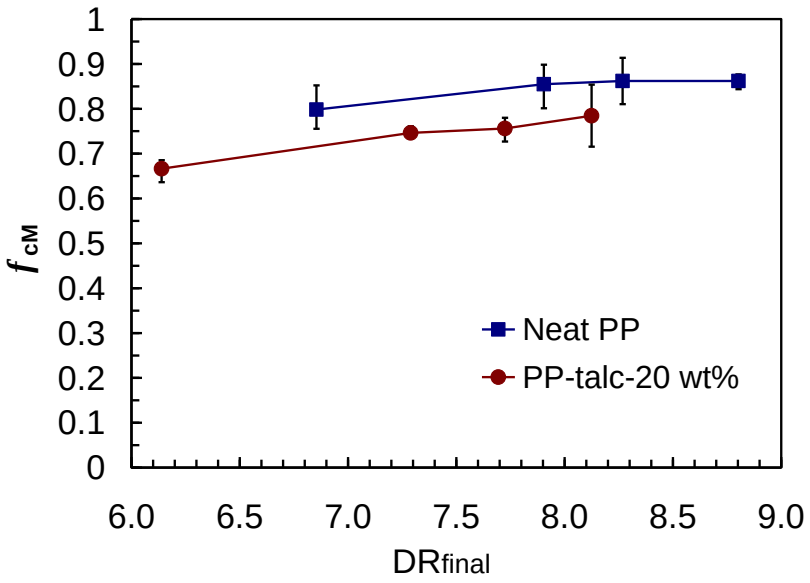

Figure 4.24: Herman orientation parameter of drawn materials as a function of final draw ratio attained at different draw rates.

4.3.4 Tensile Properties of Final Drawn Products

Tensile stress-strain curves for the undrawn and final die drawn (at 573 cm/min) billets of neat PP and PP-talc-20 wt. % composite are shown in Figure 4.25. Before die-drawing, the tensile modulus (slope of initial linear elastic region) of the composite was higher than the neat PP. The modulus of the composite before die drawing was mainly due to the reinforcement effect of the rigid talc particles. Die drawing led to an increase in the modulus for both the materials. Die drawing changed the relative trend in the moduli; for similar die drawing rates the modulus achieved for drawn neat PP was higher than drawn PP-talc composite. This trend was observed at all the draw rates studied here. In the case

of die drawn composite, the reinforcement was completely lost and the modulus enhancement was purely due to the highly oriented state of the matrix phase.

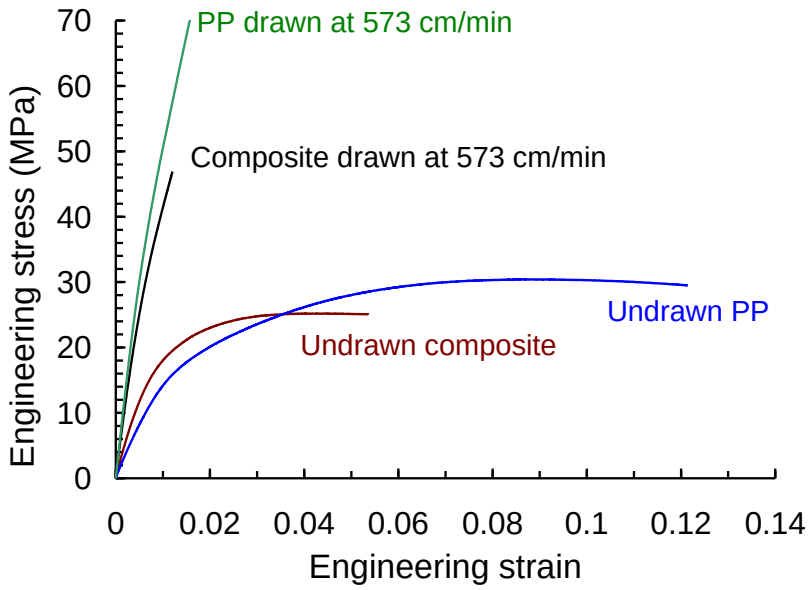

Figure 4.25: Tensile stress-strain curves for undrawn and die drawn (drawn at 573 cm/min) neat PP and PP-talc-20 wt. % composite.

The variation in tensile moduli for neat PP and its composite for different DR_{final} is shown in Figure 4.26. Despite the saturation in crystal orientation (Figure 4.24), as well as void growth (Figure 3.7(b)), the tensile modulus of the drawn composite increased with DR_{final}. A modulus increase of 4.4 fold was obtained for neat PP with the highest DR_{final}. Despite voiding in the material, the die drawn composite showed enhancement in tensile modulus with DR_{final}. For the highest draw ratio that could be attained in case of PP-talc composite, the modulus achieved on die drawing was as much as 3 times that of the undrawn neat PP, and 2 times that of the undrawn composite. The percentage crystallinity in drawn samples collected from the final deformation zones in our study

didn't change with draw rate. The crystalline volume fractions in the drawn samples of both of the materials were in the range of 55 to 59 %. The modulus enhancement for saturated levels of crystallinity, crystal orientation and void growth can be attributed to increased level of interlamellar amorphous phase orientation or higher aspect ratio of the oriented lamellar stacks in the drawn materials, as manifested by the larger area ratios (Figure 4.1) at higher draw rates.

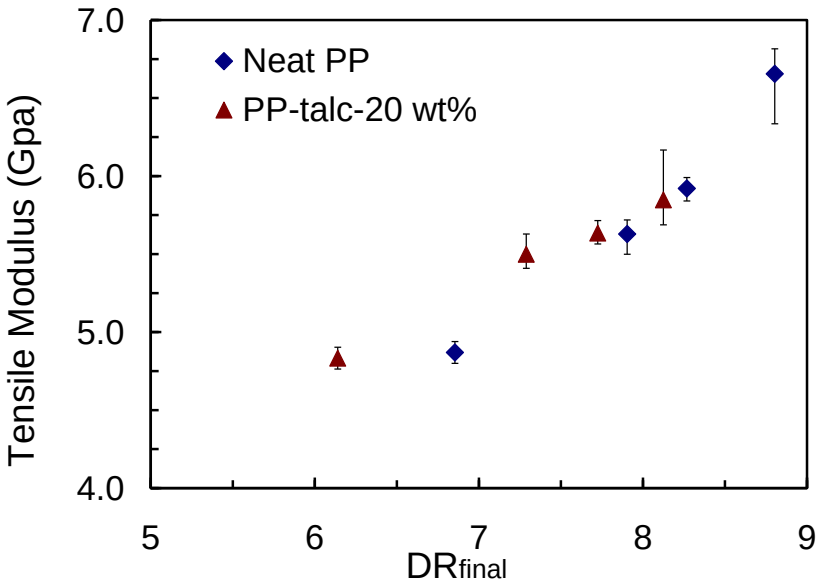

Figure 4.26: Tensile modulus of drawn materials as a function of DR_{final} attained for different draw rates.

4.4 Conclusions

In this research work we have studied the development of crystallinity and crystal structure in the matrix phase of PP-talc-20 wt.% composite as well as neat PP, that were die-drawn at 145^{o}C. In both of these materials, the processes of annealing and subsequent die drawing at a given draw rate led to about a 12 to 15 % increase in the crystallinity of

the matrix phase. Analyses of DSC endotherms and 2θ linear XRD patterns indicated that the die drawing operation resulted in transformation of the thermally less stable crystalline phase (mesophase) in un-oriented materials, to a more stable crystalline phase containing folded-chain α crystals. Pole figure measurements suggested presence of radially oriented crystal structures in undrawn composite. These crystal structures resembled the spherulitic domains found in unfilled PP, but with a different nucleation direction, because of the presence of talc particles. The differences in the initial morphologies of the undrawn materials were largely responsible for the differences in the modes of texture development found in the die drawn samples. Both neat PP and PP-talc composite yielded in the die deformation zone and showed well developed texture elements of (110)[001] and (010)[001] type in the post-die deformation zone. The results presented here show that the composite yielded at lower DR, but exhibited the above mentioned textures at higher DR than that of neat PP. In the intermediate range of draw ratios, a sharp void growth was observed for the drawn composite. When the two texture elements were quantified as a function of DR, it was noticed that the ratio of (010)[001] to (110)[001] was always higher for the die drawn composite. For comparable strains, the degree of crystalline c-axis orientation achieved for drawn composite was less than that of the drawn neat PP. The phenomena of particle debonding and void growth during composite drawing would have reduced the effective stress available for the molecular orientation of the matrix phase. Despite the saturation in crystallinity and crystal orientation (and void growth in the case of composite), the tensile modulus of the drawn materials increased with DR_{final}, that was obtained using increasing values of draw rates.

CHAPTER 5

MELT PROCESSING OF HIGH MOLECULAR WEIGHT HDPE-CLAY NANOCOMPOSITES

5.1 Introduction

Addition of a small percentage of nanoclay (layered silicates) to a polymer to achieve large improvements in the mechanical, barrier, thermal and other properties is well documented. Experimental studies on polymer-clay nanocomposites have frequently shown that complete exfoliation of the inorganic fillers in the polymer yields best performing systems. Because of the very high interfacial surface to volume ratio provided by the clay layers in this dispersion state, substantial improvements in the above mentioned properties are possible with lower levels of filler loadings. Relatively lower concentrations of the reinforcing fillers also offer some added advantages, such as low density, transparency, flexibility and ease of processing. The most commonly used layered silicates belong to the structural family known as the 2:1 phyllosilicates; more details on their smectic nature can be found in section 1.2.1. Because of its hydrophilic nature, it is difficult to disperse the nanoclay in a given polymeric matrix without some sort of organic modification. In general, the clay is organically treated with a primary alkyl ammonium ion. It is relatively easier to disperse the organoclay in a polar polymer matrix such as nylon. However, for polyolefins such as polypropylene or polyethylene the organic treatment of the nanoclays alone is not enough, and a third polarizing component is added to get well exfoliated clay nanocomposites. The polarizing component or the compatibilizer used is obtained by grafting the base polymer with some polar group like maleic anhydride. The reaction is carried out in a melt extrusion process

using a peroxide initiator. This leads to polymer scission, due to the formation of free radicals, and the melt viscosity of the compatibilizer formed is lower than that of the original polymer. During melt mixing step, the polar part of the compatibilizer gets bonded to the organoclay, whereas the non-polar part gets blended with the hydrocarbon chains of the base polymer. The final degree of dispersion in a given nanocomposite is decided by the extent of interaction among the various components of the blend, as well as the intensity of mixing.

5.2 Research Objective

Thin gauge sheeting made from high molecular weight high density polyethylene (HMW-HDPE) is used in automotive aftermarket-specifically as a masking alternative to paper in body repair shops. To obtain required tear strength and tensile strength the sheeting is typically manufactured in a 3-layer film blowing process. The film thicknesses can range from 12 μm down to 8 μm. Attempts to blow films with thickness less than 7.5 microns would result in unacceptable process instabilities and mechanical properties. This problem can be addressed by adding a small percentage of organoclay with appropriate compatibilizers. The main objective of this research work was to prepare well-dispersed nanocomposites of film grade HMW-HDPE, which would have an enhanced or equal processability as the base polymer. The intention was to obtain a similar level of mechanical properties with a reduced level of film thickness.

As described in the earlier section, maximum enhancement in the properties of the nanocomposite can be realized if the clay nanolayers or the platelets are completely separated from each other. Because of the very low melt flow rate (0.06 g/10 min.) of the base polymer, the task of preparing a well dispersed clay nanocomposite of HMW-HDPE

is faced with several challenges. First, the melt blending of this low MFR HDPE with other components would be hard without an execution of rigorous process parameters. Secondly, the very high molecular weight of the polymer chains would not only hinder the penetration of their own, but also of the compatibilizer chains into the clay galleries. For a HDPE of relatively higher melt flow rate (2 g/10 min.), Spencer and coworkers[94] were able to achieve exfoliated nanocomposites using ≥ 25% of maleated HDPE (HDPE-g-MA) of comparable melt flow rate (MFR). The very high molecular weight of the polymer in our case would necessitate higher concentration of a maleated polyethylene (PE-g-MA) compatibilizer. Moreover, since it is difficult to obtain a maleated PE (PE-g-MA) with as low MFR as the HMW-HDPE used in this study, the required loading level of PE-g-MA with a different MFR would be even higher. Lastly, a judicious selection of the process and material parameters is critical in deciding the melt strength of the nanocomposite formed; this is the most important criteria for getting a stable film during film blowing operation. The blowability of a polymeric material can be judged from its strain hardening ability in extensional flow; if strain hardening is observed in uniaxial extensional flow, it will be observed in biaxial extensional flow as well[95-97]. Thus, in order to qualify as a potential material for the film-blowing process, the nanocomposite must exhibit strain hardening ability in melt extensional flow[96].

To overcome the above discussed challenges, and to meet our objective we employed following strategies:

1) <u>Raw material selection:</u>

Organoclay

In their recent invention, Chaudhary, Pathak and Jayaraman[58] were able to obtain the strain hardening extensional viscosity behavior that is essential for foaming and film blowing for well-intercalated nanocomposites of linear polymers. They reported that this effect was especially noticeable when the organoclay was treated with chosen silane coupling agents. The silane treatment triggers higher physical, as well as reactive compatibilization with the compatibilizer. To extend this development, we decided to use the aminosilane treated organoclay used in their work.

Compatibilizer

The level of maleic anhydride (MA) provided by the compatibilizer must be sufficient to couple to all the reactive sites available on the organoclay surface and edges. If the MA level of the compatibilizer is too high, it may be immiscible with the bulk polymer because of the large polarity difference. Moreover, a high level of MA in the compatibilizer is usually associated with low molecular weights, which can also lower the mechanical properties of the final composite. Finally, the molecular weight of the compatibilizer or linking chains must be sufficient to raise the entanglement density with potential for strain hardening in melt extension. This work was done with two different compatibilizers - a low molecular wt. compatibilizer (with a higher MA content) and a higher molecular wt. compatibilizer of maleated HDPE (with a lower MA content).

2) Selection of Process Parameters:

We developed a mixing protocol in terms of sequence of addition of the raw materials and setting up the appropriate process parameters, such as mixing time, temperature, rpm, etc.

5.3 Material and Experimental Details

5.3.1 Materials

All the materials used for this part of the research work are listed in Table 5.1 with their commercial suppliers and technical specifications.

Material	Supplier-Grade	Designation	Specification
High molecular weight high density polyethylene	Exxon-HD7960	HMW-HDPE	MI=0.06 g/10 min, density=0.952 g/cc, Tm=134^{o}C
Low molecular wt. compatibilizer	Sigma Aldrich-456632 ALDRICH	SA	MA content=3 wt. % , Tm=103^{o}C Viscosity=1700-4500 cPs
High molecular wt. HDPE-g-MA compatibilizer	Dow Amplify GR205	GR205	MA content=1.2 wt. %, Tm=134^{o}C
Organically treated nanoclays	Southern Clay Products- Cloisite 15A	Cl-15A	Organic content =43 wt. %, density=1.66 g/cc, d-spacing=3.10 nm
	Nanocor-I.44P	I.44P	Organic content =35 wt. %, density=1.44 g/cc, d-spacing=2.50 nm
	Nanocor-NANOMER I.44P	Si-I.44P (Silylated I.44P)	Organic content =38 wt. %, density=1.77 g/cc, d-spacing=2.60nm (broader XRD peak)
Low molecular wt. HDPE	Ashland Inc.-HIVAL 521054	HIVAL	MI=21 g/10 min, density=0.952 g/cc
Commercial masterbatch of I.44P	Nanocor-nanoMax HDPE	Nanomax	Clay used: I.44P, clay loading=50 wt. %

Table 5.1: Constituents of HMW-HDPE nanocomposites with clay

The organoclay most suited to polyolefins has an onium ion surfactant specifically with two alkyl tails. The surfactant used in the organoclays for our study was dimethyl-di-octadecyl ammonium cation, with two –C18 tails in the case of I.44P from Nanocor,

whereas in case the of Cloisite 15A from Southern Clay Products, it was the onium ion with hydrogenated tallow. The I.44P had been further treated with an organic silane coupling agent, specifically Dow corning grade Z-6094 which was aminoethylaminopropyltrimethoxysilane (NH_2-$(CH_2)_2$-NH-$(CH_2)_3$-Si$(OCH_3)_3$); the resulting product is referred as Si-I.44P. The base polymer was a very high molecular weight HDPE with a melt flow of 0.06, which is processed at temperatures from 210 to 220^{o}C. The low molecular wt. compatibilizer (SA) has 3 wt. % MA, and the higher molecular wt. compatibilizer (GR-205) has 1.2 wt. % MA.

5.3.2 Nanocomposite Preparation

Compounds with various levels of clay, compatibilizer, and base polymer were prepared by melt mixing, either in a single stage or in a two-stage process. In single stage mixing, all the components, i.e. bulk polymer, organoclay and compatibilizer, were added at the same time. Two-stage mixing involved preparation of a masterbatch with a high loading of clay. Prior to compounding, the organically treated nanoclays, as well the PE-g-MA compatibilizers, were dried for 12 hrs., using a vacuum drier maintained at 80^{o}C and a vacuum of 20 in. Hg. Most of the mixing was carried out in Banbury type batch mixers. A schematic of this type of mixer is shown in Figure 5.1. Banbury type batch mixers of two different mixing capacities were used for melt mixing- one with 50 g capacity from Brabender, and another with 200 g capacity, which was mounted on a Polylab OS torque rheometer. The torque–time curve obtained from the torque rheometer was used to decide the time required for mixing, as done by Rezanavazz et al.[100].

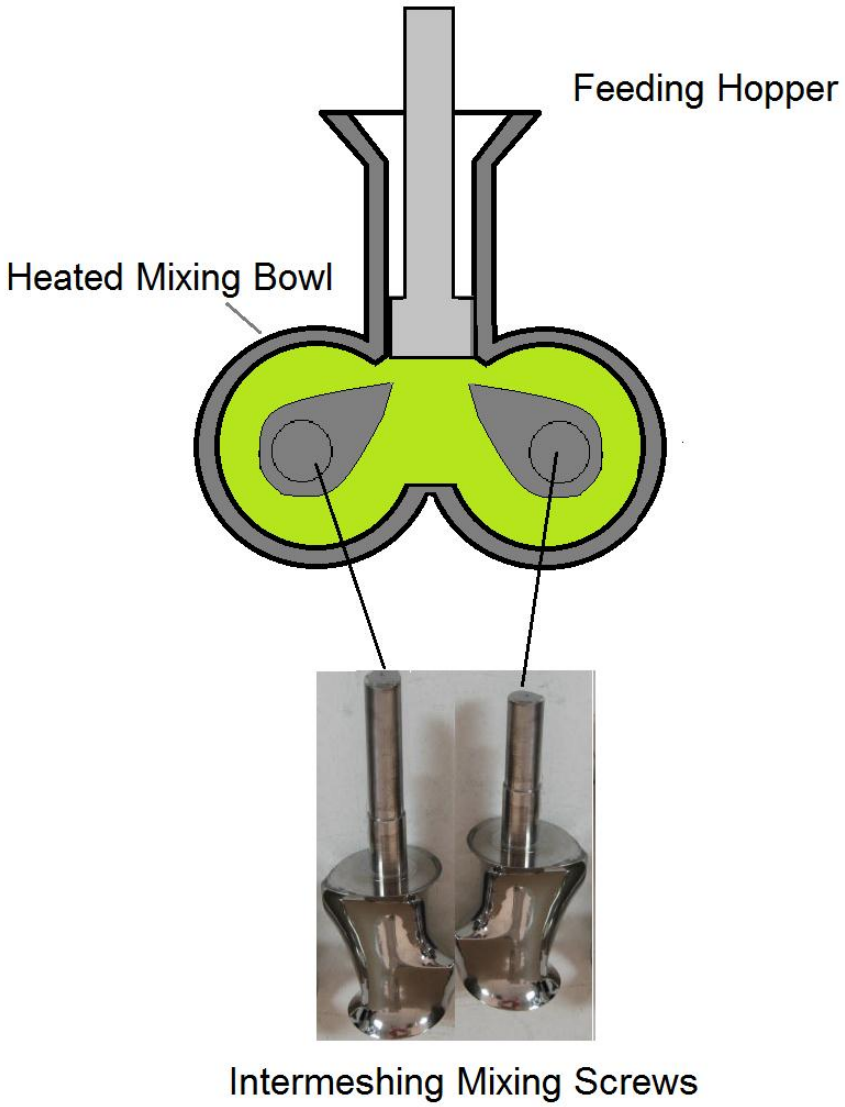

Figure 5.1: Schematic of a Banbury type batch mixer used for melt blending.

Preparation of the masterbatch (MB), which did not involve the HMW-HDPE, was carried out at 150 to 160^{o}C and at 150 rpm, for 12 to 15 minutes. For single-stage mixing, as well as for the let-down step of the two-stage mixing, the melt temperature was maintained at 210^{o}C for 20 minutes. The very high viscosity of the HMW-HDPE leads to an increase of up to 80^{o}C in the melt temperature, and therefore, temperature

control was critical during mixing. The melt temperature was maintained below 220^{o}C by controlling the set temperatures and mixing speed (rpm). The mixing was carried out under a nitrogen blanket and with Irganox to minimize oxidative thermal degradation. Chunks of melt mixed material were collected from the mixing bowl using a copper spatula and brass scraper. These chunks were then molded to prepare samples for X-ray diffraction (XRD) and rheological studies. For molding flexural bars, the chunks were granulated in a mini granulator.

Continuous melt-mixing was used to prepare kg samples of one masterbatch (MB3) and its two let-down batches, LD1-3 and LD2-3 (to be discussed later). This was done with a Cooperion intermeshing and co-rotating twin screw extruder ZSK-25 (screw diameter= 25 mm, L/D=44). The masterbatch was compounded using a feed rate of 1 to 2 kg/hr, a barrel temperature of 140-145^{o}C (melt temperature =160 to 165^{o}C), and an rpm of 250. During let-down, the barrel temperature was set to 130-140^{o}C (melt temperature =210 to 224^{o}C), and mixing was done with a feed rate of 1.5 kg/hr. and 300 rpm.

5.3.3 Sample preparation

Specimens for X-ray diffraction (XRD) and rheological tests were molded in a Wabash compression molder. A 1 mm thick circular mold with 40 mm diameter was used to mold XRD samples, whereas to mold samples for testing elongational rheology, a mold with a grid of rectangular cavities (each with 18 x 10 x 0.75 mm^{3}) was used. The polymer blobs were put on the mold and allowed to melt at 200^{o}C, and then subjected to a pressure of 5 tons for 3 minutes, and 8-10 tons for 5 minutes. The melt was cooled under pressure to

room temperature using cooling water circulated through the mold. The molded samples were visually checked to make sure that they were free of any voids and foreign particles.

To prepare flexural bars, the materials were melted using a DSM micro15 compounder (a conical and co-rotating mini twin screw extruder) operated with a set T of 210^{o}C and 50 to 100 rpm. The melt was then transferred at 210^{o}C, using a Daca micro injector system with pressure of 150 psi to a mold maintained at 70^{o}C.

Blown films of the nanocomposite and base HDPE were obtained using a lab-scale film blowing unit that was fitted with a die of 25.4 μm annular gap. The L/D of the extruder screw was 31. For preparing films using LD2-3, a let- down batch with 5 wt. % of Si-I.44P clay and a blow up ratio of 4.5:1 was used. A film of base HDPE was also produced for comparison. The extrusion temperature for the nanocomposite was set to 190^{o}C, which is 20^{o}C below the processing temperature used for base HDPE. For preparing blown films using LD1-4: a let-down batch with 3 wt. % Si-I.44P a blow up ratio of 2.5:1 was used. The films of LD1-4 could be blown with the same settings as that of neat HMW-HDPE.

5.3.4 XRD

X-ray diffraction technique (XRD) was used for structural characterization of the organically modified clays; their concentrates or masterbatches and the final let-down batches or HMW-HDPE nanocomposites. The technique works on the principle of X-ray scattering. The crystals in a material are assemblies of regular spaced atoms, which scatter or diffract the X-ray beam in a certain pattern based on their inter-atomic distance.

The d-spacing between the scattering sites is obtained using Bragg's law given by equation 5.1.

$$n\lambda = 2d\sin(\theta) \qquad (5.1)$$

Where, 'n' is the order of reflection, 'λ' is the wavelength of the X-ray beam, 'd' is the spacing between atoms or plane, and 'θ' is the angle of diffraction. In this part of the work, only first order diffraction was considered**.**

XRD patterns in reflection mode were obtained using a theta-theta Bruker Davinci Diffractometer which was equipped with a Ni-filtered Cu Kα radiation source, and operated at 45 kV and 45 mA. This instrument has four diffraction slits: one between the X-ray source and the sample; two between the sample and the goniometer and the last slit is mounted on the detector (0.6^{o}) side. The first three diffraction slits were fixed, whereas the selection of the diffraction slit on the detector was made based on the resolution and intensity of the diffraction peak of interest, which in our case was that of clay d-spacing. XRD scans were run for the nanocomposites. The d-spacing of the clay present in each material was calculated using Equation 5.1.

To obtain the XRD pattern of the clay samples, the powder samples were compacted on a glass disc with a cavity of 25 mm diameter and 3 mm thickness. For the masterbatches or nanoclays, as well as the final nanocomposites, 35 mm diameter compression molded discs, fitted on 40 mm diameter glass sample holders were used. XRD patterns of all the samples were recorded using a 3.0^{o}/min scan rate over the 2θ range of 0.4 to 10^{o}, with equal increments of 0.02^{o}.

Natural montmorillonite clay has a mean interlayer basal spacing of (001) plane (d-spacing) of about 0.95 nm. The organic treatment by various alkyl ammonium surfactant leads to intercalation of the surfactant molecules inside the clay galleries, resulting in an increase in d-spacing. For the nanoclay treated with onium ion surfactant with two alkyl tails-C18 (I.44P), the d-spacing increased to 2.50 nm. Silane treatment of this clay led to broader d-spacing with a shallow peak intensity, corresponding to a d-spacing of 2.60 nm. The highest d-spacing was recorded for Cloisite 15A clay that has onium ion surfactant with hydrogenated tallow.

5.3.5 Extensional Rheology

The extensional rheology tests were performed to study the melt behavior of the material in shear free elongational flow. It is of particular importance in various commercial processes such as film blowing, foaming, blow molding, fiber spinning, thermoforming, etc. Since this part of the work deals with production of blown films, the extensional melt behavior of a given polymeric material was crucial for assessment of its film forming ability. Because of the presence of shear stresses at stationary boundaries, homogeneous extensional flows are difficult to generate. In our study we have tested the polymeric melt, using an extensional viscosity fixture (EVF) for their uniaxial extensional flow behavior.

In the EVF test, a rectangular test specimen is subjected to an axi-symmetric deformation where a tensile stress is applied along the longest dimension, and the other free surfaces of the specimen undergo compression. For our research we used a TA ARES rheometer that was mounted with EVF. The design of the fixture is based on the original concept by Meissner[101]. The EVF fixture consists of two cylinders-a stationary cylinder that is

connected to a force transducer, and a rotating cylinder that rotates around the stationary cylinder to wind up the sample (Figure 5.2).

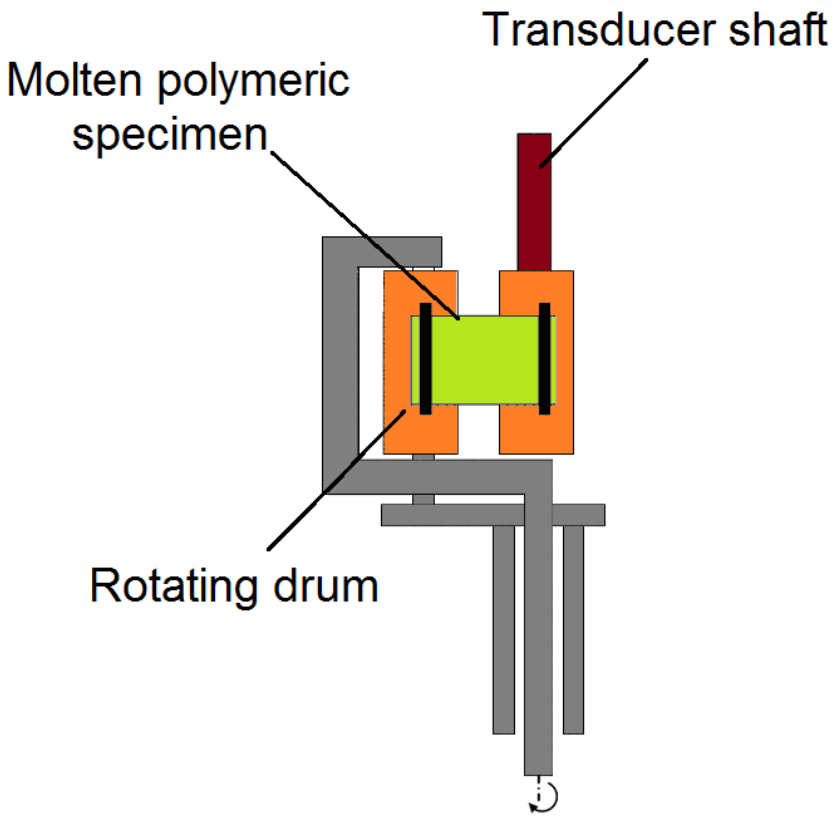

Figure 5.2: Schematic of an extensional viscosity fixture (EVF) used to measure extensional viscosity behavior of polymeric melts.

The extensional stress σ_e (Equation 2.4) is obtained by using the measured extensional force F and the cross sectional area A of the sample. Both of these are functions of time.

$$\sigma_e(t) = \frac{F(t)}{A(t)} \qquad (5.2)$$

The extensional force is then used to calculate transient uniaxial viscosity (η_e^+) using Equation 5.3.

$$\eta_e^+(t) = \frac{\sigma_E(t)}{\frac{d\varepsilon_H}{dt}} \qquad (5.3)$$

Here, $\frac{d\varepsilon_H}{dt}$ represents the applied strain rate. An ARES rheometer, with an extensional viscosity fixture (EVF) by TA instruments was used to study extensional rheology of polymeric melts. The extensional viscosity transients for melts were measured at temperatures well above the melting temperature of the material. This was done by subjecting the melt to a constant Hencky strain of 2.5, using various strain rates like 0.1, 0.5, 1 and 2 s^{-1}. The high molecular weight HDPE based samples were conditioned for 5-7 minutes at the test temperature to ensure their thorough melting. These tests are very sensitive to the sample condition, so care was taken to ensure that the samples were even and free of any voids or defects. Once the test was over, the geometry of the stretched specimen was checked to ensure that the sample was stretched uniformly without sagging. The results of non-uniformly stretched samples were discarded and only the data for the uniformly stretched samples were taken into consideration.

5.3.6 DSC

Thermal properties of the neat HMW-HDPE, compatibilizers used and the nanocomposites prepared were measured on a differential scanning calorimeter (DSC) Q10 by *TA* instruments. It was operated under nitrogen purge of 50 ml/min. The working principle involved and other details are given in section 2.2.7. The DSC curve for a given sample was obtained by subjecting 5-10 mg of its specimen to a heat/cool/heat cycle from

40 to 200^{o}C, at a heating rate of 5^{o}C/min. The first heating cycle relieves any thermal stresses present in the specimen. Values of heat of fusion were obtained with the help of Universal Analysis 2000 software (version 4.5A) by TA instruments. The position of the melting peak of a melt mixed compound, in comparison with the melting peaks of the individual components involved, can indicate the degree of compatibility among them.

5.3.6 Flexural Tests

Room temperature flexural tests were performed by a three point bending method to evaluate flexural modulus and strength of the samples; a Universal tester, fitted with 5 kN load cell and a 50 mm span was used. Load vs. deflection curves for different samples were recorded at a testing rate of 5.08 mm/min. Following the guidelines of ASTM D790, the span length was set to a equal to 16 x thickness of the flexural bar. Load vs. displacement of the given flex bar is recorded and used to calculate flexural modulus, flexural strength, and flexural strain. Flexural modulus was determined for the initial linear elastic region using Equation 5.4.

$$E_{flex} = \frac{mL^3}{4bh^3} \qquad (5.4)$$

Where:

E_{flex} = Flexural modulus, m = initial slope of the load vs. deflection curve

b = width of beam tested, h = thickness of beam tested and

L = specimen length between two support points

The flexural strength σ_y and the flexural strain ε_y were calculated with the help of Equation 5.5 and Equation 5.6 respectively.

$$\sigma_y = \frac{3PL}{2bh^2} \qquad (5.5)$$

Where,

P= peak load occurring at the yield point of the load displacement curve.

$$\varepsilon_y = \frac{6\delta_y h}{L^2} \qquad (5.6)$$

Where,

δ_y= deflection at the yield point.

5.3.8 Film Testing

The film samples prepared were generously tested by Petoskey Plastics in Petoskey, Michigan. Tensile tests on the films were performed on a Thwing-Albert Instrument's tensile testing unit as per the ASTM standard D882. Twenty 190 mm x 25 mm strips cut in machine direction (MD) and transverse direction (TD) were tested for tensile properties. The tear strengths of film samples were tested on Elemendor tear tester as per ASTM standard D1922. For a given film sample, twenty 75 mm x 62.5 mm strips each in MD as well as TD were cut for these tests.

5.4 Results and Discussion

5.5.1 Effect of Mixing Time

The effect of different mixing times on the extent of organoclay dispersion was investigated in the Brabender batch mixer, using the high molecular weight maleated HDPE grade GR205 alone as matrix. Results are presented here for a composite with 3 wt. % of Cloisite 15A (Southern Clay Products) and 97 wt. % of GR-205. Similar results were obtained with 3 wt. % of I.44P from Nanocor and 97 wt. % of GR-205. The mixing temperature was 200^{o}C. The extent of dispersion indexed by the d-spacing of clay in the nanocomposite increased progressively as the mixing time was increased from 5 min to 10 min to 15 min as shown in Figure 5.3. This trend points out the necessity of using greater mixing times when HMW-HDPE is the bulk polymer.

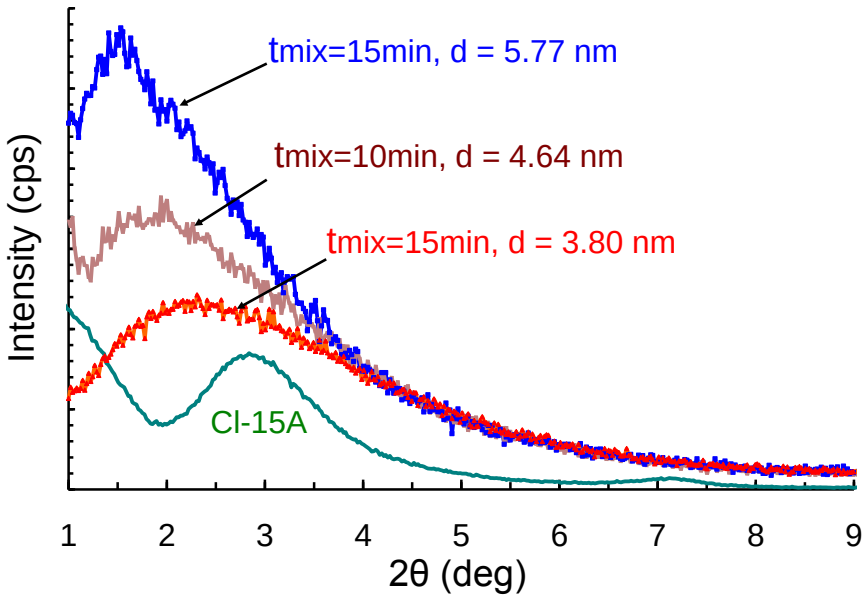

Figure 5.3: Effect of mixing time for GR205/Cl-15A (97/3 wt/wt) nanocomposites prepared on a small Brabender mixer.

5.5.2 Two Stage Mixing vs. Single Stage Mixing

5.5.2.1 Single Stage Melt Mixing

One shot mixing or single stage mixing of different compositions of HMW-HDPE, GR205, and organoclay were tried in a batch mixer. For example, nanocomposites of HMW-HDPE and Cl-15A, using two different levels of GR205 (12.4 wt. % and 24.7 wt. %) in the matrix phase, were compounded in the Polylab OS torque rheometer at 210ºC for 20 minutes. XRD patterns of these two composites are given in Figure 5.4.

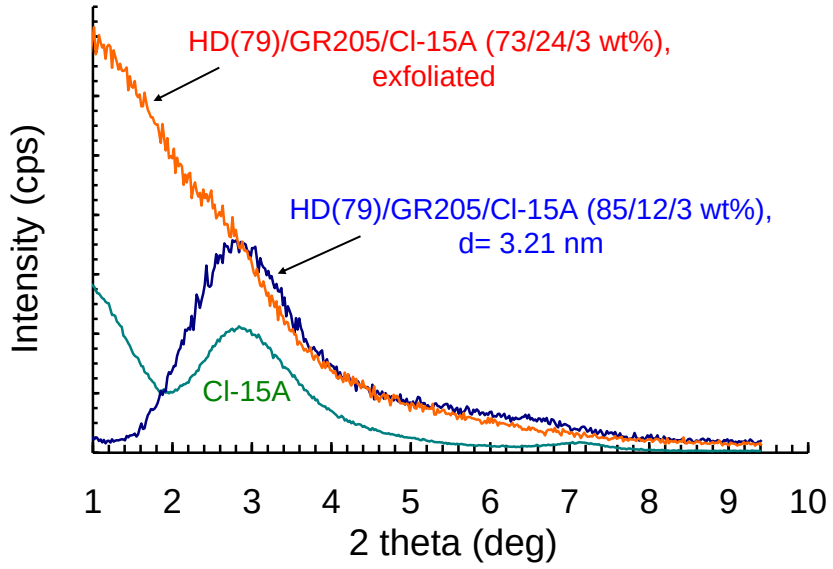

Figure 5.4: XRD patterns showing the effect of compatibilizer loading on dispersion in single shot mixing. The compounds were prepared using Polylab (OS) torque rheometer.

As seen here, the composite with 24.7 wt. % of GR205 in the matrix phase, or with compatibilizer to clay ratio of 8:1, showed exfoliation, while the composite with compatibilizer to clay ratio of 4:1 showed an increase in d-spacing of only 0.11 nm. Thus, very good dispersion of the Cl-15A organoclay was obtained with about 25 wt. % of GR-205 in the matrix polymer blend. This is consistent with trends reported by Spencer

et.al[94], where 25 wt. % of compatibilizer with similar viscosity to that of the base HDPE was required to achieve exfoliation. For HMW-HDPE nanocomposites with Si-I.44P, 25 wt. % of GR-205 was not enough to attain exfoliation. An increase of 0.25 nm in d-spacing was obtained for this case; the total level of maleic anhydride was critical with silylated clay because of the reactive coupling.

The required level of compatibilizer may be reduced by preparing a masterbatch with significant amounts of clay and carrying out the mixing in two stages. Nanocor has used this approach; they supply masterbatches of I.44P clay for polyolefins. The following steps were followed: firstly the commercially available Nanocor masterbatch (Nanomax-HDPE) was tried for HMW-HDPE in a let-down process. Secondly, a masterbatch using the silane treated organoclay was prepared, and let-down with the base HMW-HDPE. The silane treated clay was expected to (i) preserve the strain hardening ability of the base polymer in extensional melt flow, and (ii) impart adequate improvements in the mechanical properties.

5.5.2.2 Two Stage Melt Mixing

Figure 5.5 shows XRD patterns for the masterbatch- Nanomax and its let-down batch with HMW-HDPE. The Nanomax was available commercially from Nanocor and contained 50 wt. % of I.44P. Its let-down batch with HMW-HDPE had 5 wt. % of I.44P in it. The let-down batch was prepared on the Polylab OS torque rheometer, by mixing the Nanomax with HMW-HDPE at 210^{o}C for 20 min. The Nanomax masterbatch which was prepared using a twin screw extruder showed an increase of 0.56 nm in d-spacing from the base clay. Second stage mixing with Polylab OS mixer resulted in satisfactory

clay dispersion, giving a total increase of 1.4 nm in d-spacing. Based on these results, we decided to pursue two-stage mixing, particularly with silylated I.44P clay (Si-I.44P). The HMW-HDPE was not incorporated in the masterbatches; instead, up to 30 wt. % of a 21 MFI HDPE (HIVAL) was added while compounding the organoclay with the compatibilizer. Initial masterbatches with Si-I.44P were prepared using GR205. The low viscosity of HIVAL was expected to give better mixing.

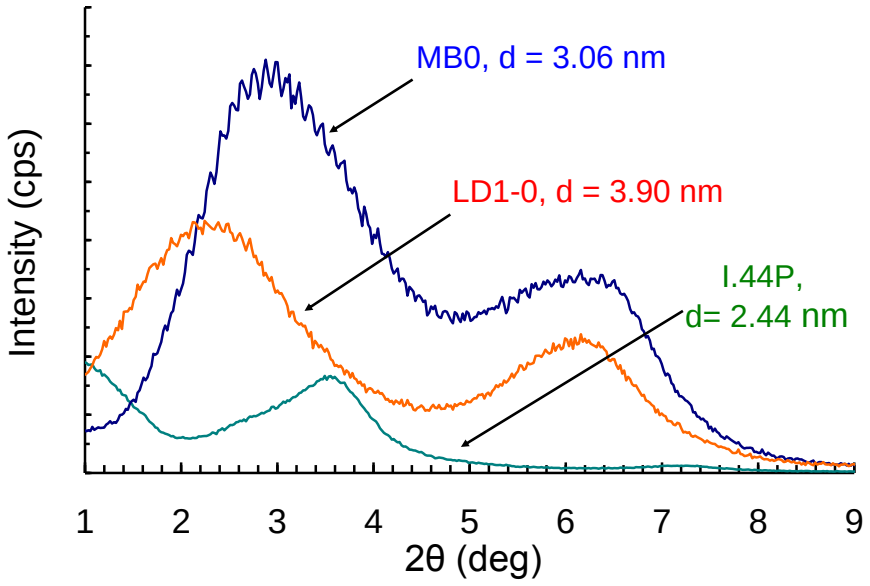

Figure 5.5: XRD patterns for a commercially available masterbatch MB0 with 50 wt. % I.44 P clay and its let-down compound LD1-0: HMW-HDPE/MB0 (90/10 wt.%) prepared on Polylab (OS) torque rheometer

Figure 5.6 presents XRD patterns for the MB of Si-I.44P with GR205, and its let-down batch with HMW-HDPE prepared on the small Banbury mixer. Although the MBs with GR205 showed an increase of 0.5 to 0.6 nm in clay d-spacing, the d-spacing collapsed in the let-down batches of these MBs with HMW-HDPE. Varying the proportions of GR205 in the masterbatch, as well as in the let-down step, did not improve dispersion in

the let-down product. As a result, we tried a different compatibilizer in the masterbatch, SA, that has 3 wt. % of maleic anhydride.

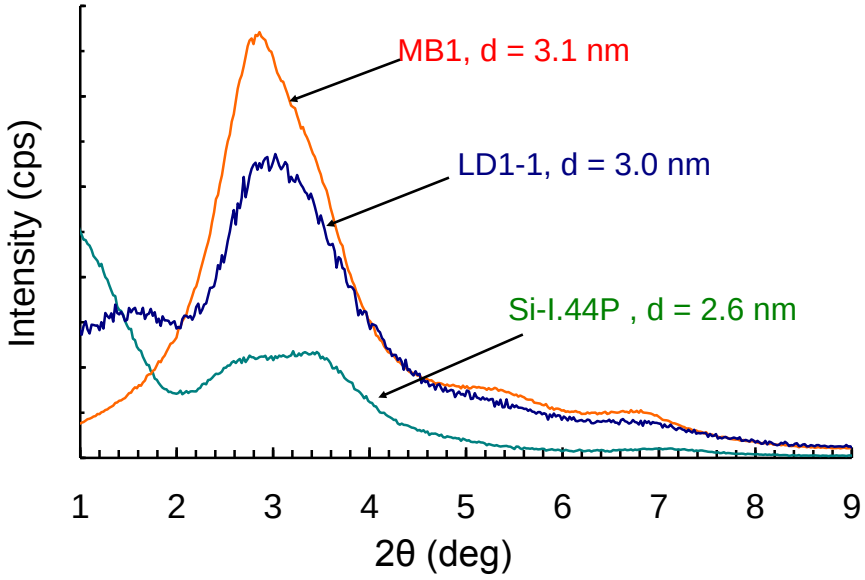

Figure 5.6: XRD patterns of masterbatch MB1 with Si-I.44P/GR205/HIVAL (30/30/40 wt. %) and its let-down LD1-1 compound: HMW-HDPE/MB1 (83.3/16.7 wt. %), prepared on the Brabender mixer.

The XRD patterns of one such masterbatch and several different corresponding let-down batches are presented in Figure 5.7. As Figure 5.7 shows, the masterbatch prepared with SA had a greater d-spacing. The let-down of this masterbatch with HMW-HDPE showed same d-spacing as the MB. Upon addition of GR205 during the let-down step (LD 2-2), we obtained an increase in d-spacing from the masterbatch to the let-down composite. Increasing the level of GR205 at the letdown stage revealed that there was an optimum level (10 wt. %) of GR205 for good dispersion of the organoclay.

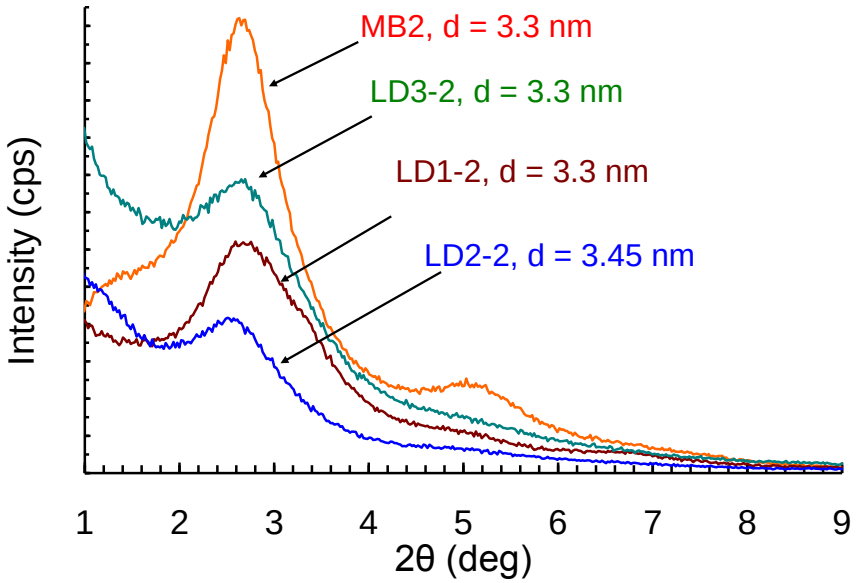

Figure 5.7: XRD patterns of masterbatch MB2 with 40/30/30 wt. % of Si-I.44P/SA/Hival and its let-down compounds LD1-2: HMW-HDPE/MB2 (87.5/12.5 wt. %), LD2-2: HMW-HDPE/GR205/MB2 (77.5/10/12.5 wt. %) and LD3-2: HMW-HDPE/GR205/MB2 (71.5/16/12.5 wt. %).

We decided to make another slightly different masterbatch, and also let it down with HMW-HDPE on a twin screw extruder (TSE) that would generate larger samples for film blowing tests. Figure 5.8 shows XRD patterns for these three compounds. An increased d-spacing of 3.39 nm was obtained in the masterbatch with 40-35-25 wt. % of Si-I.44P/SA/HIVAL.

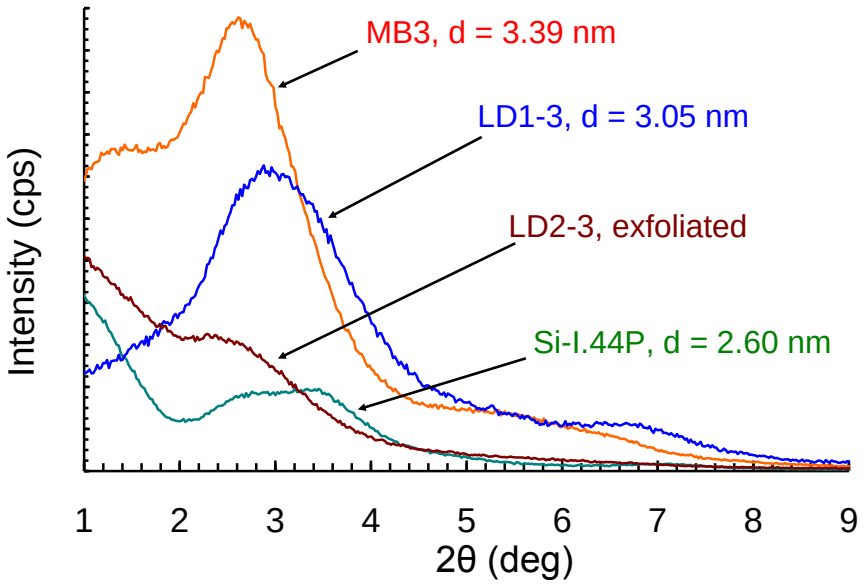

Figure 5.8: XRD patterns of MB3 with Si-I.44P/SA/HIVAL (40/35/25 wt. %) and its let-down compounds: LD1-3 with HMW-HDPE/MB3 (87.5/12.5 wt. %) and LD2-3 with HMW-HDPE/GR205/MB3 (77.5/10/12.5 wt. %) prepared on a twin screw extruder.

The DSC curves (Figure 5.9) showed high compatibility between the maleated low molecular weight compatibilizer and the high density polyethylene. This was let-down with additional GR205 and HMW-HDPE to prepare a compound with 5 wt. % of nanoclay. A different let-down, without any additional GR205, was also compounded for comparison; the d-spacing did not improve with this straight let-down. We obtained exfoliation of clay in the let-down batch with 10 wt. % of GR205.

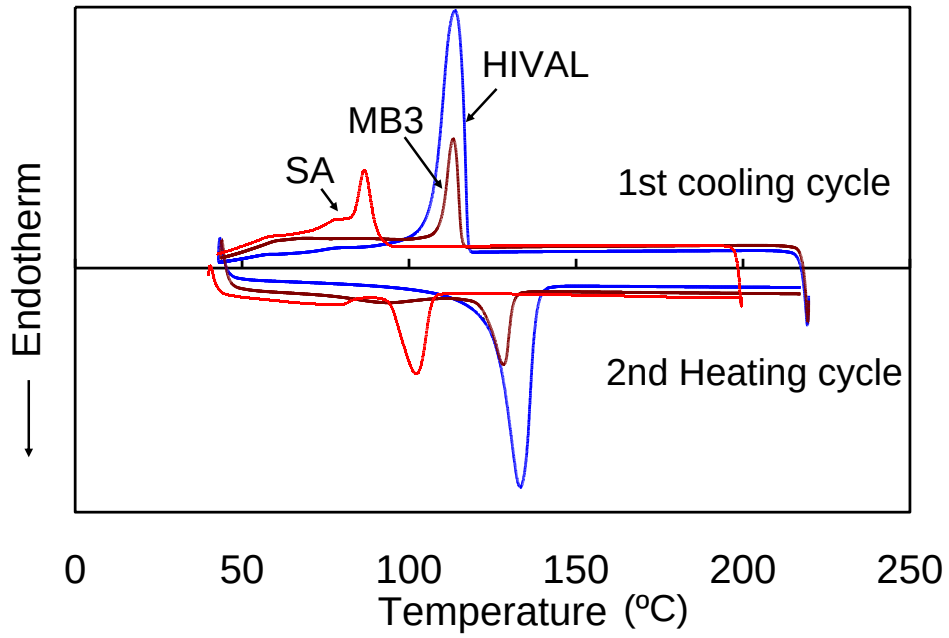

Figure 5.9: DSC curves of low molecular weight compatibilizer (SA), high density polyethylene (HIVAL) and their masterbatch (MB3 with Si-I.44P clay).

5.5.3 Flexural Properties with Injection Molded Bars

Five flexural bars were tested for each of three different materials: the HMW-HDPE, the Nanomax let-down with 5 wt. % I.44P, and the exfoliated compound described in Figure 5.6 with 5 wt. % silylated organoclay, Si-I.44P, and 10 wt. % GR205. The results are presented as bar graphs of flexural modulus, yield strength, and yield strain in Figures 5.10-5.12.

The newly formulated HMW-HDPE nanocomposites with 5 wt. % of Si-I.44P clay showed an improvement of 19 % in the flexural modulus (Figure 5.10) and 7 % in flexural strength (Figure 5.11). The flexural yield strain of this nanocomposite was also comparable to that of neat HDPE (Figure 5.12). As seen in these figures, there was more variation in the mechanical properties of the nanocomposite compounded on the twin screw extruder. Ideally, to keep the proportions uniform, the masterbatch and the bulk

polymer should be fed by different feeders. This was not done; the components were shaken together before feeding through one feeder which might have led to non-uniform proportions.

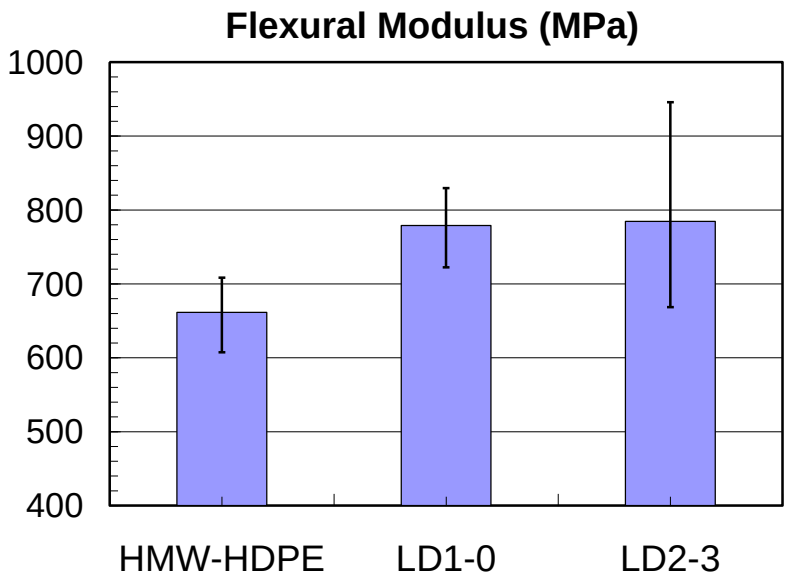

Figure 5.10: Flexural modulus of HMW-HDPE, LD1-0: HMW-HDPE/MB0 (90/10 wt. %) and LD2-3 with HMW-HDPE/GR205/MB3 (77.5/10/12.5 wt. %)

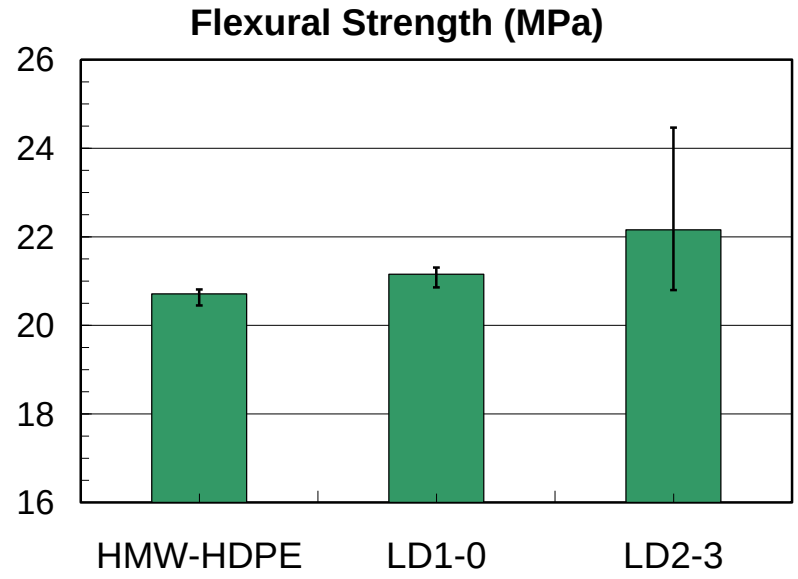

Figure 5.11: Flexural strength of HMW-HDPE, LD1-0: HMW-HDPE/MB0 (90/10 wt. %) and LD2-3 with HMW-HDPE/GR205/MB3 (77.5/10/12.5 wt. %)

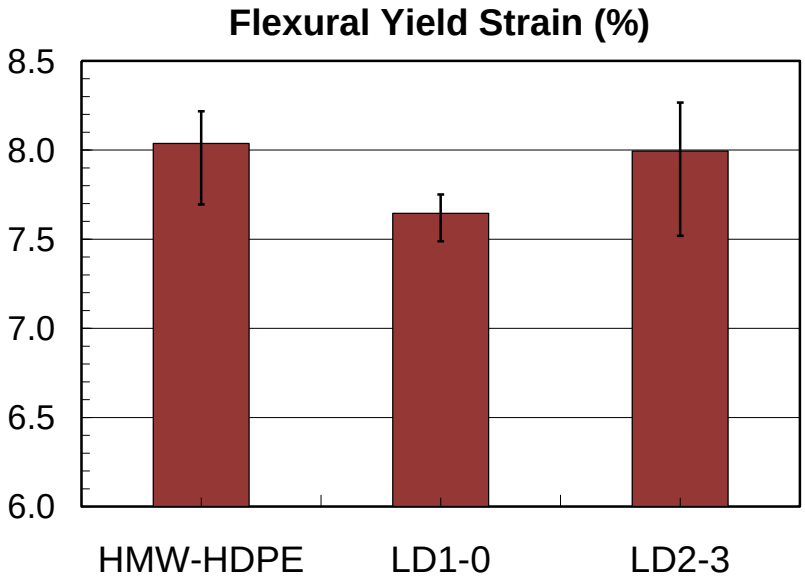

Figure 5.12: Flexural yield strain of HMW-HDPE, LD1-0: HMW-HDPE/MB0 (90/10 wt. %) and LD2-3 with HMW-HDPE/GR205/MB3 (77.5/10/12.5 wt. %)

5.5.4 Film Blowing and Processability

Resins used for film blowing should have adequate melt strength in biaxial extensional flow[96, 102]. This property or blowability can be assessed by measurements of the uniaxial extensional viscosity transient at the melt temperature of interest. Figure 5.13 for HMW-HDPE shows a lift-off in extensional melt viscosity when tested at 210^{o}C.

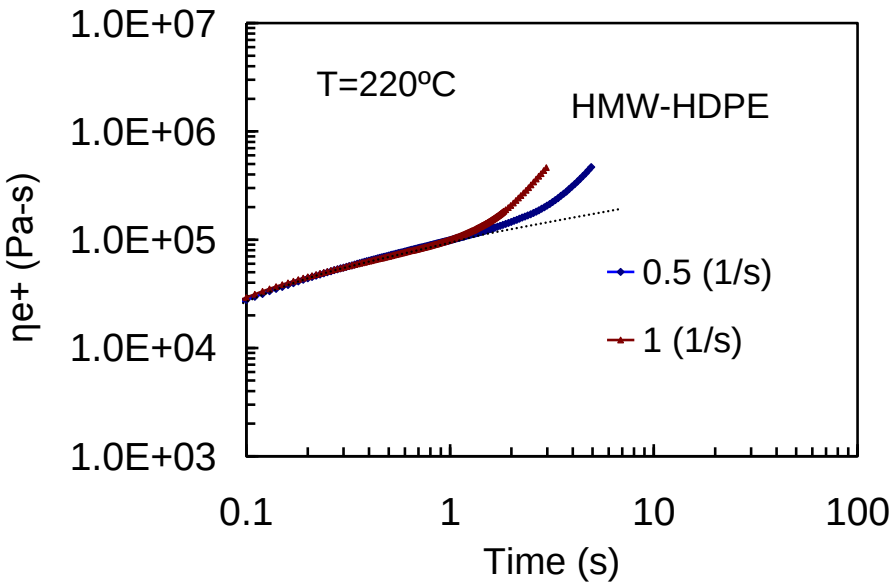

Figure 5.13: Uniaxial melt extensional viscosity of neat HMW-HDPE conditioned for 7 minutes before testing at 210^{o}C.

In general, addition of fillers to the polymer melt brings down the strain hardening in melt extension flow. However, strain hardening of the extensional viscosity can be maintained, or even enhanced in some nanocomposites by careful selection of the compatibilizer and the coupling between the organoclay and the compatibilizer[98, 99.]

Figure 5.14 shows the uniaxial extensional viscosity transients for GR205 and its composite with 3wt. % Cl-15A, that was mixed for 15 minutes. Neat GR205 itself strain

hardens at different strain rates; the degree of strain hardening went up for the GR205 composite with well intercalated Cl-15A clay. Due to its strain hardening ability, this compatibilizer is expected to retain the melt blowability of the base HMW-HDPE resin, which is another reason why it was a compatibilizer of choice.

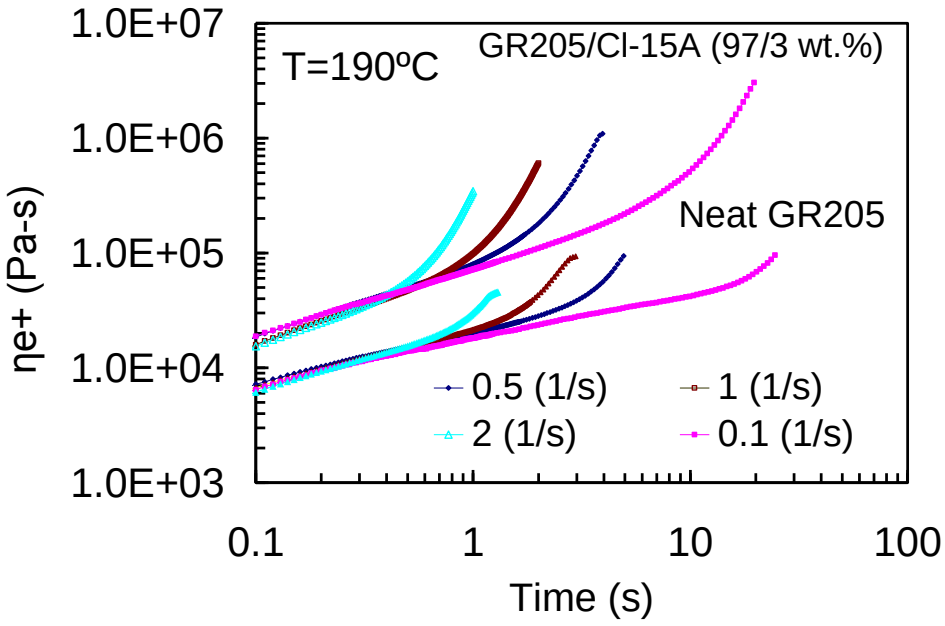

Figure 5.14: Uniaxial melt extensional viscosity of neat GR205 and GR205/Cl-15A composite tested at 190^{o}C without conditioning.

The nanocomposite of HMW-HDPE compounded on the twin screw extruder also showed similar degree of strain hardening as that of base HDPE (Figure 5.15), but at a lower test temperature of 195^{o}C. Therefore, films for the nanocomposites were produced with blow film extruder operated at 190^{o}C instead of 210^{o}C for neat HMW-HDPE. Horizontal wrinkled lines were observed on the film bubble during the film blowing operation. Table 5.2 gives the properties of the blown films made from HMW-HDPE and its nanocomposite (LD2-3) made with 5 wt. % Si-I.44P. As can be seen from the table,

the modulus of the nanocomposite film was higher than that of neat HMW-HDPE, particularly in the TD; it was twice that of unfilled HMW-HDPE. All the mechanical properties of the nanocomposite films except the moduli were poorer than that of the base HMW-HDPE films.

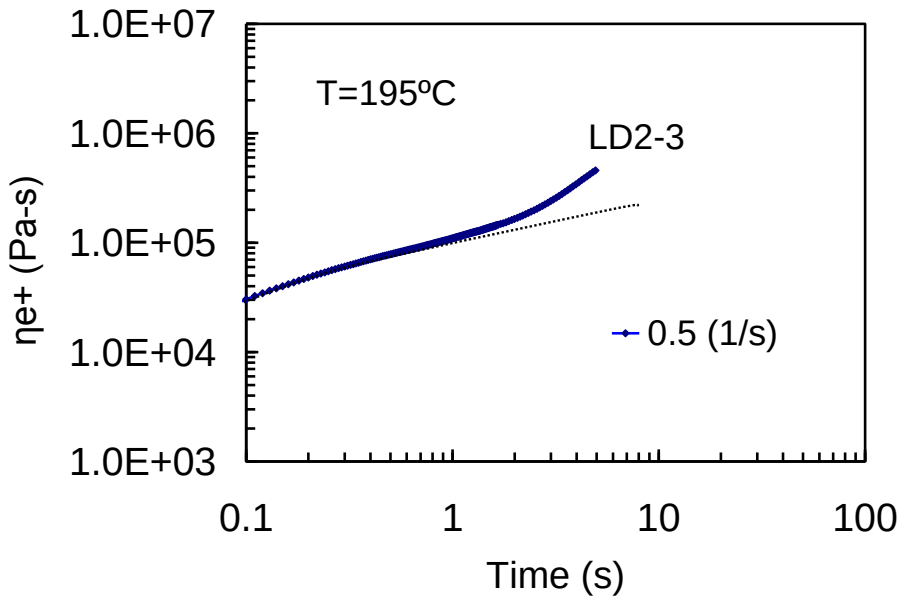

Figure 5.15: Uniaxial melt extensional viscosity of HMW-HDPE nanocomposite tested at 195^{o}C without conditioning.

Material / Property	Neat HMW-HDPE	LD2-3 Nanocomposite with 5 wt. % Si-I.44P
Film gauge (microns)	25.4	25.4
Tensile Strength-MD (MPa)	38.4	33.1
Tensile Strength-TD (MPa)	30.7	20.7
Tensile Modulus-MD (MPa)	371.6	441.9
Tensile Modulus-TD (MPa)	266.1	804.6
Elongation at break (%)	361.6	319.1
Elongation at break (%)	550.4	10.1
Tear Strength-MD (g)	16.2	7.1
Tear Strength-TD (g)	959.0	567.0

Table 5.2: Mechanical properties of blown films of HMW-HDPE and LD2-3 nanocomposite containing 5 wt. % Si-I.44P produced with a BUR of 4.5.

The fact that the films could not be blown above 190^{o}C suggested that there was too high concentration of low molecular weight components like SA, HIVAL and GR-205. Out of these, SA and GR-205 are maleated polyolefinic compatibilizers, and must be present to get good dispersion of the clay. Therefore, we decided to prepare a new masterbatch, this time without HIVAL. Additionally, we decided to reduce the final clay concentration to 3 wt. % instead of 5 wt. %. Figure 5.16 shows XRD patterns of the newly prepared masterbatch and its let-down batch with HMW-HDPE.

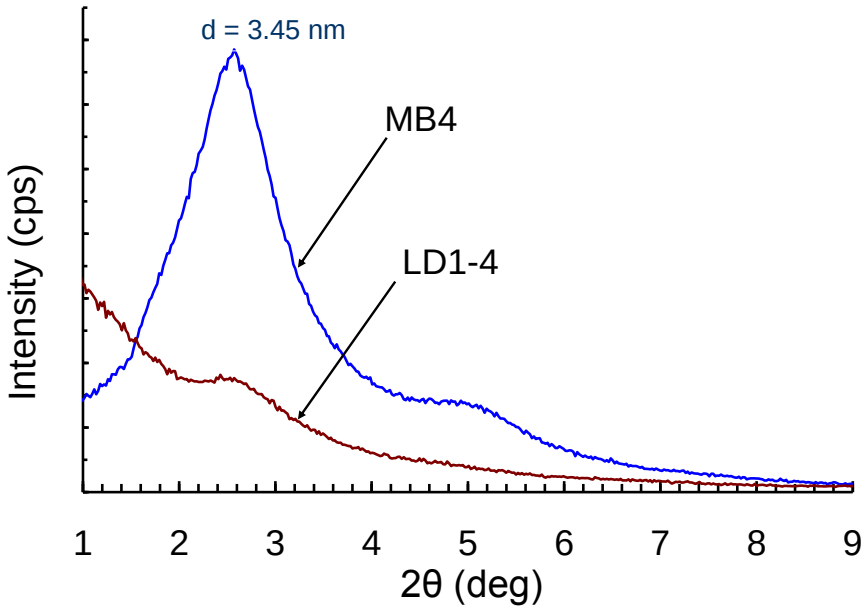

Figure 5.16: XRD patterns of MB4 with Si-I.44P/SA (50/50 wt. %) and its let-down compound LD1-4 with HMW-HDPE/GR205/MB4 (88/6/6 wt. %) prepared on Polylab OS torque rheometer.

The extensional viscosity behavior of the let-down batch is shown in Figure 5.17. As can be seen from Figure 5.14, the extensional melt viscosity of the nanocomposite with 3 wt. % Si-I.44P showed an almost similar level of strain hardening as that of neat HMW-HDPE, when both were tested at 210^{o}C. Films of these two materials were then blown at a set temperature of 210^{o}C and tested for their properties.

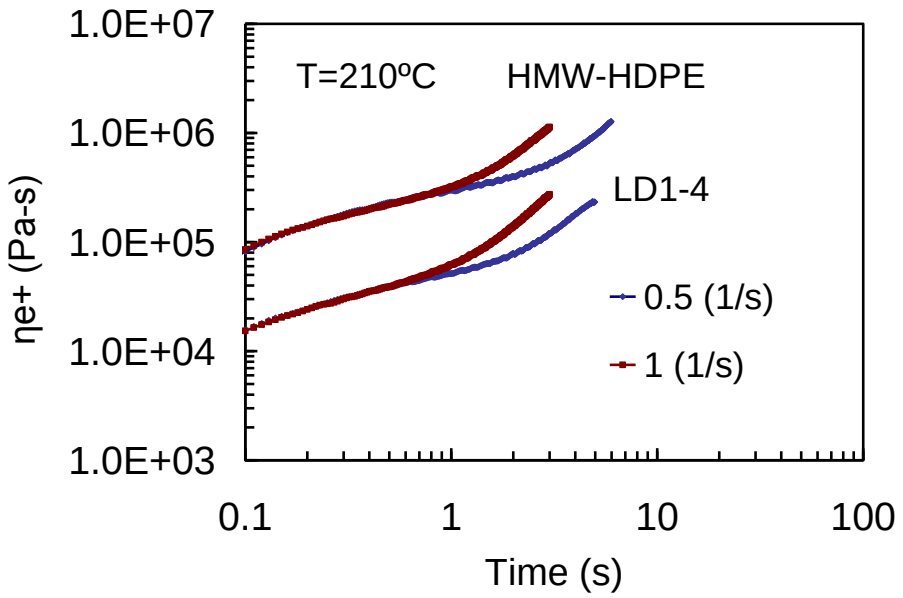

Figure 5.17: Uniaxial melt extensional viscosity behavior of HMW-HDPE and LD1-4 nanocomposite with HMW-HDPE/GR205/MB4 (88/6/6 wt. %). Both conditioned for 5 min. before testing at 210^{o}C

Table 5.3 gives the properties of the films obtained for LD1-4 and HMW-HDPE film produced under similar processing conditions. Similar to the results of nanocomposite films with 5 wt. % Si-I.44P, the nanocomposite films with 3 wt. % Si-I.44P showed poor mechanical properties, except the tensile modulus. The tensile modulus in TD this time was 8 times that of neat HMW-HDPE. The film showed comparable tear strength to that of neat polymer, but besides that all other mechanical properties were inferior to that of unfilled HDPE. From these results it appears that the anisotropic orientation of organoclay particles during biaxial orientation, in film blowing operation was the main reason for poor mechanical performance of the film in the machine direction.

Material / Property	Neat HMW-HDPE	LD1-4 Nanocomposite with 3 wt. % Si-I.44P
Film gauge (microns)	25.4	23.6
Tensile Strength-MD (MPa)	81.7	22.4
Tensile Strength-TD (MPa)	31.7	16.9
Tensile Modulus-MD (MPa)	427.5	448.1
Tensile Modulus-TD (MPa)	103.4	937.7
Elongation at break (%)	373.0	229.0
Elongation at break (%)	494.0	5.0
Tear Strength-MD (g)	11.2	11.0
Tear Strength-TD (g)	638.0	250.0

Table 5.3: Mechanical properties of blown films of HMW-HDPE and LD1-4 nanocomposite containing 3 wt. % Si-I.44P produced with a BUR of 2.5

5.5 Conclusions

Well exfoliated nanocomposites of high molecular weight HDPE were obtained by using a combination of two maleated polyethylene compatibilizers in two-stage mixing. Complete exfoliation of the nanoclay could be obtained with compatibilizer to polymer ratio of 1/7, as well as 1/10. Injection molded bars of nanocomposite with 5 wt. % aminosilane treated clay showed 19 % increase in flexural modulus. Tensile moduli of blown films of the HMW-HDPE nanocomposites with 5 wt. % and 3 wt. % of clay loadings were much higher than that of the neat polymer; however, all other properties of the nanocomposite films were poorer than that of neat HMW-HDPE processed under similar processing conditions. Orientation of the exfoliated clay particles during biaxial stretching in film blowing operation must be the cause of this.

CHAPTER 6

SUMMARY AND RECOMMENDATIONS

The research work presented in this study was conducted in two separate parts. The conclusions and recommendations for each part are given below:

Part I:

Summary:

This part of the research constituted a major portion of the work; it was focused on studying the development of microstructure in drawn PP-talc composites that were die-drawn in solid phase at elevated temperatures. Two experimental setups were used to perform the die drawing operations; a lab-scale setup and a pilot-scale setup. An injection molded billet of PP-talc composite filled with 38 wt. % or 16.5 vol. % of talc was die drawn on the lab-scale setup. The billet was drawn using a converging die of nominal draw ratio of 3.2 at 150°C, using the following 5 different draw rates: 2.54 cm/min, 12.7 cm/min, 25.4 cm/min, 50.8 cm/min and 101.6 cm/min. The required draw loads were recorded using a load cell on the drawing side. A relatively bigger extruded billet of PP-talc composite was die-drawn on the pilot-scale setup. This billet was loaded with a lower talc level (20 wt. % or 7 vol. %). Pilot-scale die drawing runs were performed at 145°C using a converging die of nominal draw ratio of 2, using the draw rates of 91 cm/min, 244 cm/min, 366 cm/min and 573 cm/min. The microstructures of the die drawn samples were analyzed for voiding and crystal orientation.

To study the void fractions and void morphologies, composites drawn on both the lab-scale and pilot-scale die drawing setups were analyzed. The densities (or void contents) were determined using a densitometer, and the void morphologies were characterized

with the help of a scanning electron microscope (SEM). The dimensions of the particles and voids seen on the SEM pictures were quantified using image analysis software. From the recorded values of die drawing loads, it was concluded that the draw stress required for die-drawing PP-talc composite was considerably less than that required for die-drawing the corresponding unfilled PP. The draw stress was found to increase linearly with the draw ratio. From the measurements of densities and dimensions of the drawn samples, it was noted that the die drawing operations on both of the setups led to saturation in the final density, above an actual draw ratio of 7. The final void volume fractions in the die drawn samples of PP-talc-38 wt. % and PP-talc-20 wt. % composites were 30 % and 17 %, respectively. The ratio of final void volume fraction to the initial filler volume fraction was found to be lower (1.81 vs. 2.26) for the die-drawn composite with higher talc loading. Morphological pictures showed that all the particles in the final deformation zones were debonded from the matrix phase and that the voids around them had grown in the drawing direction. In the case of die-drawn PP-talc-20 wt. % composite, the lengths of the voids along the drawing direction were 4-6 times the lengths of the particles trapped inside of them. The average value of the void stretch ratio (ratio of the void length to the particle length in the drawing direction) plateaued above an actual DR of 7. Voids formed in the die-drawn composite with the higher talc loading were observed to have a lower range of aspect ratios and a wider distribution of stretch ratios.

To characterize the crystal orientations, samples of billets that were die-drawn mainly on the pilot-scale setup were analyzed; lower concentration of the talc particles in these billets allowed greater accuracy in the experimental results. The texture of the samples was characterized using a wide angle X-ray diffraction (XRD) technique. The crystalline

fractions in the undrawn and die drawn billet samples were determined using a differential scanning calorimeter (DSC). To study the effect of draw rate on the final texture, the billet samples (obtained with different draw rates) collected farther from the die exit were analyzed. To understand the development of the texture at a given draw rate, billet samples collected from the die-deformation zone and the post-die deformation zone were analyzed. The texture developed in the die-drawn PP-talc composite was compared to that of die-drawn neat PP, which was drawn under a similar set of processing conditions. For both of the materials, the processes of annealing and subsequent die drawing were found to have imparted a 12 to 15 % increase in the crystallinity of the matrix phase. Analyses of the DSC endotherms and the 2θ linear XRD patterns indicated that the die drawing operation resulted in the transformation of the thermally less stable crystalline phase (mesophase) in the undrawn materials, to a thermally stable crystalline phase with folded-chain α crystals. The pole figure study suggested the presence of radially oriented crystal structures in undrawn PP-talc composite. These crystal structures resembled the spherulitic domains found in unfilled PP, but with a different nucleation direction. The flaky talc particles in the composite material must have forced the crystals to grow in a different direction than that of neat PP. The differences in the initial morphologies of the undrawn materials resulted in different modes of texture development on die drawing. In the die deformation zone, the composite was found to have yielded at a lower draw ratio than the neat PP. In the post-die deformation zone, (110)[001] and (010)[001] type texture elements developed in both the materials; the draw ratio at which that happened was higher for the drawn PP-talc composite. Quantification of those texture elements indicated that the ratio of (010)[001] to

(110)[001] was always higher for the drawn composite. The texture elements in both the materials sharpened with draw ratio, but the degree of crystalline c-axis orientation attained in the case of die-drawn composite was lower than that of die-drawn neat PP of comparable draw ratio. The phenomena of particle debonding and void growth occurring during composite drawing would have reduced the effective stress available for the molecular orientation of the matrix phase. Despite the saturation in the crystal orientation, crystal volume fraction and void growth in the case of drawn composite, the tensile modulus of the drawn materials increased with DR_{final} (obtained using increasing values of draw rates).

Recommendations:

During the drawing operation of a given composite, the inter-particle distance which is determined by the filler volume fraction affects the stress-strain distribution around the individual particles. The results obtained on the void content and void morphology in our study seem to be in logical agreement with some of the important observations reported in the literature. For example, Renner et al.[12] observed that the difference between the debonding stress and the yield stress during tensile drawing of microcomposites decreased with increased filler volume fraction. Therefore, the fraction of the particles debonded during composite drawing is expected to be higher for lower levels of filler loadings. In another study, Dubnikova and coworkers[13] observed that the voids formed around the debonded particles in PP composite filled with 8 vol. % of $Al(OH)_3$ were longer, as compared to those formed in PP composite that was filled with 36 vol.% of $Al(OH)_3$. The relative extents of debonding and void growth responsible for density

reduction are expected to be higher when the composite is filled with lower loadings of micron sized filler particles. This must be the reason, why the ratio of the void volume fraction to the particle volume fraction, was higher in the case of die-drawn PP-talc-20 wt. % composite, compared to the die-drawn PP-talc-38 wt. % composite. This conclusion needs to be validated by conducting additional runs using a same die-drawing set-up and similar processing conditions.

The results on the crystal orientation and texture of the die-drawn materials were obtained by studying the billet samples after the die-drawing runs were over. Therefore, the crystal texture developed in a given material shows a combined effect of the orientation process as well as the cooling profile. Unless the two effects are decoupled, there is no way to tell which one has more influence on the texture. To characterize this, an in-situ study of the crystal orientation needs to be performed.

Part II:

Summary:

The second part of the research work was directed towards developing nanocomposites of high molecular weight high density polyethylene (HMW-HDPE), with enhanced mechanical properties and improved or similar processability as that of the base resin. The very high molecular weight of the matrix presents many challenges in attaining a good dispersion of the organoclay during its melt mixing. In this work, we optimized the material and processing parameters to obtain well-dispersed nanocomposite of HMW-HDPE. The various ingredients used to prepare the nanocomposites were: the bulk polymer (HMW-HDPE), another grade of HDPE with a lower molecular weight, nanoclays treated with three different organic treatments, two grades of maleated PE

compatibilizers, and one commercially available clay-masterbatch. Prior to the compounding, the organically treated nanoclays, as well the PE-g-MA compatibilizers were dried under vacuum. Compounds with various levels of clay, compatibilizer and base polymer were prepared by melt mixing, either in a single stage or in a two-stage process. In a single stage mixing, all of the components: bulk polymer, organoclay, and compatibilizer were added at once. Two-stage mixing involved preparation of a masterbatch with a high loading of clay. Temperature control was critical during mixing, as the very high viscosity of the HMW-HDPE led to an increase in the melt temperature. The chunks of compound obtained after melt-mixing were molded to prepare samples for X-ray diffraction (XRD) and rheological studies. In order to obtain flexural bars and film samples, chunks of melt mixed compounds were granulated in a mini granulator prior to melt processing. The nanocomposites of HMW-HDPE and unfilled HMW-HDPE were characterized for their XRD patterns, extensional melt flows and flexural properties. Selective formulations of nanocomposites were pelletized and melt-processed to obtain blown-film samples. The film samples were tested for their tensile properties and tear strengths in the machine direction and the transverse direction.

Complete exfoliation of the dispersed clay was possible with a combination of two maleated polyethylene compatibilizers in two-stage mixing. Compatibilizer to polymer ratios as low as 1/7 to 1/10 were enough to get well-dispersed clay-nanocomposites. Two exfoliated nanocomposite formulations with 3 and 5 wt. % of organoclay were chosen for the film blowing operation. Flexural bars of the latter composite showed a modulus increase of 19 %. Both the nanocomposites showed a good dispersion of the organoclay and exhibited strain hardening behavior in the melt state. Tensile moduli of the blown

films obtained with the two nanocomposites were much higher than that of the neat polymer-particularly in the transverse direction. However, the percent elongations, tensile strengths and tear strengths of the nanocomposite films were poorer than that of the neat HMW-HDPE processed under similar processing conditions. Improved mechanical properties in the case of injection molded flexural bars, and the inferior mechanical properties in the case of blown-film samples indicated that the processing conditions had affected the final properties of the processed samples. Higher tensile moduli of the film samples in the transverse direction indicated anisotropic orientation of the exfoliated clay particles during the biaxial stretching of the blown film.

Recommendations:

Some of the suggestions given below may be useful to achieve improved film blowing ability of the nanocomposites:

Extensive work done by Chaudhari et al. [98, 99] indicates that a nanocomposite of PP can show noticeable improvement in the strain-hardening ability in the extensional melt flow, even when it is intercalated; complete exfoliation of the organoclay is not necessary. One likely reason for this observation is that the polymer chains crystallized inside the clay galleries can melt and provide high degree of entanglement density, thus imparting an increased strain-hardening ability to the melt. If the clay is exfoliated, the crystals would be relatively separate from each other and might not yield higher entanglement density on melting. With this argument, another recommendation in the context of our study is to make an intercalated nanocomposite, probably using less intense mixing conditions or using lower concentrations of the compatibilizers, and use this nanocomposite for the

film-blowing operation. The film blowing operation of the nanocomposite, in the melt state itself, might lead to further separation of the clay platelets.

The aminosilane treatment used to obtain silylated organoclay in our work contained three hydrolysable groups attached to the silicone atom. During the silylation of the I.44P clay, these groups might have self-condensed inside the clay galleries, giving a broader XRD peak. This type of self-condensation can not only make the dispersion difficult during the melt mixing stage, but can also create weak spots in the stretched film during film blowing stage. One way to avoid this would be to use an aminosilane that contains either one, or at the most two hydrolysable groups attached to the silicon atom.

APPENDICES

APPENDIX A

Figure A.1 and Figure A.2 show the area ratios of die drawn PP-talc-38 wt. % and die drawn PP-talc-20 wt. % composite respectively. As these figures show despite the lower nominal draw ratio of the die, the area ratios attained for the PP-talc composite drawn on pilot die drawing setup were higher than the composite drawn on lab-scale setup. Other than the higher draw rates, the longer post-die deformation zone imposed by unconstrained drawing of the material through a converging die without any die-land were the main reasons for the observed differences. The values of area ratios for the two drawn materials were used to calculate their respective draw ratios which are presented in Figure 3.6 and Figure 3.7. Additional microscopic images of PP-talc-20 wt. % composite drawn at different draw rates are shown in Figures A.3 to A.6. Part (a) in these figures show SEM pictures viewed in MD-ND plane, at all the draw rates, the particle in this plane were found to be well trapped inside the voids. Part (b) show the images viewed in MD-TD plane. Unlike the samples cracked for MD-ND view the particles in this plane were not entirely confined inside the voids and thy came off during the surface preparation. Some of these pictures (presented here) still showed a good beat of particle entrapment even in this plane. Based on these observations it was assumed that the dimensions of a void in ND-TD plane were similar to that of particle dimensions trapped inside it and the voids were stretched mainly in the MD. The particle lengths for >1800 particles (measured for all the draw rates) are presented in Figure A.7 and Figure A.8. As expected, in both the MD-ND and MD-TD views the lengths of particles in MD were close to each other. The number average particle dimension was found to be 37 x 14 x 7.5 (μm^3).

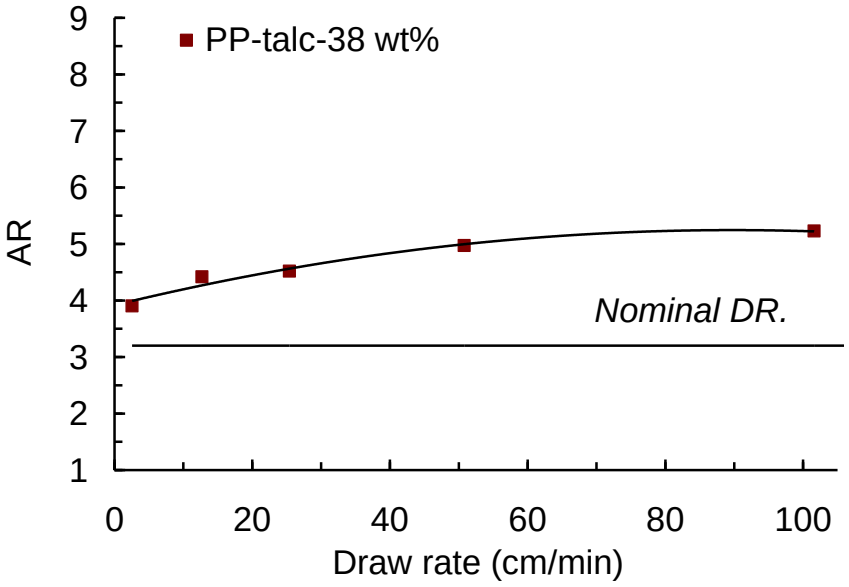

Figure A.1: Area ratio of PP-talc-38 wt. % drawn on a lab-scale setup.

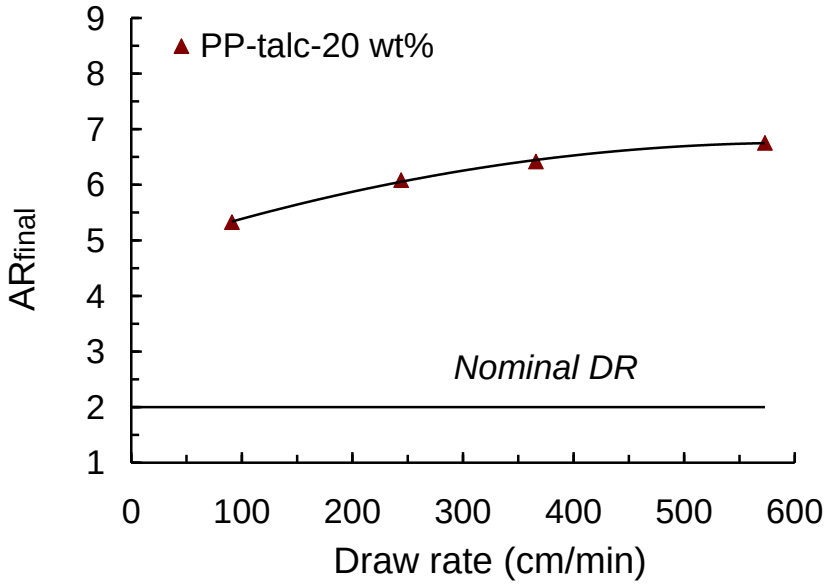

Figure A.2: Area ratio of PP-talc-20 wt. % drawn on a pilot-scale setup.

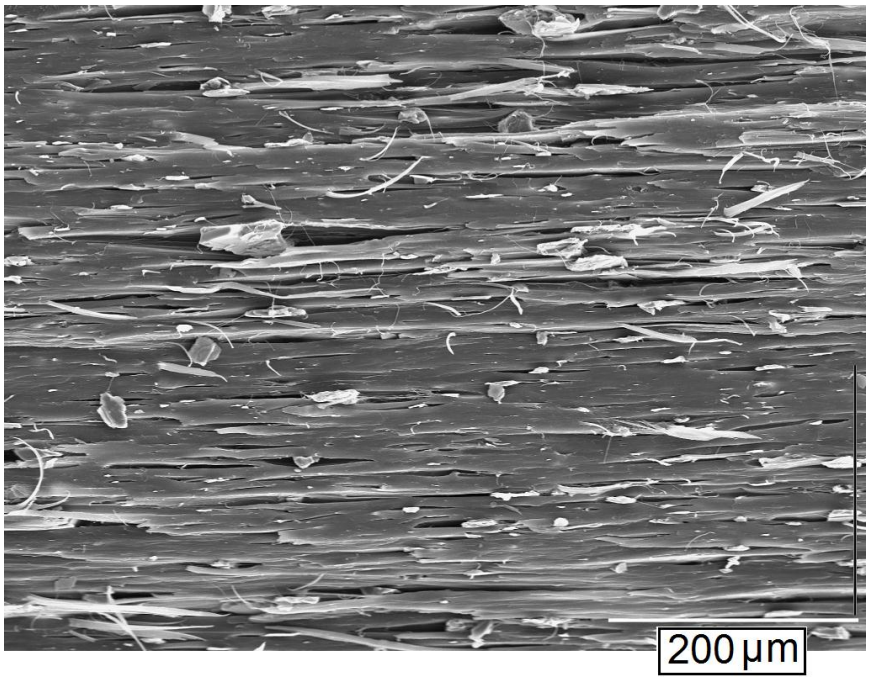

(a)

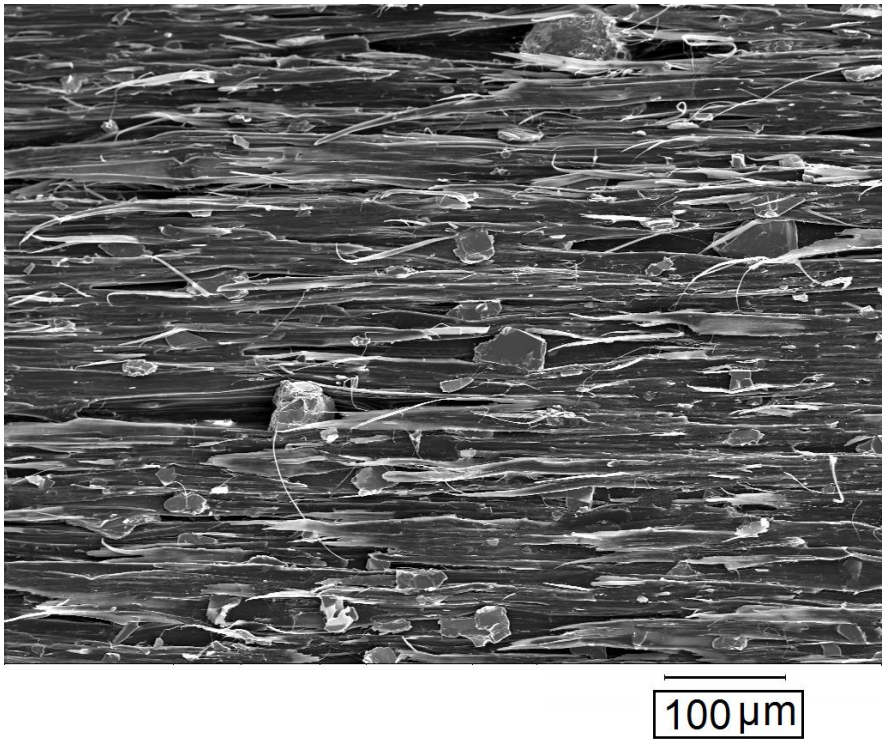

(b)

Figure A.3: SEM images of PP-talc-20 wt. % composite die drawn at 91 cm/min (a) MD-ND plane (scale bar =200 µm) and (b) MD-TD plane (scale bar =100 µm)

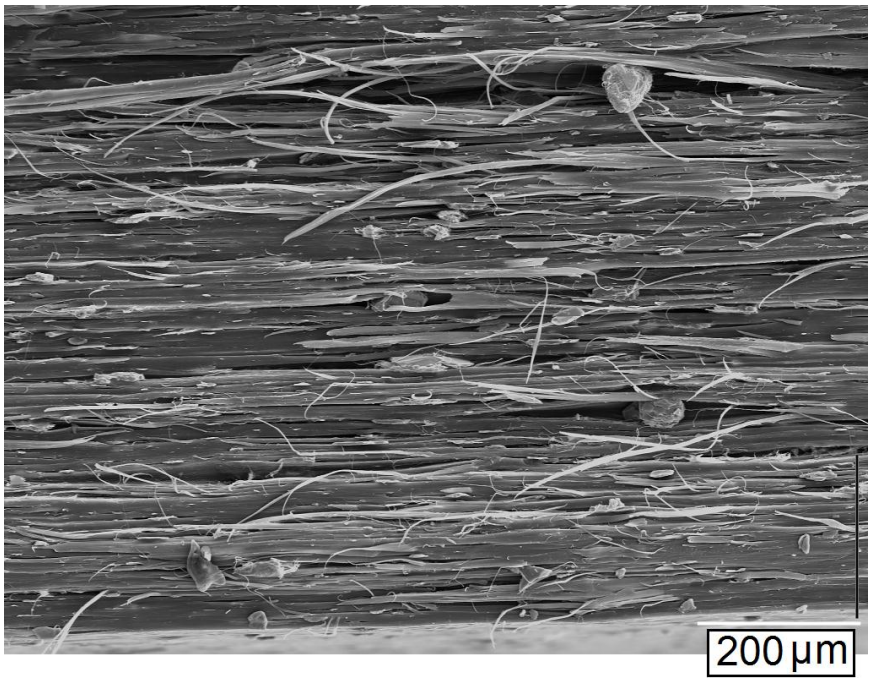

(a)

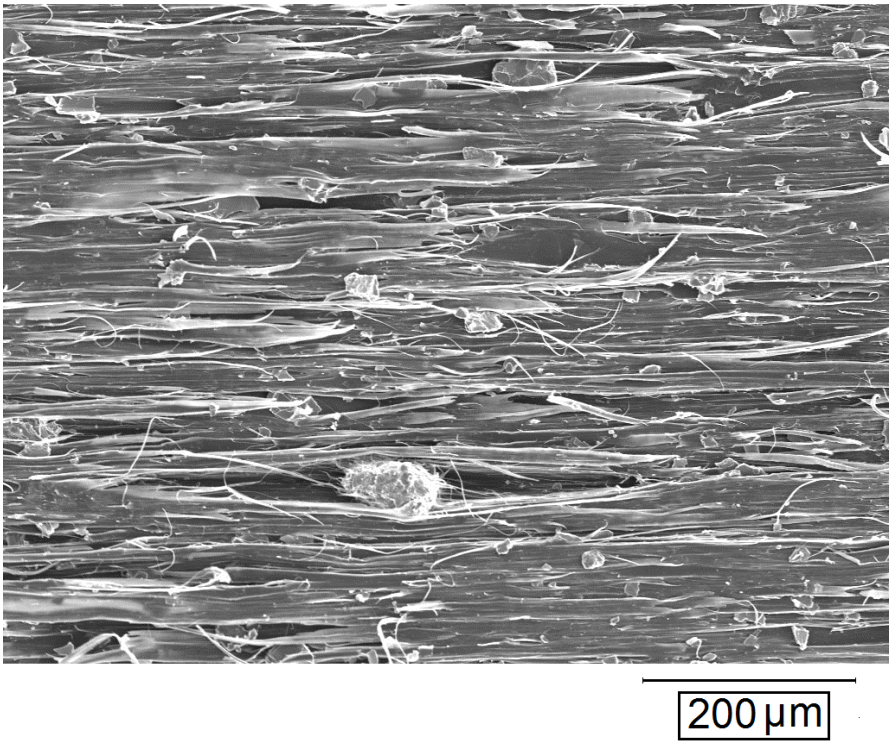

(b)

Figure A.4: SEM images of PP-talc-20 wt. % composite die drawn at 244 cm/min (a) MD-ND plane (scale bar =200 µm) and (b) MD-TD plane (scale bar =200 µm)

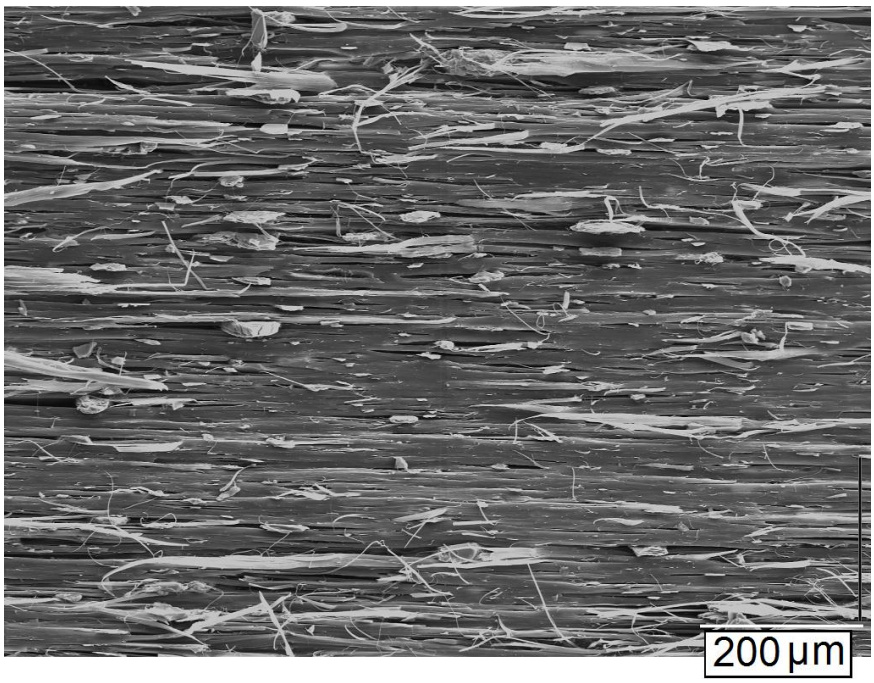

(a)

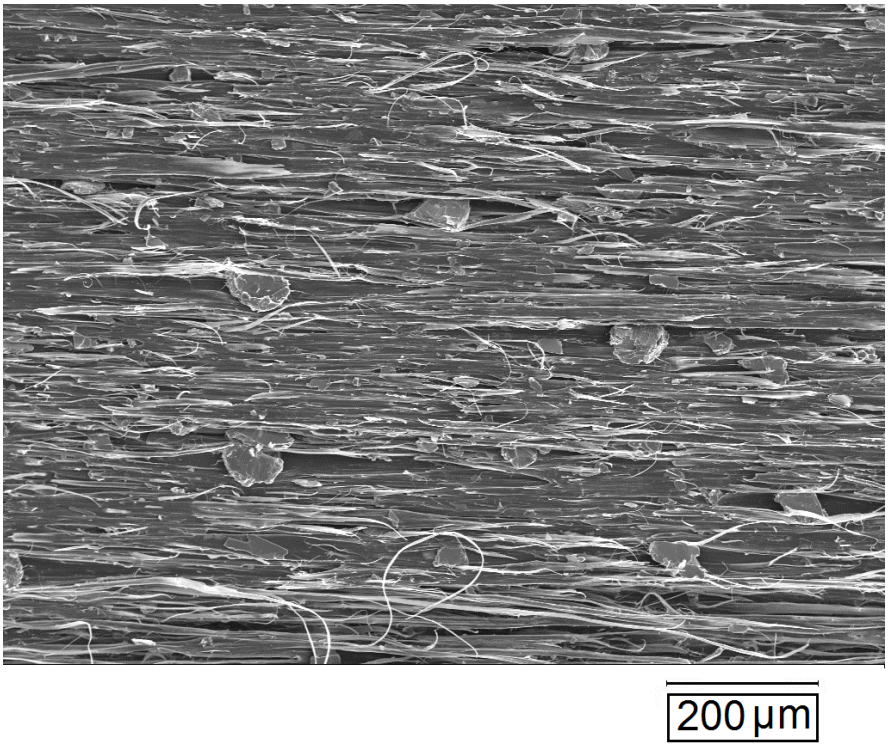

(b)

Figure A.5: SEM images of PP-talc-20 wt. % composite die drawn at 366 cm/min (a) MD-ND plane (scale bar =200 µm) and (b) MD-TD plane (scale bar =200 µm).

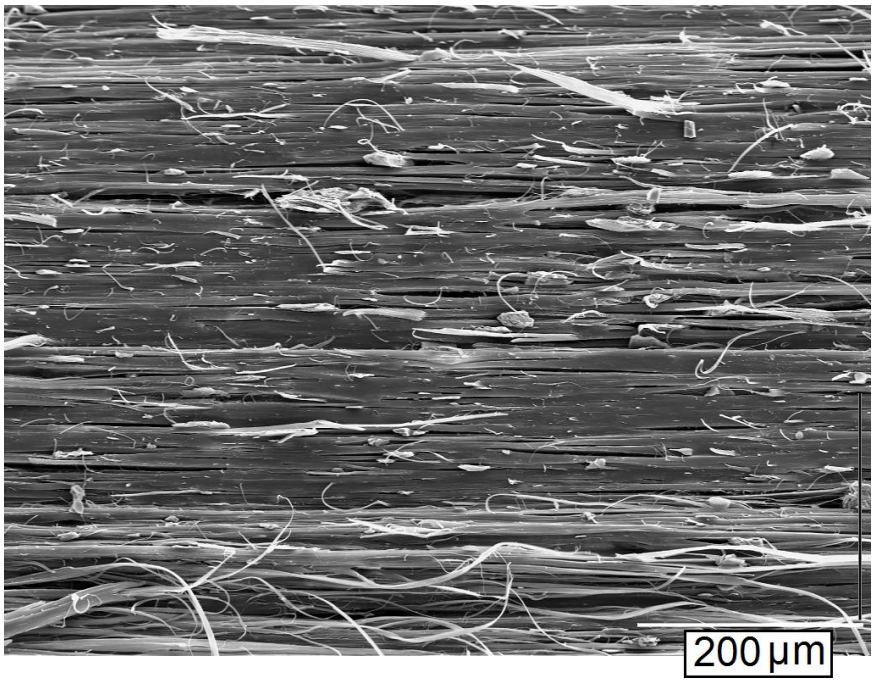

(a)

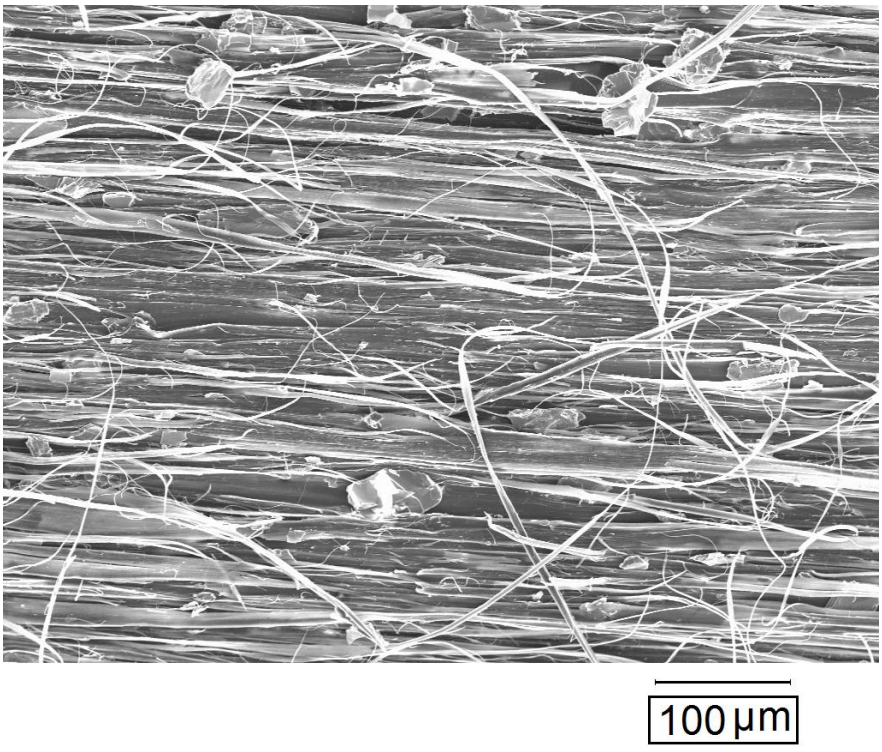

(b)

Figure A.6: SEM images of PP-talc-20 wt. % composite die drawn at 573 cm/min (a) MD-ND plane (scale bar =200 µm) and (b) MD-TD plane (scale bar =100 µm).

APPENDIX B

For die-drawn samples obtained from lab-scale die drawing runs cuboidal specimens of 15 x 10 x 2.4 mm^3 dimensions were cut and machined for XRD studies. Here, 10 mm and 2.4 mm are the final dimensions of the composite billet drawn at the highest draw rate along the TD and ND respectively. Experimental setup for the rectangular sections of lab-scale drawn billets is shown in Figure B.1.

The XRD pattern of undrawn PP-talc-38 wt. % composite is shown in Figure B.2 along with the XRD pattern for the talc (FDC).

The orientation of the crystalline c-axis in PP can be calculated from the pole figures of α(110) and α(040) crystal planes of PP. The averaged values of the orientation distributions of these planes $\cos^2 \varphi_{(hkl)}$ in each MD, TD and TD are computed with the help of three dimensional coordinate system shown in Figure B.3 and using the following formulae[80, 92]:

$$\left\langle \cos^2 \phi_M \right\rangle = \frac{\int_0^{2\pi} \int_0^{\pi/2} I(\varphi, \chi) \cos^2 \varphi \sin^3 \chi \, d\phi \, d\chi}{\int_0^{2\pi} \int_0^{\pi/2} I(\varphi, \chi) \sin \chi \, d\phi \, d\chi} \qquad \text{(B.2)}$$

$$\left\langle \cos^2 \phi_T \right\rangle = \frac{\int_0^{2\pi} \int_0^{\pi/2} I(\varphi,\chi) \sin^2 \varphi \sin^3 \chi \, d\phi \, d\chi}{\int_0^{2\pi} \int_0^{\pi/2} I(\varphi,\chi) \sin \chi \, d\phi \, d\chi} \qquad \text{(B.3)}$$

$$\left\langle \cos^2 \phi_N \right\rangle = \frac{\int_0^{2\pi} \int_0^{\pi/2} I(\varphi,\chi) \cos^2 \chi \sin \chi \, d\phi \, d\chi}{\int_0^{2\pi} \int_0^{\pi/2} I(\varphi,\chi) \sin \chi \, d\phi \, d\chi} \qquad \text{(B.4)}$$

The average $\langle \cos^2 \varphi_c \rangle$ in the machine direction is then calculated using Wilchinsky's relation[80] as given in Eq. (B.5) derived from the unit cell geometry of α-PP crystal.

$$\left\langle \cos^2 \varphi_{c,i} \right\rangle = 1 - 1.099 \left\langle \cos^2 \varphi_{(110),i} \right\rangle - 0.901 \left\langle \cos^2 \varphi_{(040)i} \right\rangle \qquad \text{(B.5)}$$

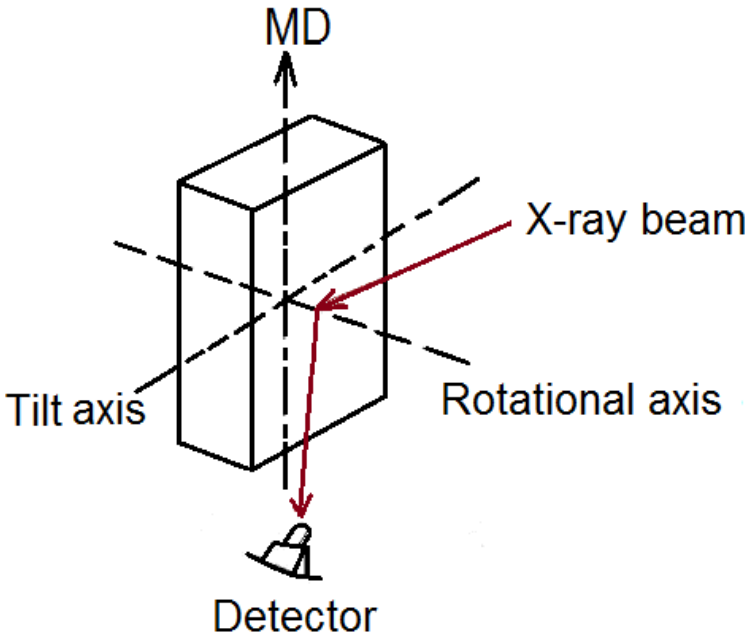

Figure B.1: Schematic of experimental setup used to study XRD of PP-talc-38 wt. % composite drawn on lab-scale setup.

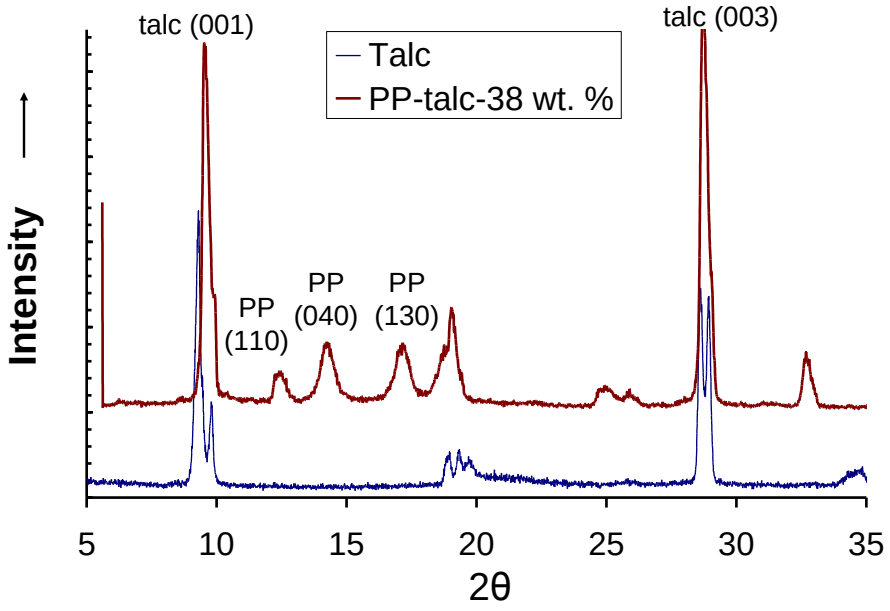

Figure B.2: XRD patterns of PP-talc-38 wt. % composite and the Luzenac talc.

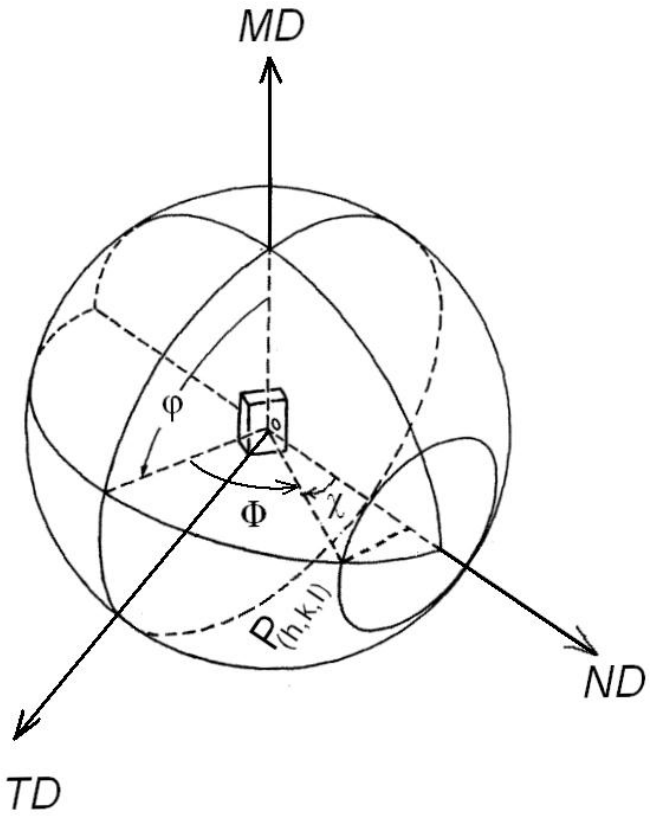

Figure B.3: Position of plane normal $P_{(h,k,l)}$ by spherical coordinates χ and φ.

REFERENCES

REFERENCES

1. D. M. Bigg, Polymer Engg. & Sci., **28**(13), 830 (1988).

2. P. Smith and P. J. Lemstra, J. of Mat. Sci., **15**, 505 (1980).

3. A. Cifferri and I. M. Ward, ed., Ultra High Modulus Polymers, Applied Science Publishers Ltd, 1, (1979).

4. I. M. Ward, P. D. Coates and M. M. Dumoulin, Solid Phase Processing of Polymers, Hanser Publishers, Munich (2000).

5. I. M. Ward, J. Sweeeney, ed., An Introduction to the Mechanical Properties of Solid Polymers, John Wiley and Sons Ltd, 2, (2004).

6. J. M. Andrews and I. M. Ward, J.Appl.Polym.Sci.,**14,** 2305 (1970).

7. K. L. Nichols and B. M. Birchmeier, I. M. Ward, P. D. Coates, P. Caton-Rose, Thompson, P. Glen, V. Wani and R. M. Patel, U.S. Patent Application US20080287576 A1, May 14, 2007.

8. K. L. Nichols and B. M. Birchmeier, U.S. Patent Application US20080111278 A1, October 15, 2007.

9. W.R. Newson and F.W. Maine, Proceedings of Conference on Progress in Wood Fiber-Plastic Composites, Toronto, CA, (2002).

10. P. S. Hope, A. Richardson and I. M. Ward, *Journal of Applied Polymer Science.* **26**, 2879 (1981).

11. B. Pukanszky, M. Vanes, H. Maurer and G. Voros, *Journal of Material Science* **29,** 2350 (1994).

12. K. Renner, M. Yang, J. Moczo, H. Choi and B. Pukanszky, *European Polymer Journal*, **41**, 2520 (2005).

13. I. L. Dubnikova, D. K. Muravin and G. Oshmyan, *Polymer Engineering and Science*, **37**(8), 1301 (1997).

14. M. Jerabek, Z. Major, K. Renner, J. Moczo, B. Pukanszky and R.W. Lang, *Polymer*, **51**, 2040 (2010).

15. R. Farris, *Transactions of The Society of Rheology* **12:2,** 315 (1968).

16. P. Vollenberg, D. Heikens and H.C.B. Ladan, *Polymer Composites*, **9**, 382 (1988).

17. A. N. Gent and B. Park, *Journal of Material Science* **19** 1947(1984).

18. M. E. J. Dekkers and D. Heikens, *Journal of Material Science* **18** 3281(1983).

19. V. G. Oshmyan and D.K. Muravin, *Composite Sci. & Tech.*, **57**, 1167 (1997).

20. V. G. Oshmyan, S. A. Timan and M.Yu Shamaev, *Polymer Science*, Ser.A, **47**, 352 (2005).

21. A. Meddad, S. Fellahi, M. Pinard and B. Fisa, *SPE ANTEC Tech. Papers*, **40** 2284 (1994).

22. A. Meddad and B. Fisa *J. of Applied Polymer Science* **64** 653 (1996).

23. B. A. Sjogren and L. A. Berglund, *Polymer Composites* **18** 1(1997).

24. B. Z. Jang, D. R. Uhlmann and J. B. Vander Sande, *J. of App. Pol. Sci.*, **30**, 2485, (1985).

25. A. Zhuk, N.Knunyants, V. Oshmyan, V. Topolkaraev and A. Berlin *Journal of Material Science* **28**,4595 (1993).

26. D. R. Morrow, *J. Macromol. Sci.-Phy.*, **B3**(1), 53 (1969).

27. S. Brcukner, S. Meille, V. Petraccone and B. Pirozzi, *Prog. Polym. Sci*., **16**, 361 (1991).

28. H. W. Wyckoff, *J. of Polym. Sci.*, **62**, 83 (1962).

29. W. W. Cox, A. A. Duswalt, *Polymer Engineering and Sci.*, 309 (1967).

30. W. J. Choi, S. C. Kim, *Polymer* **45**, 2393 (2004).

31. Y. Song, K. Nitta, N. Nemoto, *Macromolecules* 36, 1955 (2003).

32. Y. Nozue, Y. Shinohara, Y. Ogawa, T. Sakurai, H. Hori and T. Kasahara, *Macromolecules* **40**,2036 (2007).

33. T. Sakurai, Y. Nozue, T. Kasahara, K. Mizunuma, N. Yamaguchi and K. Tashiro, *Polymer*, **46**, 8846 (2005).

34. Y. Koike, and M. Cakmak, *Macromolecules*, **37**, 2171 (2004).

35. J. X. Li, W. L. Cheung and C. M. Chan, Polymer, **40**, 2089 (1999).

36. M. Aboulfaraj, C. G'Sell, B. Ulrich and A. Dahoun, *Polymer*, **36**, 731 (1995).

37. P. D. Coates, I. M. Ward, *Polymer Engg. & Sci.* **21**(10), 612 (1981).

38. P. S. Hope, A. Richordson and I. M. Ward, *Polymer Engg. & Sci.*, **22**(5), 307 (1982).

39. S. N. Kukureka, G. Craggs and I. M. Ward, J. *of Material Science*, 27, 3379 (1992).

40. A. G. Gibson, G. R. Davies and I. M. Ward, *Polymer* **19** 683(1978).

41. J. Mohanraj, M. Bonner, D. Barton and I. Ward, *Journal of Process Mechanical Engineering* **221** Part **E** 47(2006).

42. N. G. McCrum, C. P. Buckley and C. Bucknall, ed., "Principles of Polymer Engineering", 2nd Ed, 45, (1997).

43. S. Rettenberger, L. Capt, H. Munstedt, K. Sttoperka and J. Sanze, *Rheol Acta*,**41**,332 (2002).

44. F. Zuo, J. K. Keum, X. Chen, B. S. Hsio, H. Chen, S. Y. Lai, R. Wevers and J. Li, *Polymer*, **48**, 6867 (2007).

45. I. Polec, P. J. Hine, M. J. Bonner, I. M. Ward and D.C. Barton, *Comp. Sci. & Tech.*, **70**, 45, (2010).

46. C. Chaffey, A. Taraiya and I. M. Ward, *Polym. Eng. And Sci.* **37**, 1774 (1997).

47. Z. Bartczak and E. Martuscelli, *Polymer* **38** (16),4139 (1997).

48. M. Pluta, Z. Bartczak and A. Galeski, *Polymer* **41**, 2271 (2000).

49. F. Sadeghi, A. Ajji and P. J. Carreau, *J. Plastic Fim & Sheeting*, **21**,1 (2005).

50. P. Zhu, J. Tung, A. Phillips and G. Edward, *Macromol.* **39**, 1821, (2006).

51. G. Machado, E.L.G. Denardin, E.J. Kinast, M.C. Gonclaves, M.A. de Luca, S.R. Teixeira and D. Samios, *European Polymer Journal*, **41**, 129 (2005).

52. M. Fujiyama and T. Wakino, *J. Appl. Polym. Sci.* **42**, 9, (1991).

53. M. C. Branciofti, C.A. Oliveira and J.A. de Sousa, *Polymer Advanced Technology* (2009).

54. E. Ferrage, F. Martin, A. Boudet, S. Petit, G. Fourty, F. Jouffret, P. Micoud, P.De Parseval, S. Salvi, C. Bourgrette, J. Ferret, Y. Saint-Gerard, S. Buratto and J.P. Fortune, *J. of Mat. Sci.*, **37**, 1561 (2002).

55. M. Naiki, Y. Fukui, T. Matsumura, T. Nomura and M. Matsuda, *J. Appl. Polym. Sci.* **79**,1693 (2001).

56. T. Kitayama, S. Utsumi, H. Hamada and T. Nishino, T. Kikutani and H. Ito, J. App. Poly. Sci., **88**(13), 2875 (2003).

57. T. Lan, P. D. Kaviratna and T. J. Pinnavaia, Chem. Mater., **7**(11), 2144 (1995).

58. K. Jayaraman, T. J. Pathak, and A. K. Chaudhary, US Patent Application 12/780,461 (2010) pub. no. 2010-0310802 A1.

59. S. Matthies, H.R. Wenk and G.W. Vinel, *J. Appl. Cryst.* **21**, 285 (1988).

60. A.-H.I. Mourad, N. Bekheet, A. El-Buthc, L. Abdel-Latif, D. Nafee and D.C. Barton, *Polymer Testing*, **24**, 169, (2005).

61. M. Arroyo, M. A. Lopez-Manchado, *Polymer*, **38**, 5587 (1997).

62. J. Amoedo and D. Lee, *Pol. Engg. & Sci.*, **32** (16), 1055 (1992).

63. A. Dasari, S. Sarang and R. D. K. Misra, *Mat. Sci. and Engg.* **A368**, 191 (2004).

64. S. Rettenberger, L. Capt, H. Munstedt, K. Stopperka and J. Sanze, *Rheol Acta*, **41**, 332 (2002).

65. A. K .Taraiya, A. Richardson and I.M. Ward, *J.Appl. Pol. Sci.*, **33**, 2559 (1987).

66. X. Yu, H, Wu, J. Li, S. Guo and J. Qiu, *Poly. Engg. & Sci.*, **49**(4), 703 (2009).

67. K. M. H. Shipley, 'High Temperature Behavior of Polypropylene and Polypropylene/glass Composites', M.S., Michigan State University, 70 (2011).

68. A. Drozdov, and Christiansen, *Polymer*, **43**, 4745 (2002).

69. A. Sudar and others, *Express Polymer Letters*, **1**, 763 (2007).

70. V. Chacko, R. Farris and F. Karasz, *J. of Applied Polymer Science* **28,** 2701 (1983).

71. P. H. Hardling and others, *J. of Adheshion Sci. and Tech.*, **12**, 497 (1998).

72. S. L. Bai and others, *J. of Mat. Sci. Letters*, **19**, 1587 (2000).

73. K. Jenckel, E. Tcege and W. Hinrichs, *Kolloid-Z,* **129**, 19 (1952)

74. H. Quan, Z. M. Li and M. B. Yang and R. Huang, *Comp. Sci. and Tech.*, **65**, 999 (2005).

75. A. Funaki, T. Kanai, Y. Saito and T. Yamada, *Poly. Engg. & Sci.*, **51** (6), 1068 (2010).

76. S. Rastogi, D. R. Lippits, W. Gerrit, M. Peters, R. Graf, Y. Yao and H. Spiess, *Nature Materials*, **4**, 635 (2005).

77. G. Coulon, G. Castelein and C.G'Sell, *Polymer* **40**, 95 (1998).

78. A. Pawlak and A. Galeski, *J. of Polymer Sci.*, Part B: *Polymer Physics* **48**, 1271 (2010).

79. T. A. Huy, R. Adhikari, T. Lupke, S. Henning and G. H. Michler, *J. of Polymer Science: Part B: Polymer Physics*, **42**, 4478 (2004).

80. Z. W. Wilchinsky, *J. of Applied Physics*, **31**(11), 1969 (1960).

81. C. L. Choy, F. C. Chen and W. H. Luk , *J of Poly. Sci.* **18**(4), 1187, (1980).

82. K.Nitta, K.Odaka, *Polymer* **50**, 4080 (2009).

83. P. B. McAllister, T. J. Carter and R. M. Hinde, *J. of Pol. Sci., Pol. Physics*, **16**, 49 (1978).

84. Z. Ma, C. Shao, X. Wang, B. Zhao, X. Li, H. An, T. Yan, Z. Li and L. Li, *Polymer*, **50**, 2706 (2009).

85. S. Bruckner, S. V. Meille, V. Petraccone and B. Pirozzi, *Prog. Poly. Sci.*, **16**, 361 (1991).

86. C. De Rosa, G. Guerra, R. Napolitano, V. Petraccone and B. Pirozzi, Eur. Pol. J., 20(10), 937 (1984).

87. G. Guerra, J. of Polymer Sci., *Pol. Phy.* Ed., 22, 1029 (1984).

88. V. Vittoria, *J. of Macromol. Sci.-Phys.*, **B28**(1), 97 (1989).

89. Y. Obata, T. Sumitomo and T. Ijitsu, *Poly. Engg. & Sci.*, **41**(3), 408 (2001).

90. Z. Bartczak, A. Galeski, *Polymer*, **40**, 3677 (1999).

91. J. Jia, D. Raabe, *European Polymer J*., **42**, 1755 (2006).

92. I. Karacan, A.K. Taraiya, D. I. Bower and I. M. Ward, *Polymer*, **34**, 2691 (1993).

93. S. Tabatabaei, P. J. Carreau and A. Ajji, Polymer, **50**, 4228 (2009).

94. M. W. Spencer, L. Cui, L, Y. Yoo, Y and D. R. Paul, *Polymer* **51,** 1056-1070 (2010).

95. J. Stange and H. Munstedt, *J. of Cellular Plastics*, **42**(6), 445 (2006).

96. H. Munstedt, S. Kurzbeck and J. Stange, *Poly. Engg. & Sci.*, **46**(9), 1190 (2006).

97. F. J. Stadler, A. Nishioka, J. Stange, K. Koyama and H. Munstedt, *Rheologica Acta*, 46(7), 1003 (2007).

98. A. K. Chaudhary and K. Jayaraman, *Polym. Eng. Sci.* **51** (9), 1749-1756 (2011).

99. A. K. Chaudhary, 'Rheology Modification and Foaming of Polypropylene-Clay Nanocomposites with Coupling Agents', Ph.D., Michigan State University, 44 (2010).

100. R. Rezanavaz, M. K. R. Aghjeh and A. A. Babaluo, *Polymer Comp.* **31**(6), 1028-1036 (2010).

101. J. Meissner, T. Raible and S.E. Stephenson, *Journal of Rheology*, **25**(1), 1 (1981).

102. D. Godshall, G. Wilkes, R. K. Krishnaswamy and A.M.Sukhadia, Polymer **44**, 5397 (2003).